Doctoral Dissertation

Chaminda Pradeep

Tomographic Approach to Automatic and Non-Invasive Flow Regime Identification

Telemark University College
Faculty of Technology

Chaminda Pradeep

Tomographic Approach to Automatic and Non-Invasive Flow Regime Identification

Thesis for the degree Philosophiae Doctor (PhD)
Telemark University College - Faculty of Technology

PhD Thesis 4:2015

ISBN 978-82-7206-400-5
ISSN 1893-3068

Telemark University College
P.O. Box 203
NO-3901 Porsgrunn
Norway

Phone: +47 35 57 50 00
Fax: +47 35 57 50 01
http://www.hit.no/

© 2015 Galahitiya Vidana Arachchige Chaminda Pradeep

Dedicated to all who wish to do a PhD

Preface

The experiments, data analysis and other related works performed during the degree of philosophiae doctor (PhD) studentship are the main inclusions of the thesis you are holding in your hand. But the path to this achievement was a hard one. Without the supports and inputs from different people this would not be here.

Among those who supported, one who comes first to my mind in is my supervisor Professor Saba Mylvaganam. First of all I would thank him for offering me the opportunity to follow this PhD course, and secondly for his guidance through the whole research work. I was very lucky to have such a supportive supervisor, especially with the preparation of publications and thesis writing.

His strong in depth knowledge on process tomography and instrumentation were also very helpful in my research.

I would like to thank my co-supervisors, Professor Bernt Lie for valuable discussions and conducting a PhD course for students and Professor Wuqiyang Yang from University of Manchester, for arranging visits to his research facilities and giving us a better introduction to the tomographic researches and for advising me in the capacity of co-supervisor.

My thanks are due to Professor Mi Wang of school of chemical and process engineering, faculty of engineering, University of Leeds and Ms. Changhua Qiu of Industrial Tomography Systems, UK for the advice in the beginning phases of my research in process tomography. Mr. Bill Randall of the University of Cape Town, South Africa, gave me good insight and practical help in using the ERT system developed by his group both in his department and our department during his visit to a seminar on ERT systems held in TUC.

My great appreciation goes to Professor Morten C. Melaaen for letting and helping me to work with multiphase flow rig at Telemark University College (TUC). Even though he was not involved with my work directly, his guidance to get technical supports from his former students was very helpful.

My sincere appreciation is extended to Dr. W. A. S. Kumara, for his help on running the Multiphase flow rig, gamma densitometry and high-speed image capturing. His knowledge and experience in multiphase flow experiments were very helpful, especially in the first year of my research work. I would like to thank Dr. Sondre Vestøl for giving me his measurement data to compare with tomographic data. I appreciate the opportunity given by Dr. Lene Amundsen of STATOIL for running some calibration tests with low and high pressure multimodal tomographic systems in the research center of STATOIL in Porsgrunn.

Special thanks to Mr. Øivind Urkedal, Mr. Per Morten Hansen, Mr. Talleiv Skredtvedt, Mr.

Eivind Fjelldalen and Mr. Thorstein Fåne, for their technical assistances.

I appreciate very much the advise given by Mr. Malcolm Byars of Process Tomography Ltd and Support of Mr. Ken Primrose of Industrial Tomography Systems.

I also like to thank IEEE for giving me a student scholarship for participation in the IEEE SAS 2012 Symposium held in Brescia, Italy.

I would like to extend my gratitude to my colleague Yan Ru, who was one of the co-authors of my publications, for her support throughout the research. I am pleased to thank professor Britt Halvorsen and Dr. Christo Rautenbach for sharing their experience with the ECT with fluidised bed applications.

When my inspiration and motivation were totally gone at the end, where I was writing the thesis, Associate Professor and the Head of the Department Randi Toreskås Holta and Associate Professor and PhD coordinator Lars Andre Tokheim always guided me towards the completion of the thesis in the absence of Professor Saba Mylvaganam. So, my special thanks goes to them for their support.

Special thanks to Professor David Di Ruscio for meeting me to discuss model identification and further more giving valuable comments on my thesis.

Sincere gratitude to my friends and fellow PhD students, Chameera, Sanoja, Sampath, Anushka and Roshan for their inspiration, support and company.

Chaminda Pradeep G. V. A.
July 2015

Summary

This thesis mainly presents the use of process tomography to study and measure flow parameters in two phase horizontal and near horizontal flows. All static measurements were made using a horizontal separator section while dynamic flow measurements were performed using the flow facility at Telemark University College. Most of the study was based on Electrical Capacitance Tomography (ECT) and Electrical Resistance Tomography (ERT) measurements. Unlike typical tomographic applications, here, the focus was on extracting information from measurements and not constructed tomograms.

Artificial Neural Network (ANN) algorithms based inferential models were first developed for interface level estimation of layered flows. The results were tested and validated with both static and dynamic measurements. Separate models for oil-air, water-air and oil-water two phase combinations were developed to compare with the measurements. After having very satisfactory estimations with 12 electrode sensor data, the study was extended with the possible reduced number of electrode sensors. Here the selections were 6, 5 and 4 selected electrode combinations. Corresponding measurements of the selected electrodes were employed in the estimations. The speed of the estimation with the reduction of electrode of the sensor was also studied separately. The experimental analysis demonstrates that interface estimates of the layered flows are possible with ANN based algorithms. It is further evident that even with the reduced 6, 5 and 4 electrode sensor arrangements, acceptable results can be observed quickly but with some increased uncertainty. The possibility of using as a redundant system is also an added advantage of having this type of estimators separately.

Some Gamma measurement results presented by (Vestøl 2013) were tested with the ECT tomographic technique. Here, tomograms were used in this study. For oil-air two phase flows the comparisons were acceptable despite the low resolution with ECT. But, ECT does not produce acceptable tomograms when water was the dominant medium.

Slug flow parameters, such as slug translational velocity, slug front and tail velocities, liquid film thickness, slug frequency and slug length, were estimated using ECT and ERT measurements. The cross-correlation technique was used in the slug translational velocity calculation. This calculated slug translational velocity, then used in the other parameter estimations. High-speed camera images captured provided that the estimations are acceptable, though the capturing frequency (100Hz) is not high enough. Time series of differential pressure measurements were also captured along with the tomographic measurements for the verification purpose. They were separately studied with different techniques for the slug flow parameter estimations. Power Spectral Density (PSD) was applied in the calculation of slug frequency. Results show a good

agreement between ECT and ERT based estimations and differential pressure based calculations.

Possible use of capacitance measurement data matrix properties for the flow regime detection was tested with experimental data. Here independent capacitance measurements of each frame are arranged in a symmetric matrix and the eigenvalues of them are calculated. How the eigenvalues are related to the flow parameters such as liquid fractions are studied here. A good agreement with both measurement data and mathematical model based results are given by (Fang & Cumberbatch 2005). A solid relationship between leading eigenvalue and the volume fractions could be observed. Possible identifications of flow regimes with the second and third dominant eigenvalues were also discussed with the experimental results.

Dynamic time warping technique which is commonly applied to align two time series signals are used in the liquid slug length estimations. The fusion of both tomometric and differential pressure measurements is done with this approach. Then, the relationship between liquid slug length and warped pressure peak was also investigated. The relationship between differential pressure and liquid slug length could be identified as linear. The results are proven with different experimental data.

PART I

Introduction

Contents

List of Figures

List of Tables

Nomenclature

Symbol	Unit	Explanation
A	m^2	Cross-sectional area
C	F	Capacitance
$\mathbf{c}$	F	Capacitance vector
$C_{i,j}$	F	capacitance between i^{th} and j^{th} electrodes
$\mathbf{C_m}$		Capacitance measurement Data matrix
$\mathbf{C_{\bar{m}}}$		Constructed capacitance measurement Data matrix
$\mathbf{c_{max}}$	F	Capacitance at upper reference point
$\mathbf{c_{min}}$	F	Capacitance vector at lower reference point
C_n		Normalised capacitance measurement
$\mathbf{c_n}$		Normalised capacitance vector
Co_δ		Cost function of a warping path w.r.t. δ
Dp	mbar	Differential pressure
$DTW(x,y)$		Dynamic time warping distance between signals x and y
D	mm	Flow pipe diameter
d_i		i^{th} element of the target ANN output vector
e		Error of ANN estimation
Ei_d		Magnitude of leading eigenvalue
$E_{i,i+1} - E_{j,j+1}$	V	Voltage measurement between j^{th} and $j+1^{\text{th}}$ electrodes when current is applied to i^{th} and $i+1^{\text{th}}$ electrodes
F		power spectrum of the signal z
f_{cap}	Hz	Data capturing frequency/rate
f_{sam}	Hz	Sampling frequency
f_s	Hz	Slug frequency
g		Error gradient
$\mathbf{H}$		Hessian matrix of ζ
h_{Dp}		Pressure peak
$\bar{h}_{Dp}$		Mean of the pressure peak
h_l	mm	Interface height/level (film thickness)
$\mathbf{h_{ln}}$		Normalised interface height
h_w	mm	Water interface level
I	A	Electrical current

Symbol	Unit	Explanation
$\mathbf{I_{Cn}}$		Normalised conductivity vector
$\mathbf{I_{ei}}$		Identity matrix with the size of $\mathbf{C_{\bar{m}}}$
$\mathbf{J}$		Jacobian matrix of ζ
$\mathbf{J_C}$		Jacobian of ξ
$\mathbf{J_R}$		Jacobian matrix which relates voltage and conductivity
K	F/m	Permittivity of the pixel area
$\mathbf{K_{max}}$	F/m	Permittivity vector at higher reference point
$\mathbf{K_{min}}$	F/m	Permittivity vector at lower reference point
$\mathbf{K_n}$		Normalised permittivity vector
L_f	m	Liquid film length
L_s	m	Liquid slug length
L_{pla}	m	Distance between two ECT/ERT sensor planes
M		Number of measurement per frame
N_C		Number of electrodes in ECT sensor
N_R		Number of electrodes in ERT sensor
$\hat{\mathbf{n}}$		Unit vector normal to the electrode surface
n_{con}		Number of connections in the ANN
n_{ct}		Length of the capacitance data matrix $\mathbf{c_t}$ used in training
n_{cv}		Length of the capacitance data matrix $\mathbf{c_v}$ used in validation
n_{lay}		Number of layers in an ANN
$n_{nu,l}$		Number of neurons in l^{th} layer of the ANN
n_p		Length of the warping path signal P_w
n_{pix}		Number of pixels in a tomogram
n_s		Number of slugs
n_x		Length of the time series x
n_y		Length of the time series y
n_z		Length of the time series z
O_k^l		Output of the k^{th} neuron in layer l of ANN
$\mathbf{O^o}$		Output vector of ANN
P_w		Warping path
Q	C	Electric charge
$\mathbf{S}$		Sensitivity matrix of ξ
s		Sensitivity of the capacitance measurement
S_{pl_i}		Measurement signal from sensor plane i
$STD_{h_{Dp}}$		STD of the pressure peak
$STD_{T_{ANN}}$	μs	Standard deviation of ANN execution time
T_{add}	μs	Time consumed for addition
T_{ANN}	μs	Execution time of ANN
T_{fun}	μs	Time taken by activation function of ANN
T_{mul}	μs	Time taken for multiplication
T_{ob}	s	Observation time period
t_s	s	Time window of the slug

Symbol	Unit	Explanation
U_f	m/s	Slug tail velocity
U_{GS}	m/s	Superficial gas velocity
U_{LS}	m/s	Superficial liquid velocity
U_{mix}	m/s	Mixture velocity
U_s	m/s	Liquid slug velocity
U_t	m/s	Slug translational velocity
u		Electrical potential distribution
V	V	Electrical voltage
V_{mean}	V	Mean voltage
V_s	V	Supply voltage
$\mathbf{v_n}$		Normalised voltage vector
$\mathbf{W^l}$		Weight matrix which relates l^{th} layer and $(l+1)^{th}$ layer of ANN
$\mathbf{w}$		Weight vector of ANN
w_{ij}^{l}		Synaptic weight between i^{th} neuron in layer l and j^{th} neuron in layer $l-1$
x, y, z		General symbols for input variables
x_i, y_i, z_i		Context dependent input variables
$\mathbf{x}$		Input vector
α		volume fraction
α_o		Oil volume fraction
α_w		Water volume fraction
$\alpha_{w/o}$		Water volume fraction when two phases are water and oil
β	$^\circ$	Angle of inclination
Γ_j		Surface area of the j^{th} electrode
δ		Squared distance between two time series elements
ε	F/m	Electrical permittivity
ε_r		Relative permittivity
ζ		Squared error of ANN estimation
η		Learning parameter
$\mu_{T_{ANN}}$	μs	Mean of ANN execution time
ν		Electrical potential distribution u of the electrode surface
σ	S/m	Electrical conductivity
τ	s	Time delay/lag
τ_{max}	s	Time delay at correlation peak
ϕ		Activation function of ANN

Abbreviation	Explanation
ANN	Artificial neural network
DP	Differential pressure
DTW	Dynamic time warping
ECT	Electrical capacitance tomography

Abbreviation	**Explanation**
ECTm	Electrical capacitance tomometry
ECVT	Electrical capacitance volume tomography
ERT	Electrical resistance tomography
FEM	Finite element method
FFT	Fast Fourier transform
FPS, fps	Frames per second
LBP	Linear back projection
NNT	Neural network toolbox (MATLAB)
PCA	Principle component analysis
PDT	Differential pressure transducer
PID	Proportional integral derivative
PIV	Particle image velocimetry
PSD	Power spectral density
PTL	Process tomography limited
RMS, RMSE	Root mean square error
SVM	Support vector machine
TB	Taylor bubble
2D	Two dimensional

Special mathematical operators

Notation	**Explanation**
$./$	Element by element division

Chapter 1

Introduction

An introduction to the main research works and an overview on each research activity are given briefly in this chapter. Background research works are also addressed with a short review on relevant current literature. The thesis structure and main contributions are also presented in this chapter.

1.1 Background

In industrial applications, multiphase flows are typically constrained to pipes or vessels. Powder or particulate material transportation using pneumatic conveying, fluidization and liquid and gas transportation are some examples of multiphase flows.

When it comes to the oil and gas industry, most commonly considered phases are natural gas, oil and water, since the sand is separated in preliminary stages. This three phase flow mixture is complex to measure/observe and control. One of the challenges in the industry is to understand this complex flow behavior. Different kinds of technologies are currently being used in observations and identifications of the flow behaviors and patterns (regimes). Simulations of flow phenomena are also performed using some complex simulation tools like FLUENT for different conditions.

Obviously, first study should be on identification of different flow patterns. Then the flow parameters and their relationships with those patterns and their transitions can be investigated. Those relationships can be useful in flow control applications.

Most of these complex flow pattern/regime observations are still made visually by using high-speed cameras, but there are some issues regarding the speed of the data acquisition and processing to produce the data of interest. When it comes to the non transparent vessel or pipe/tube or sometimes with formation of emulsions, such visual methods are not suitable. Some analytical techniques with available process tomographic measurement information can be used to find the flow regimes. The non-invasive nature of the process tomography technology is one of the reasons for its latest popularity. Here, the sensors used are of either electrical impedance or radiation based techniques. Different mathematical techniques may be used to analyse the signal fluctuation characteristics and thus to determine the flow patterns.

Analyses presented in this thesis are based on the electrical capacitance and resistance tomographic measurements. In the context of process tomography, the main focus is on the construction of better tomograms (images) based on the inter-electrode measurements. Instead of dealing with complex image constructions and image processing, possibility of using raw measurements in the estimations of flow parameters are studied in this thesis.

When performing online measurement of multiphase flow parameters, it may not be possible to use images (tomograms). This is mainly due to the time taken by the image reconstruction algorithms. Such delays involved may not be accepted by the control programs. Since numbers of capacitance measurements are less than number of pixels in the tomograms, the construction is under determined and with all other processing techniques it is not possible to get very accurate images. But, higher accuracy is not so important compared with the response time in the control process. Hence with simple inferential models, it may be possible to estimate the parameter of interest. Here, prior data is needed in the model development. Estimations using such models will be fast but the accuracy may not be high.

Artificial Neural Networks (ANN) is mainly used in the estimate of interface levels. Property of the measurement matrix are also studied and analysed in the identification of flow regimes and slug flow parameter estimations.

Differential pressure measurements and high-speed camera images are also used to verify some analysis and relationships. Specially with slug flow studies, high-speed camera images are important to identify slug boundaries. Effects on measurements with emulsion in the system have not been a part of this study.

1.2 Objectives

Objectives of the research are mainly to study what briefly is given in the above section. They can be explained as:

1 Tomometric approach on estimation of stratified interfaces:

  Interface level of stratified flows can be estimated using different techniques. Possibility of calculating with the tomometric measurements would be more convenient. Apart from the estimation of the interface level, estimation time is also important and needs to be studied.

2 Multimodal process tomometry, Electrical Capacitance Tomography (ECT) and Electrical Resistance Tomography (ERT) for the estimation of slug flow parameters in horizontal/near horizontal flows.

  The main objective of the research was on flow regime observations with much focus on slug flow study. Main focus was on identification without going into image observations of the flow and possible component velocity and parameter estimations especially with slug flows.

3 Study of measurement data matrix properties to identify flow regimes.

4 Studying the detection of flow reversal involved with some slug phenomena with twin plane tomometric data.

5 Studying the fusion of tomometric signals and pressure signals using Dynamic Time Warping (DTW) technique to estimation improved parameters.

1.3 Contributions

1 Interface level estimations with tomometric measurements have been investigated before by (Alme 2007) and here possibility of fast estimations is further studied. Interfaces correspond to ECT measurements used in this work are measured separately for the model training and verification. Possibility of gaining fast estimations by reducing number of capacitance measurement electrodes was further studied. Interface estimations were performed based on the developed Feed-forward ANN model. Then, the study was extended to see how the number of hidden neurons affects the estimation time and uncertainty. Study was limited to horizontal pipe flows. Chapter 4 and Paper 1 in the attached collection of articles, describe the work done on interface detection.

   Some of the results were tested and compared with the Gamma measurement performed separately under the same flow conditions. ECT images were used along with corresponding camera images in the comparison. Results can be found in Paper 3.

2 Sensor information captured from flows is fused using the mathematical tools and techniques in the estimations. Identification of Interface boundaries, flow patterns and parameterization of each flow conditions are interested in investigation. Both ECT and ERT measurements were successfully used in the estimation of slug parameters such as slug frequency, translation velocity and slug length. Differential pressure measurements and high-speed camera images were also useful in the verification of estimations. The importance of data capturing rate on velocity estimations are also discussed under this. Detailed information is given in Chapter 5 and Paper 4.

3 How to use the measurement data matrix properties to identify flow regimes was studied. The non-intrusive nature in the identifications and timely recognition of the flow regimes were the main reasons for testing this approach. Mathematical simulations on this approach have been presented in (Fang & Cumberbatch 2005). How the eigenvalues of the measurement matrices vary with the flow regime variations and their regions are studied. Results were compared with the simulations given in (Fang & Cumberbatch 2005).

4 Detection of flow reversing with the twin plane ECT measurement systems was also a part of this study. The results are verified using high-speed camera images. Cross-correlation of time series of raw capacitance values captured from twin plane ECT systems was used in detection of the flow direction.

5 Possible estimation of slug parameters by fusing pressure signals and Electrical Capacitance Tomometry (ECTm) using Dynamic Time Warping (DTW) technique was studied.

Aligning pressure signals and ECTm signals which were not captured simultaneously was done with DTW. Relationship between warped pressure peak and liquid slug length was tested with high-speed camera image. Camera images are processed to get time series signals which are compared with ECT signal and warped Differential Pressure (DP) signal for validation. Chapter 7 and attached Paper 5 give more details on the DTW techniques used and the combined study of high speed camera images and DP based results.

1.3.1 Dissemination of results

Some important parts of the work were presented in conferences and published in journals. The following gives a list of publications in journals and conferences:

1 Ru, Y., Pradeep, C., Mylvaganam, S. (2010) Artificial neural networks for ECT based interface detection in separators, in 'at 6thWorld Congress on Industrial Process Tomography', Beijing, China.

2 Pradeep, C., Ru. Y., Mylvaganam, S., (2011). Interface detection in pipe separators using ECT: Performances with reduced number of sensing electrodes'. IEEE Sensors Application Symposium in San Antonio, Texas, February 2011.

3 Ru, Y., Pradeep, C., Mylvaganam, S. (2011), 'Neural networks in electrical capacitance tomography (ect)-based interface detection', Measurement Science and Technology 22(10), 104006.

4 Pradeep, C., Ru. Y., Mylvaganam, S., (2012). Neural Network-Based Interface Level Measurement in Pipes Using Peripherally Distributed Set of Electrodes Sensed Symmetrically and Asymmetrically, IEEE Transactions on Instrumentation and Measurement, Vol:61 , Issue: 9, September 2012, pp: 2362-2373

5 Pradeep, C., Ru. Y., Mylvaganam, S., (2012). Reverse Flow Alarm Activation using Electrical Capacitance Tomometric (ECTm) Correlation. Proceedings of IEEE Sensors Application Symposium in University of Brescia, Brescia, Italy, February 2012, pp: 1-5

6 Pradeep, C., Ru. Y., Vestøl, S., Melaaen, M. C., Mylvaganam, S., (2012). Electrical capacitance tomography (ECT) and Gamma radiation meter for comparison with and validation and tuning of (CFD) modeling of multiphase flow. Proceedings of IEEE International conference on Imaging Systems and Techniques, Manchester, UK in July 2012.

7 Pradeep, C., Ru. Y., Vestøl, S., Melaaen, M. C., Mylvaganam, S., (2014). Electrical capacitance tomography (ECT) and Gamma radiation meter for comparison with and validation and tuning of computational fluid dynamics (CFD) modeling of multiphase flow. Transactions of IOP journal of Measurement science and technology, Vol:25, Issue: 7, March 2014, pp: 075404-075411.

8 Pradeep, C., Ru. Y., Mylvaganam, S., (2012). Multimodal Tomometry for Slug Detection in two Phase Flow. Proceedings of 6th International Symposium on Process Tomography (ISPT) in Cape Town, South Africa, March 2012, pp:OR11

9 Pradeep, C., Ru. Y., Mylvaganam, S., (2012). Co-operative sensor fusion using time warping in multimodal tomometry for process control. IEEE conference on Systems and Industrial Informatics (ICCSII), Bandung, Indonesia, September 2012, pp: 219-224.

1.4 Previous work

Though tomographic imaging was developed for medical applications in the middle of 20th century, it was not introduced to the industrial applications till 1980s. Due to increasing demand in non-invasive process studies, by 1990s industries were gaining confidence that tomography would have the potential in industrial process studies (Beck & Williams 1996). Use of capacitance measurement for imaging industrial processes was first introduced in University of Manchester (UMIST), UK (Huang et al 1980). Due to long exposure time involved with the radiation based tomographic methods; they were not feasible to be used in real-time measurements in industrial applications (Beck & Williams 1996).

There are many different types of measurement techniques used in tomographic measurements. Electrical capacitance, electrical resistance, ultrasonic and gamma ray are more common among many. But tomographic construction is more similar despite the modality. There are different types of reconstruction algorithms to have improved tomograms, but it involves high construction time. So, in practice, most of the dynamic flow visualizations, simple linear back projection technique is used to construct the tomograms (Niedostatkiewicz et al. 2009). Some algorithms have been developed to have calibrations while in operation to have improved measurements (Yang et al. 2004). Possible image fusions algorithms for dual plane tomography systems can be found in (Sankowski et al. 2006). Current developments on tomography are largely on 3D image constructions called Electrical Capacitance Volume Tomography (ECVT) and improved image resolutions. But in practice it is still difficult due to computational difficulties (Yang 2010).

Primary objective of process tomography is process visualization, but analysis of raw measurements to extract the parameter, instead of image constructions, can also be more convenient and useful (Niedostatkiewicz et al. 2009). Such approaches are also called as tomometric approach. These approaches create opportunities for the tomographic techniques in the process control applications due to fast responses. Variations in calculated parameters can also be monitored easily in real-time. This approach has been used by (Bennett et al. 1999) in analysis of bubble columns dynamics. Principle Component Analysis (PCA) and Support Vector Machines (SVM) techniques are some of the techniques used in analyzing the raw measurements in the flow regime identification by (Zou et al 2001) and (Wang & Zhang 2009) respectively.

When gas liquid mixture is flowing in vertical pipes, gas component will not get a chance to have a physical contact with the pipe wall. But in horizontal flows, due to gravitational forces, this will not happen. This reason has restricted the use of ERT for vertical flows and hence ERT with horizontal flow measurements can hardly be seen in most of the literature (Ma et al. 2001). Novel approach on level measurements in horizontal flows without going into tomograms have been tested and discussed by (Ma et al. 2001). Horizontal flows and slug parameter estimations presented in attached Paper 4 and this thesis also discuss the possibilities of using ERT.

Different flow regimes generated due to flow rates of gas and solid particles in fluidised beds

has been investigated using ECT as explained by (Dyakowski & Jaworski 2003). Since fluid component involved with most of the fluidised bed applications are non conductive, ECT is more suitable for measurements and flow visualizations. (Rautenbach et al. 2011) and (Rautenbach et al. 2012) explain experimental studies on fluid particles and their influences in parameters using ECT and x-ray tomographic techniques. Investigations of pneumatic conveying of solid particles has also been done by (Dyakowski & Jaworski 2003) and (Datta 2007).

Multiphase flow measurements in petroleum industry are very complex and most of the flow metering are flow regime dependent (Ismail et al. 2005). Process tomographies for possible multiphase flow metering systems are explained in (Primrose et al. 2010). Level measurements in subsea separators can be found in (Hjertaker et al 2001a).

Development of a microwave tomographic system for the oil and gas flow measurements has been studied by (Wu et al. 2009). Studies on process flow measurements with Gamma ray tomography has been done by (Johansen et al. 2014) dealing with two and three phase flows related to the oil and gas industries.

Chapter 2

Measurement and analysing techniques

Since a major part of this thesis work is based on measurements from ECT and ERT techniques, giving an overview of those methods is a part of the content of this chapter. Brief explanations of data analyzing techniques used in different chapters of this thesis are also given here. Processing of a sequence of images captured by high-speed camera to be compared with other time series signals is explained separately in Chapter 7.

2.1 Electrical tomography

A brief mathematical formulation on electrical capacitance and resistance tomographic systems are first discussed in this section. Tomographic systems and sensors used in the measurements are described in the Chapter 3

2.1.1 Electrical capacitance tomographic systems

Calculation of the permittivity distribution of material covered by the sensor plane based on the inter-electrode capacitance measurements is the main functionality of the ECT system. Most of the ECT sensors are non-invasive, lying outside the wall and non-intrusive, touching but not penetrating the wall of the vessel as shown in the Figure 2.1. Construction of the capacitance sensors depends on the physical shape of the object or vessel to be observed, but most of the standard industrial sensors are designed to be mounted on the cylindrical shaped vessel or pipe. A cross-sectional view of a pipe with mounted ECT sensor is shown in Figure 2.1. The sensor shown has 12 electrodes. All sensor electrodes have to be covered by a grounded screen to shield the system from external disturbances. Resistors with larger resistance (around 1MΩ) are connected between the shield and the electrodes to avoid electrostatic build up (Alme 2007). Co-axial cables which reduce the environmental noise and interference connect each electrode of the sensor to the data acquisition system.

There are different measurement strategies available in the data acquisition; the most common one is adjacent measurement strategy which is named as protocol 1 in (Byars 2001). As illustrated in Figure 2.1, an alternative voltage V_s is supplied to one of the electrodes (source

electrode) and the currents flow between source electrode and the remaining electrodes (detecting) are measured separately. These currents are proportional to the capacitances between the source and detector electrodes. The set of capacitances measured by exciting one electrode (as the source) is called a *projection*. Then, the voltage, V_s is applied to the neighboring electrode and current measurements are repeated. Sequentially, all electrodes of the sensor are excited and the current flow to the remaining electrodes are measured . For a sensor with N_c electrodes, there will be a total $N_c(N_c-1)$ possible capacitance measurements. However, as half of these are reciprocal measurements, there are only $N_c(N_c-1)/2$ independent capacitance measurements. One set of these independent measurements which is needed in the construction of a single image is called a *frame*.

V_s (the alternative source voltage) used in the PTL M300 system is $15V$ peak to peak square wave. The excitation frequency is in the range 1 to 2 MHz. However, some latest capacitance tomographic systems have increased the excitation frequency up to 10 MHz.

The capacitance measurements are related to the permittivity of the materials present in the sensor between electrode pairs. The relationship between the electric potential and the permittivity distribution can be given in the Poisson Equation (2.1) as explained by (Wang et al. 2009).

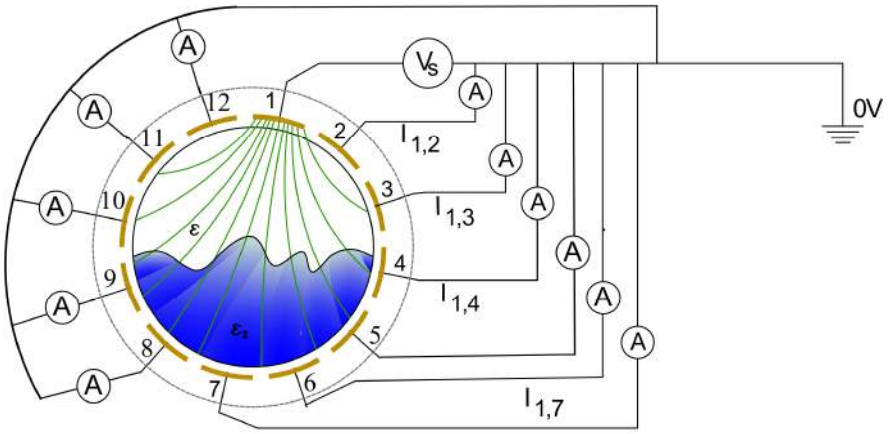

Figure 2.1: Measurement principle of ECT when electrode 1 is excited with V_s and the other electrodes earthed

$$\varepsilon(x,y)\bigtriangledown^2 u(x,y)+\bigtriangledown\varepsilon(x,y)\bigtriangledown u(x,y)=0 \tag{2.1}$$

where $\varepsilon(x,y)$ is the permittivity distribution and $u(x,y)$ is potential distribution for M inter-electrode combinations ($M=N_c(N_c-1)/2$).

Then, the measured capacitance between i^{th} and j^{th} electrodes, $C_{i,j}$, can be calculated by the ratio between stored charge, Q_j, on the j^{th} electrode and the potential difference, $\Delta V_{i,j}$, between i^{th} and j^{th} electrodes as in Equation (2.2). Stored charge on the j^{th} electrode can be further explained as a function of the permittivity distribution of the content in the sensor.

$$C_{i,j} = \frac{Q_j}{\Delta V_{i,j}} = \frac{1}{\Delta V_{i,j}} \oint_{\Gamma_j} \varepsilon(x,y) \bigtriangledown u(x,y) \hat{\boldsymbol{n}} dl \tag{2.2}$$

where Γ is the surface area of the j^{th} electrode and $\hat{\boldsymbol{n}}$ is a unit vector normal to Γ_j. To solve the Equation (2.2), for a known permittivity distribution, $\varepsilon(x,y)$, Finite Element Methods (FEM) or a similar numerical method is to be used. The potential distribution can also be given as a function of permittivity distribution. Then, the above equation can be rewritten for any pair of electrodes as,

$$C = \xi(\varepsilon) \tag{2.3}$$

where C is the capacitance between a pair of electrodes. ξ is the function defining the capacitance C as a function of permittivity ε.

The change in capacitance when a slight change in permittivity distribution gives,

$$\Delta C = \frac{d\xi}{d\varepsilon}(\Delta\varepsilon) + O\left((\Delta\varepsilon)^2\right) \tag{2.4}$$

where, ΔC is the change in capacitance, $\frac{d\xi}{d\varepsilon}$ is called the sensitivity of the capacitance against permittivity distribution, $\Delta\varepsilon$ is the change in permittivity distribution, Since, $\Delta\varepsilon$ is very small, the higher order terms of the equation, $O((\Delta\varepsilon)^2)$ can be neglected (Yang & Peng 2003).

$$\Delta C \approx s\Delta\varepsilon \tag{2.5}$$

where $s = \frac{d\xi}{d\varepsilon}$ is the sensitivity of the capacitance measurements.

To visualise the permittivity distribution across the sensor cross-section, cross-sectional areas of the sensor plane is discretised in to number of pixels, n_{pix}. Permittivity inside each pixel area is considered constant. This cross-sectional area is typically divided into 32×32 pixel grid and then total number of pixels, n_{pix}, will be 1024. Circular image constructed contains only 812 pixels since others lie outside the circular sensor cross-section. Figure 2.2 illustrates a typical pixel grid. Since change in permittivity distribution causes changes in capacitance measurements, change of capacitance measurement is a function of all n_{pix} pixel values. So, $\Delta\varepsilon$ in the Equation (2.5) can be written as an $n_{pix} \times 1$ column vector and s has to be presented as a $1 \times n_{pix}$ raw vector.

Similarly, for all inter-electrode measurements in one frame, M number of equations exists (for a 12 electrode sensor M is 66). Hence all M number of equations can be arranged to be expressed in a matrix form as,

$$\boldsymbol{\Delta C} = \mathbf{J_c} \boldsymbol{\Delta\varepsilon} \tag{2.6}$$

where $\boldsymbol{\Delta C} \in \mathbb{R}^{M \times 1}$. $\mathbf{J_c}$ is the Jacobean of ξ.

This process of calculating the inter-electrode capacitances from a known permittivity distribution is called as the *forward problem*. This is the linear approximation to the non linear *forward problem* (Yang & Peng 2003). Since the range of permittivity and capacitance values are very small, normalised form is used.

$$\mathbf{c_n} = \mathbf{S}\mathbf{K_n} \tag{2.7}$$

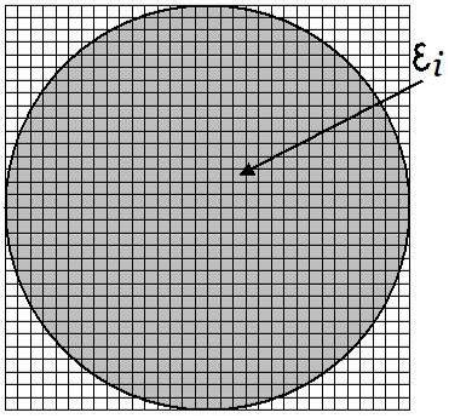

Figure 2.2: A typical 32×32 pixel grid. Pixel grid is square and tomogram is cylindrical. Hence, only 812 (marked in grey) out of the 1024 pixels are sufficient for the construction of a tomogram

where $\mathbf{c_n}$ is the normalised capacitance vector, $\mathbf{K_n}$ is the normalised permittivity vector and $\mathbf{S}$ is the Jacobian matrix which relate normalised capacitance vector and normalised permittivity vector.

Before going for the measurement in a process application, calibration of the sensor has to be performed by filling the sensor vessel with high and low permittivity components of the mixture separately. All capacitance values in $\mathbf{c}$ ($\mathbf{c}$ is the capacitance measurement vector) are then normalised to have values between zero (sensor is filled with low permittivity material) and 1 (sensor is filled with high permittivity material) (PTL 2009). Equation (2.8) shows the normalisation of the capacitance measurements $\mathbf{c}$. The relationship between a normalised capacitance measurement and an absolute capacitance measurement can also be illustrated as shown in the Figure 2.3.

$$\mathbf{c_n} = (\mathbf{c} - \mathbf{c_{min}}) ./ (\mathbf{c_{max}} - \mathbf{c_{min}}) \tag{2.8}$$

where $\mathbf{c}$ is the absolute capacitance measurement vector, $\mathbf{c_{max}}$ is the capacitance vector measured at higher permittivity calibration point and $\mathbf{c_{min}}$ is the capacitance vector measured at lower permittivity calibration point. Here $./$ denote dividing each element in the vector $\mathbf{c} - \mathbf{c_{min}}$ by the corresponding element in vector $\mathbf{c_{max}} - \mathbf{c_{min}}$.

Similarly, pixel values of permittivity distribution image are also normalised.

$$\mathbf{K_n} = (\mathbf{K} - \mathbf{K_{min}}) ./ (\mathbf{K_{max}} - \mathbf{K_{min}}) \tag{2.9}$$

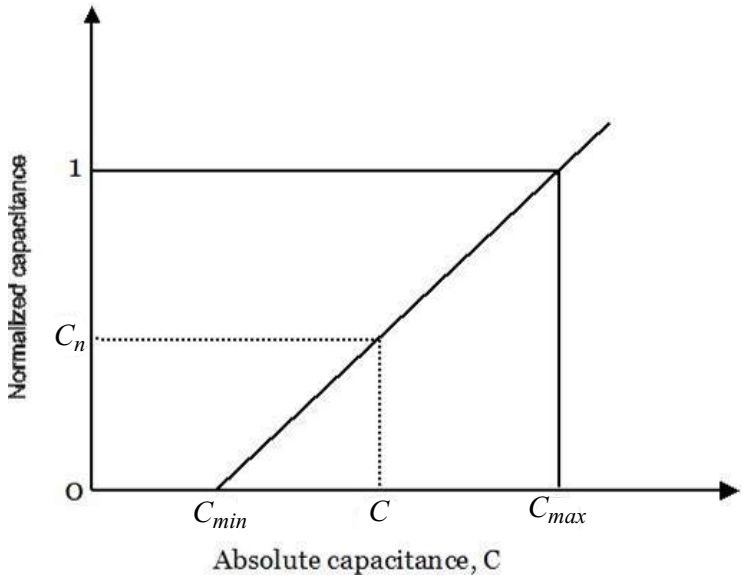

Figure 2.3: Normalisation of an inter-electrode capacitance measurement (C). The inter-electrode capacitance measured at the lower permittivity calibration point (C_{min}) is assigned to 0 while the measurements at the higher calibration point (C_{max}) is assigned value 1.

where $\mathbf{K_n}$ is the normalised permittivity vector. $\mathbf{K}$ is the permittivity vector. $\mathbf{K_{max}}$ is the permittivity vector at higher calibration point and $\mathbf{K_{min}}$ is the permittivity vector at lower calibration point.

In process of the tomography image construction, permittivity distribution map has to be generated based on the capacitance measurements. This is termed as *inverse problem*. Simply, it can be explained as finding unknown $\mathbf{K_n}$ from known $\mathbf{c_n}$ in the Equation (2.7). But there are two main problems as explained in (Yang & Peng 2003). First one is, the number of unknowns are larger than the number of equations. The second one is, the sensitivity matrix is not constant and varies with the change in permittivity distribution. When materials with permittivities within a close range are present in the process, the tomograms will not have clearly defined boundaries, leading to distortion and fuzziness of the images at interfaces of different materials.

Different kinds of algorithms are used in the image construction (calculation of $\mathbf{K_n}$). The simplest one among them is Linear Back Projection (LBP).

Equation (2.7) can be rearranged to isolate $\mathbf{K_n}$ as,

$$\mathbf{K_n} = \mathbf{S^{-1}c_n} \tag{2.10}$$

In practice, $\mathbf{c_n}$ is taken from inter electrode measurements. $\mathbf{K_n}$ is calculated using $\mathbf{S^{-1}}$ and $\mathbf{c_n}$. But, $\mathbf{S}$ is not a square matrix and inverse does not exist. However, LBP algorithm uses

the transpose of **S** as its inverse. Though this is not correct according to the mathematical point of view, it is widely used in many online image construction applications. This is mainly due to its simplicity and hence lower time taken by the algorithm. Even though this algorithm produces poor-quality images, it is still useful in some online applications, where processing time is important (Yang & Peng 2003).

2.1.2 Electrical Resistance Tomographic systems

Similar to ECT system, ERT system also produces cross-sectional images, but it shows the distribution of electrical conductivity of the contents filled in the process vessel or pipeline. Measurements are taken at the boundary of the vessel or pipe, but unlike in ECT, ERT electrodes should have a physical continuous contact with the conductive components inside. It shows ERT measurements are invasive, even though it is still non intrusive.

Principles behind the construction of tomograms are more similar to ECT. Cross-sectional distribution of the resistivity/conductivity is generated as a tomogram based on the boundary measurements. In the measurement process, a current is injected (eg:- M3000 system of ITS[1] and Current pulse ERT system of UCT[2]), between a pair of electrodes and the resultant voltage differences between remaining electrode pairs are measured according to a pre-defined measurements protocol.

Adjacent protocol is the more common measurement strategy. Here, current is applied through two neighboring electrodes (eg: electrode 1 and 2) and voltages are measured from the remaining pairs of neighboring electrodes (eg: electrodes 3-4, 4-5, ect ...). Then current is applied through the next adjacent pair of electrodes and the voltage measurements are repeated. This is repeated for all adjacent pairs (current injection) by measuring all independent measurements.

Similar to ECT, electrodes are arranged at equal intervals around the boundary of a circular pipe (in multiphase flow applications). Typical number of electrodes in an ERT sensor is 16. Electrode arrangement and adjacent measurement protocol is illustrated in the Figure 2.4. Electrodes of the ERT sensors should be more conductive compared to the continuous flow inside the pipe to avoid contact impedance (ITS 2005). Typically, electrodes are made of stainless steel, brass or silver palladium alloy (ITS 2005). In the designing of the electrodes, diameter of the pipe, flow velocity and the conductivity range of the media being measured should be taken in to consideration.

Since the conductance dominates in ERT, the governing Poisson's equation which relates potential distribution, $u(x,y)$, and conductivity distribution, $\sigma(x,y)$, can be expressed as in (Alme 2007).

$$\nabla.\sigma(x,y)\,\nabla u(x,y) = 0 \tag{2.11}$$

How to derive the Equation (2.11) from Maxwell's equations has been explained well in (Cheney et al. 1999). Since a current is applied to the external electrodes in measurement procedure, the integral of the current density over the electrode will be equal to the current applied,

[1] Dual modality tomography instrument of Industrial Tomography Systems

[2] Product of University of Cape Town

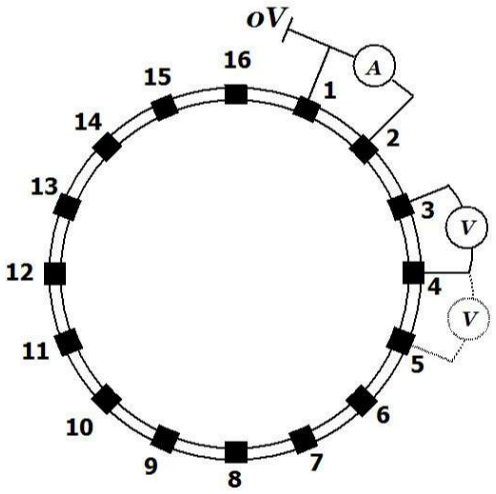

Figure 2.4: Typical adjacent measurement principle of ERT. A current is applied between electrode 1 and 2. Then, voltages between remaining pairs of electrodes are measured. Then current is applied through next adjacent pair (electrode 2 and 3) and voltage measurements are repeated. This current injection method is repeated for all adjacent pairs.

I_j. For the gaps between electrodes this will be zero. To model the very high conductivity of the electrodes, $u(x,y)$ is constrained to a constant. These three boundary conditions can be given as in (Cheney et al. 1999).

$$\begin{array}{rl} \int_{el} \sigma \frac{\partial u}{\partial v} ds = I_j & j = 1,2,...,N_R, \\ \sigma \frac{\partial u}{\partial v} = 0 & \\ u = V_j \ on \ \ electrode_j & j = 1,2,...,N_R, \end{array} \tag{2.12}$$

where N_R is the number of electrode in ERT sensor. V_j is the voltage on j^{th} electrode. Here, $V = u$ on the electrode surface.

Solving Equation (2.11) to find $\sigma(x,y)$ for given V and I, boundary voltages and currents is called as *inverse problem*. In analogy to Equation (2.6) discussed in conjunction with ECT, this can be expressed by

$$\mathbf{v_n} = \mathbf{J_R I_{Cn}} \tag{2.13}$$

where $\mathbf{v_n}$ is the normalised voltage vector, $\mathbf{I_{Cn}}$ is the normalised conductivity vector and $\mathbf{J_R}$ is the Jacobian matrix which relates normalised conductance vector and normalised voltage vector. *Forward problem* has to be solved using numerical methods, such as FEM (similar to ECT). Principles of image construction and *inverse problem* are very much similar to ECT, but the constructed tomograms in ERT show conductivity map instead.

2.2 Signal Processing Techniques

Artificial neural networks were used for the model identification mainly in the interface level estimation. Cross-correlation technique and power spectrum analysis were used for velocity estimations and frequency estimations in slug flow. DTW was important technique in the alignment of two signals Differential pressure, D_p and liquid volume fraction, α. In the palette of techniques used for analysis of raw data, a matrix consisting of raw data from each frame is analysed using eigenvalues and making use of the dominant eigenvalues in finding relationships to some of the characteristic parameters associated with the flow or flow regimes.

2.2.1 Artificial Neural Networks (ANN)

Nervous system of the human body processes information using biological neurons for identification and managing the physical functionality of the body (eg: human vision, odor, etc.). The brain is doing nonlinear highly complex computations to do all functionality. The processing elements called *neurons* are working collectively to fulfill those requirements. ANN is also made to act as same way for the particular application it is used, such as pattern recognition or data classification, through a learning process. Learning in ANN systems is principally same as biological systems, but, ANN involves adjustments of synaptic weights between the *neurons* and *biases*.

There are many different types of neural networks. Three types of them are widely used depending on the application requirements. They are feed-forward, recurrent and self-organizing neural networks. The work presented in the Chapter 4 mainly used feed-forward neural networks for interface estimations.

2.2.2 Feed-forward neural network

A brief overview on a feed-forward neural network is given in this section. Generally these kind of networks are named also as multilayer Perceptron ((Haykin 2008)). As illustrates in Figure 2.5, a neuron which is the building block of the ANN contains inputs $\mathbf{x} = [x_0, x_1, ...x_m]^T$ where $\mathbf{x} \in \mathbb{R}^{(m+1)\times 1}$, synaptic weights w which weight the inputs before further computation and the activation function ϕ which should be differentiable. As explained in (Matlab 2002), there are three common types of transfer functions, ϕ. They are given in Equation (2.14). (Marsshdeh 2006) says that a neural network with continuous transfer functions given in Equation (2.14) in it's output layer is a universal approximator.

$$\begin{aligned} \textit{Linear} \quad & \phi(x) = x \\ \textit{Logsigmoid} \quad & \phi(x) = \frac{1}{1+e^{-x}} \\ \textit{Tansigmoid} \quad & \phi(x) = \frac{1}{1+e^{-2x}} - 1 \end{aligned} \tag{2.14}$$

In each neuron, inputs are weighted and summed before sending through the activation function. Input x_0, which is always 1, is also weighted and added to the summation at each neuron.

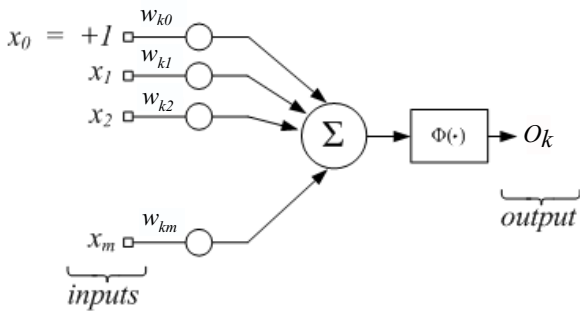

Figure 2.5: Basic components of an artificial neuron with inputs x_1, x_2, ..., x_m and output O_k

This term is called as *bias* input. The output of a given neuron k in a selected layer l can be calculated according to the Equation (2.15) given below.

$$O_k^l = \phi\left(\sum_{i=0}^{n_{nu,(l-1)}} w_{ki}^{l-1} x_i\right) \tag{2.15}$$

where w_{ki} is the weight used to multiply the i^{th} input before sending to k^{th} neuron. O_k^l denotes the output of k^{th} neuron in l^{th} layer. $n_{nu,l}$ is the number of neurons in l^{th} layer.

To handle the more complex mapping, a network consists of these kind of neurons are constructed. The structure is typically organised in layers as given in Figure 2.6. Outputs of a layer are inputs to the next layer, unless it is the output layer. Network shown in the figure has 4 layers. The number of input to ANN considered as the first layer, even though there are no active neurons available there. When the whole network is considered, its outputs are functions of a given set of inputs only. All other parameters involved are fixed after the 'training'. In the process of training, synaptic weights are adjusted to map the ANN outputs with the given outputs. Prior data are necessary in the training of these kind of networks.

Since there are no any active neurons in 1st layer of the 4 layer ANN, outputs of the 1st layer are same as inputs.

$$\mathbf{O^l} = \mathbf{x} \tag{2.16}$$

Output of a middle layer neuron (j^{th} neuron of l^{th} layer) can be given as,

$$O_j^l = \phi\left(\sum_{i=0}^{n_{nu,(l-1)}} w_{ji}^{l-1} O_i^{l-1}\right) \tag{2.17}$$

Then, Output vector of a middle layer l, can be expressed as,

$$\mathbf{O^l} = \phi\left(\mathbf{W^{l-1}O^{l-1}}\right) \tag{2.18}$$

where $\mathbf{O^l} = \left[O_1^l,\ O_2^l, \cdots\ O_j^l, \cdots\ O_{n_{nu,l}}^l\right]^T$. $\mathbf{W^{l-1}}$ is the weight matrix which relates l^{th} layer and $(l-1)^{th}$ layer.

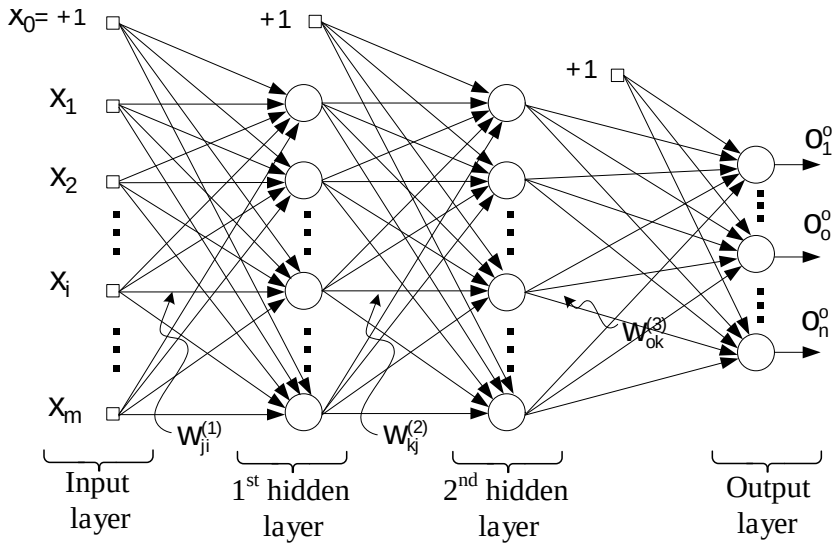

Figure 2.6: Architecture of a multilayer perceptron with two hidden layers. Here, inputs are x_1, x_2, ..., x_m and outputs are O_1^o, ..., O_o^o, ..., O_n^o.

$$\mathbf{W^l} = w_{ji}^l \quad for \quad \begin{matrix} j = 1, 2, , ..., n_{nu,(l+1)} \\ i = 0, 1, , ..., n_{nu,l} \end{matrix} \quad and \tag{2.19}$$

Then, the forward calculation of the feed-forward neural network can be given as,

$$\mathbf{O^o} = \phi\left(\mathbf{W^3}\phi\left(\mathbf{W^2}\left(\phi\left(\mathbf{W^1 x}\right)\right)\right)\right) \tag{2.20}$$

Back propagation learning procedure with gradient descent algorithm

Back propagation technique, adjust the weights in the direction opposite the instantaneous error gradient. Let ζ denote the error at the output layer, where:

$$\zeta \triangleq \frac{1}{2}\sum_{i=1}^{n_{nu,o}} (d_i - O_i^o)^2 = \frac{1}{2}\sum_{i=1}^{n_{nu,o}} e_i^2 \tag{2.21}$$

$n_{nu,o} =$ is the number of neurons in the output layer layer. Then gradient of ζ can be defined as,

$$g = \frac{\partial \zeta_k}{\partial \mathbf{w_k}} \tag{2.22}$$

Here, $\mathbf{w_k}$ is the vector of all weights of the whole network after k^{th} iteration. Then weight updation at $(k+1)^{\text{th}}$ iteration can be given as,

$$\mathbf{w_{k+1}} = \mathbf{w_k} - \eta g_k \tag{2.23}$$

where η is the scalar parameter called learning rate. This algorithm given in Equation (2.23), is called gradient descent algorithm. There is no guarantee that this algorithm brings the error to the global minimum.

Levenberg Marquardt algorithm

Levenberg Marquardt (LM) algorithm is used to have fast second order training without having computation of Hessian matrix (Matlab 2002). Here, the Hessian matrix of ζ, $\mathbf{H}$ is approximated as,

$$\mathbf{H} = \mathbf{J^T J} \tag{2.24}$$

where $\mathbf{J}$ is the Jacobian of ζ. Gradient, g can also be computed as,

$$g = \mathbf{J^T} e \tag{2.25}$$

$\mathbf{J}$ of ζ is computed using back propagation technique and hence computation of Hessian matrix is easy (Matlab 2002). Then, the LM algorithm can be shown with the given Hessian matrix approximation.

$$\mathbf{w_{k+1}} = \mathbf{w_k} - \left[\mathbf{J^T J} + \eta \mathbf{I}\right]^{-1} \mathbf{J^T} e_k \tag{2.26}$$

When η gets a larger value, this will be like gradient descent algorithm with a small step sizes. When η is very small, this will become Newton's method. More information can be found in (Matlab 2002).

2.2.3 Cross-correlation of signals from two plane tomographic systems

Cross-correlation function can be used to characterise against the variations in time lag between two initial signals. The time delay, τ, corresponding to the maximum value of cross-correlation function gives the transit time (τ_{max}) between two sensors assuming that there are no considerable changes in the signal within the short distance between two sensors. Cross-correlation of the periodic signals from sensor plane 1,S_{pl_1}, and sensor plane 2, S_{pl_2}, (from ECT or ERT) with the same fundamental frequencies can be explained mathematically as in Equation (2.27) below.

$$\rho_{S_{pl_1} S_{pl_2}} = \lim_{T \to \infty} \frac{1}{T} \int_0^T S_{pl_1}(t)\, S_{pl_2}(t-\tau)\, dt \tag{2.27}$$

where $\rho_{S_{pl_1} S_{pl_2}}$ is the cross-correlation function of S_{pl_1} and S_{pl_2}. T is the time span of signals. τ is the time lag between two signals.

This technique has been used to estimate the slug translational velocities by many researchers ((Al-Lababidi 2006)). Figure 2.7 illustrates how to select τ_{max} between given signals, S_{pl_1} and S_{pl_2}.

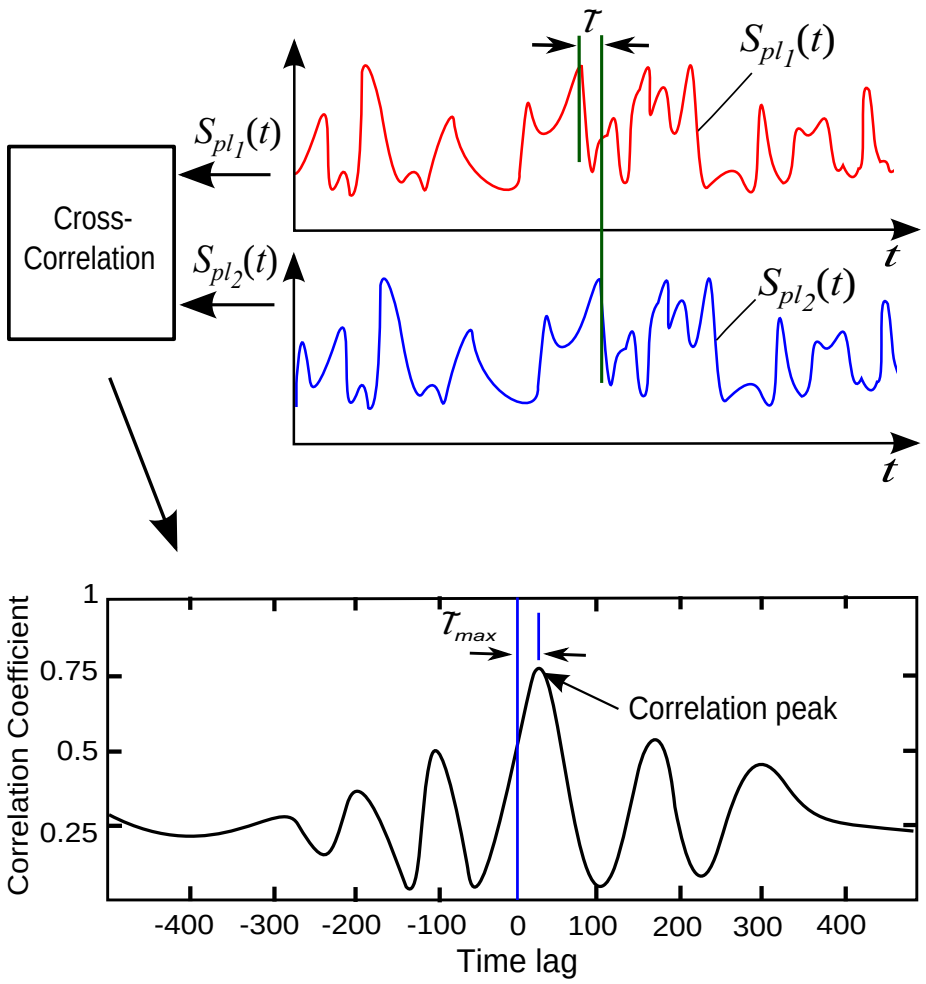

Figure 2.7: Cross-correlation technique to identify the time lag based on correlation peak

2.2.4 Power Spectral Density (PSD)

This technique has been used in many signal processing applications. This is a time series analysis method in frequency domain. Power spectral density (PSD) function produces power distribution of a signal along with corresponding frequency. Changes in volume fraction signal change the magnitude of the power spectrum and band width. These variations in PSD can be used in the estimation of dominant frequency of a flow signal. The ultimate output of this technique gives the relationship between signal powers against the frequency. Then, the frequencies which give higher power and lower power of the signal can be easily identified. The frequency at the strongest power is selected as the dominant frequency. Mathematically PSD can be defined

as Fourier transform of auto-correlation sequence of a time series data. Fast Fourier Transform (FFT) algorithm is used to transforms time domain signals to frequency domain where the dominant frequency can be extracted.

If z_n is a time series signal, z_k, the discrete Fourier transform of z_n can be given as,

$$z_k = \sum_{n=0}^{n_z-1} z_n e^{-j\frac{2\pi}{n_z}kn} \tag{2.28}$$

where $n, k = 0, 1, 2, ..., n_z - 1$ and n_z is the length of z_n. Then, the power spectrum can be given as;

$$F_{f_k} = \frac{1}{n_z} \sum_{k=-\frac{n_z}{2}}^{\frac{n_z}{2}} |z_k|^2 \tag{2.29}$$

where, F_{f_k} is the power spectrum of the signal z_k. $|z_k|$ is the magnitude of z_k. Power spectrum signal is symmetric and only the positive half of the spectrum is defined for positive frequencies. Frequencies of the power spectrum signal lies between $0 \leq f_k \leq f_{sam}/2$ (Figure 2.8). Here, f_{sam} is the sampling frequency of the signal z_n.

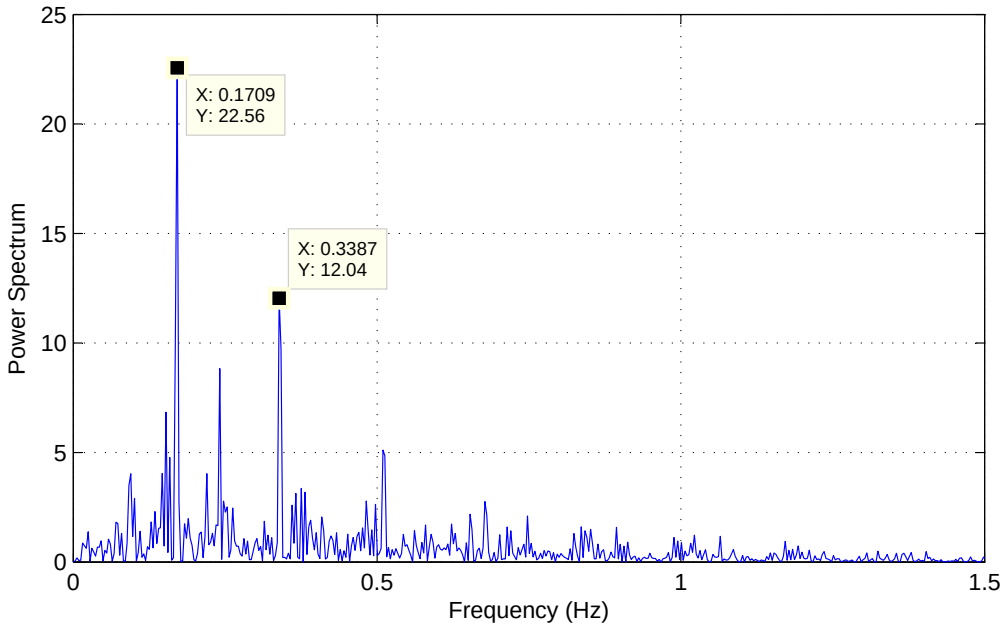

Figure 2.8: PSD technique to identify the dominant frequency of water volume fraction signal, α_w, with peaks at $0.17Hz$ and $0.34Hz$ in this case

Power spectrum plot of a typical water volume fraction signal of a slug flow, α_w (α is defined in Chapter 3) is shown in the Figure 2.8. Points correspond to the first two dominant frequencies are marked on the plot.

2.2.5 Dynamic Time Warping (DTW)

Dynamic Time Warping (DTW) technique is used to compare two time series signals. Here the warping path and two time series signals are defined as $P_w = (p_1, p_2, ..., p_{n_p})$, $x = (x_1, x_2, ..., x_{n_x})$, and $y = (y_1, y_2, ..., y_{n_y})$ respectively. n_x and n_y are number of elements in the x and y time series signals and n_p is length of the warping path. Warping path aligns the points in time series x and y in such a way that the distance between them are minimised. Squared distance between i^{th} element of x and j^{th} element of y can be defined as:

$$\delta(x_i, y_j) = (x_i - y_j)^2 \tag{2.30}$$

Similarly, calculating the local cost of each pair of elements of the signals x and y, a 2D matrix called distance matrix can be obtained. Figure 2.9 shows the distance matrix of a typical x and y time series signals and the Warping path, P_w.

The total cost function, Co_δ of a warping path between x and y signals with respect to δ can be defined as:

$$Co_\delta(x, y) = \sum_{k=1}^{n_p} \delta(x_i, y_j)_k \tag{2.31}$$

An optimal warping path between x and y is selected minimising the total cost function, $Co_\delta(x, y)$. The DTW distance, $DTW(x, y)$, between x and y is then defined as the total cost of P_w^* [3].

$$DTW(x, y) = Co_\delta^*(x, y) \tag{2.32}$$

$$DTW(x, y) = \min_{P_w} \sum_{k=1}^{n_p} \delta(p_{w_k}) \tag{2.33}$$

where, each P_{w_k} corresponds to a point $(i, j)_k$ of the cost matrix.

The DTW distance measure shown in Equation (2.33) is found using dynamic programming. Further information on dynamic programming and DTW can be found in Müller (2007) and Keogh & Pazzani (2000).

2.2.6 Eigenvalues of raw ECT measurements for flow study

Capacitance data matrix of a single ECT measurement frame can be arranged to have an upper triangular matrix, $\mathbf{C_m}$.

$$\mathbf{C_m} = \begin{cases} a_{i,j} = C_{i,j+1} & for\ i \leqslant j \\ a_{i,j} = 0 & for\ i > j \end{cases} \tag{2.34}$$

where $a_{i,j}$ is the element a at row and column indices i and j. $C_{i,j}$ is the normalised capacitance measurement between i^{th} and j^{th} electrodes, when i_{th} electrode is excited. $i = 1, 2, 3, ..., N_C$ and $j = 1, 2, 3, ..., N_C - 1$. $\mathbf{C_m} \in \mathbb{R}^{N_C \times (N_C - 1)}$

[3] * denotes the optimal

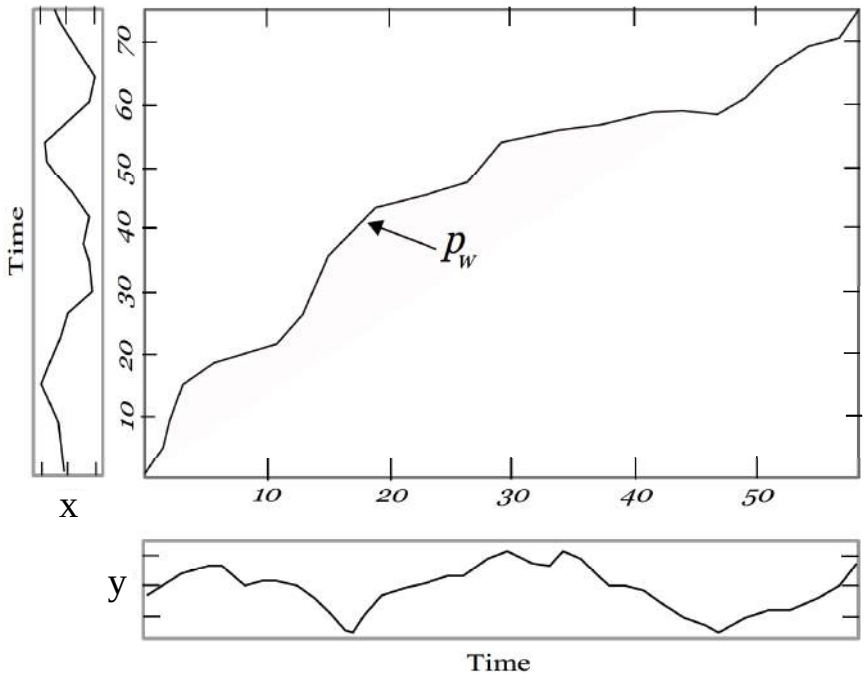

Figure 2.9: The distance matrix and warping path, p_w with two time series of signals

Since only independent inter-electrode measurements are captured by the ECT system, elements below diagonal of $\mathbf{C_m}$ are zero. Then, elements below diagonal are filled with available measurements by considering $C_{i,j} = C_{j,i}$ to construct a square matrix called constructed measurement data matrix, $\mathbf{C_{\tilde{m}}}$ (to make $\mathbf{C_{\tilde{m}}}$ a square matrix, last row of the $\mathbf{C_m}$ is removed at the beginning).

The matrix $\mathbf{C_{\tilde{m}}} \in \mathbb{R}^{(N_C-1)\times(N_C-1)}$ can simply be defined as;

$$\mathbf{C_{\tilde{m}}} = \begin{cases} a_{i,j} = C_{i,j+1} & for\ i \leqslant j \\ a_{i,j} = C_{i+1,j} & for\ i > j \end{cases} \tag{2.35}$$

Eigenvalues of these matrix $\mathbf{C_{\tilde{m}}}$ are then used in the studies in Chapter 6. (Strang 2009)

explains that a number (Ei) is an eigenvalue of a matrix $(\mathbf{C_{\tilde{m}}})$, if and only if $\mathbf{C_{\tilde{m}}} - Ei\mathbf{I_{ei}}$ is singular. This can be explained mathematically as,

$$det(\mathbf{C_{\tilde{m}}} - Ei\mathbf{I_{ei}}) = 0 \tag{2.36}$$

where det denotes determinant of a matrix (here $\mathbf{C_{\tilde{m}}} - Ei\mathbf{I_{ei}}$).

Since $\mathbf{C_{\tilde{m}}} \in \mathbb{R}^{(N_C-1)\times(N_C-1)}$, the Equation (2.36) gives $N_C - 1$ eigenvalues. However, all of them may not be dominant. Relationship between flow regimes and dominant eigenvalues have studied by (Fang & Cumberbatch 2005) with theoretical approaches. Three basic flow pattern and identification of them with the help of dominant eigenvalues can be given as presented in (Fang & Cumberbatch 2005).

1 Stratified flows

Leading eigenvalue Ei_d has a linear relationship with liquid height h_l. Next two eigenvalues Ei_2 and Ei_3 are more likely to have opposite signs. (Ei_d is the largest eigenvalue, Ei_2 and Ei_3 are second and third largest eigenvalues)

2 Annular flows

Leading eigenvalue Ei_d has a linear relationship with liquid fraction α_l. Next two eigenvalues Ei_2 and Ei_3 are approximately equal and have positive signs.

3 Core flows

Leading eigenvalue Ei_d has a linear relationship with liquid fraction α_l. Ei_2 and Ei_3 are approximately equal and negative.

This eigenvalue based method is further studied with experimental data as given in Chapter 5

2.3 Discussions of Techniques

All these techniques as presented in this study are mainly implemented offline, i.e. using logged data from different experiments. All data analysis was performed using MATLAB and dedicated toolboxes.

Only the main techniques used in this thesis work are briefly discussed in this chapter. Other techniques are briefed at the appropriate sections and chapters. More information on each technique or method can be found in the relevant references. In this study, analyzing is done with tomograms and tomometry using ANN, cross-correlation, PSD, and DTW. Whenever, it is possible comparisons of the performances of these methods are presented with focus on flow related parameters.

Chapter 3

Experimental set-up with sensors and instrumentation

All of the experimental works were performed in TUC. Test facilities, measurement systems and sensors used are described in the following sections of this chapter. Dynamic measurements were performed with the flow generated in the multiphase flow facility while static measurements were mainly performed with the same sensor arrangement but separately from flow facility.

A brief review of the basic parameters used in the flow experiments is given before describing the experimental set up and instrumentation.

3.1 Basic definitions in two phase flows

In gas-liquid multiphase flow experiments, inlet conditions of liquid and gas components are the only controllable parameters. Other basic quantities and definitions can be derived from inlet flow parameters with the known pipe cross-sectional information. If the gas flow rate is q_G and liquid flow rate is q_L, superficial velocity of each liquid (U_{SL}) and gas (U_{SG}) is defined as given in Equations (3.1) and (3.2).

$$U_{LS} = \frac{q_L}{A} \tag{3.1}$$

$$U_{GS} = \frac{q_G}{A} \tag{3.2}$$

the mixture velocity,U_{mix}, will be

$$U_{mix} = U_{GS} + U_{LS} \tag{3.3}$$

and liquid and air fraction (no slip), α_l and α_g, are defined as,

$$\alpha_l = \frac{q_L}{q_L + q_G} = \frac{U_{LS}}{U_{LS} + U_{GS}} \tag{3.4}$$

$$\alpha_g = \frac{q_G}{q_L + q_G} = \frac{U_{GS}}{U_{LS} + U_{GS}} \tag{3.5}$$

When liquid phase is water or oil, α_l is denoted as α_w or α_o respectively.

3.2 Multiphase flow facility

Simplified P and ID (Piping and Instrumentation Diagram) of the experimental flow rig used in this study is shown in Figure 3.1. The experiments were performed using liquid (oil or water) and air at room temperatures and atmospheric outlet pressure. The liquids are transparent mineral oil (Exxsol D60) and tap water with the properties given in Table 3.1. Oil and water are stored in separate tanks (T100 and T101 for oil and water, respectively, as shown in Figure 3.1) and circulated using volumetric pumps P100 and P101. Both water and oil flow rates below 80 kg/min can be selected from centrifugal pump P102 and volumetric pumps P103 and P104. Volumetric flow ranges of each pump are given in the Table 3.2. The mass flow, density and temperature were measured for each phase, before the components enter the test section using Coriolis flow meters. The test section is a 15m long steel pipe with inner diameter 56mm. Pipe inclination can be adjustable within the range of -10° to $+10^{\circ}$ to the horizontal. Liquid and air flow travel 12.5 m from the inlet of the test section to pass the first tomography sensor plane. Coriolis flow meters (FT109B, FT110, FT114B and FT115) provide high accuracy with uncertainty $\pm$ 0.01kg/min. Proportional Integral Derivative (PID) controllers implemented in LabVIEW controls the liquid flow rates.

Table 3.1: Properties of fluids used in experiments

Fluid	Density[kg/min]	Relative permittivity ε_r	Conductivity σ
Air	1	1	0
Water	996	$\approx$80	2mS/cm
Oil	790	2.7	0

Table 3.2: Pump specifications

Pump	Type	Flow rate [l/min]	Flow per revolution [ml/rev]	Fluid
P100	Positive displacement	80-428	946	Oil
P101	Positive displacement	80-542	1285	Water
P102	Centrifugal	1.74-13.9	3.48	Water/Oil
P103	Positive displacement	0.158-1.5	0.316	Water/Oil
P104	Positive displacement	0.455-4.2	0.910	Water/Oil

3.2.1 Differential pressure measurements

The outlet pressure of the test section is atmospheric due to storing of the fluids at the outlet of pre-separator tank before going to the gravity separator R100. Total differential pressure between points indicated by red arrows in Figure 3.2 is measured using pressure transducers PDT120 and PDT121. The system is capable of logging the pressure drop data up to the rate of 20Hz. These pressure measurements are more useful especially in the study of slug characteristics. Specifications of the pressure transducers are given in the Table 3.3.

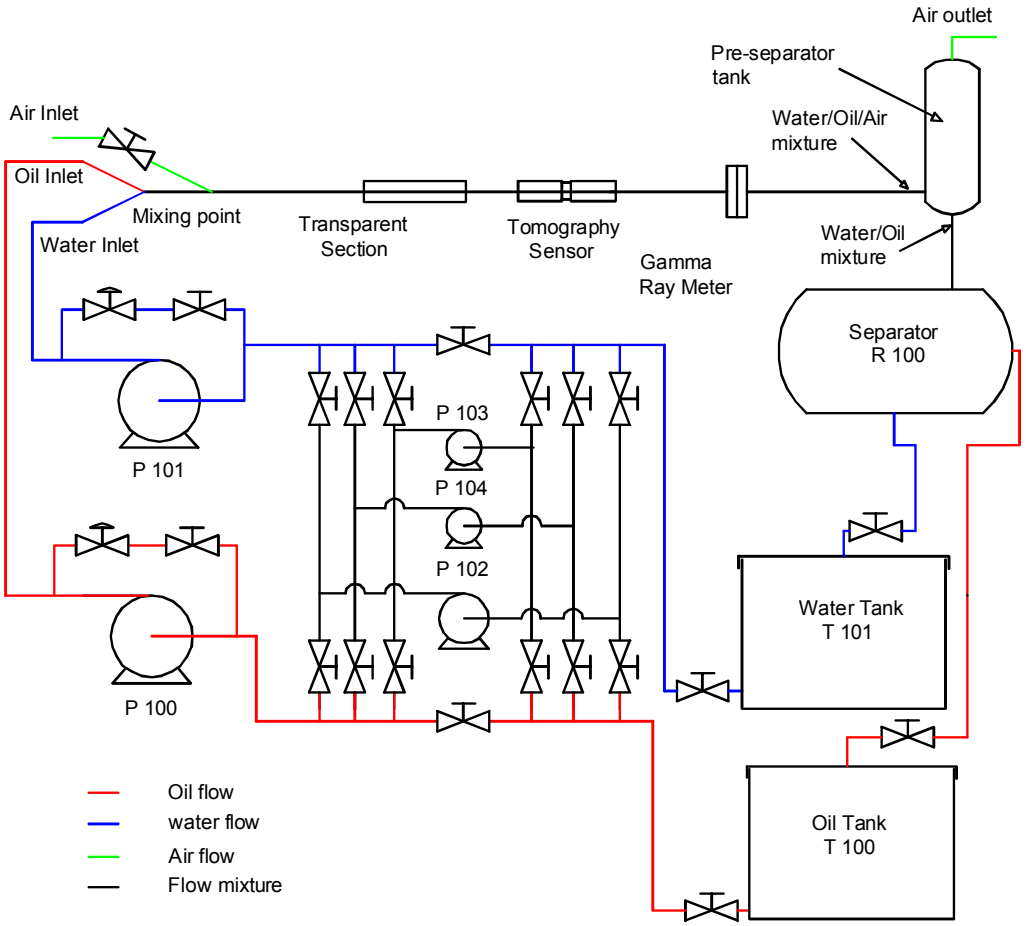

Figure 3.1: P and ID of the multiphase flow loop with installed tomography and gamma sensor systems as explained in (Pradeep et al. 2014) and (Kumara 2010)

Table 3.3: Sensors and transducers used in experiments with their respective measurement uncertainties

Transducer	Type	Model	Range [mbar]	Accuracy [mbar]
PDT120	Differential pressure	Rosemount 3051CD	0-100	±0.1
PDT121	Differential pressure	Rosemount 3051CD	0-50	±0.05
PT131	Differential pressure	Vika S-10	0-100	±2.5

3.2.2 Transparent section

A Plexiglas transparent section has been inserted to the test section about 10m from the pipe inlet. This section is very useful in visual observation of flow patterns and high-speed camera imaging. It had facilitated for Particle Image Velocimetry (PIV) measurements in previous flow studies (Kumara 2010).

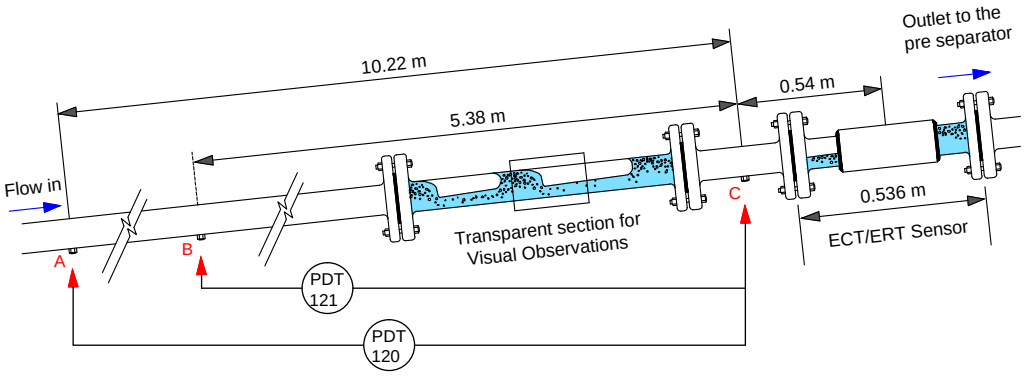

Figure 3.2: Test section with sensor placements as part of the tilted pipe with multiphase flow. Transparent section for high-speed camera based studies, multimodal tomographic system at the far right of the pipe section.

3.3 Tomographic systems and sensors

The sensor systems are going to be used in these research activities would mainly be ECT or ERT with commercially available measurement systems. Here, when the vessel or pipe wall is constructed from a dielectric material such as plastic or glass, the electrodes of the sensor can be located either inside, within or outside the vessel wall in the capacitance tomographic system. If the system is resistance or impedance tomography, the sensors must have contacts with the medium inside the vessel or pipe. When the measurement of the velocities is needed two plane of sensors are to be mounted.

3.3.1 Sensors used in experiments

Static measurements were mainly performed using 94mm diameter single plane ECT sensor. Other two sensors shown and explained in Figure 3.3 a), b) and Table 3.4 are used for measurements with multiphase flow experiments.

Table 3.4: Details of sensors shown in Figure 3.3

Type	No: of electrodes per plane	No: of planes	Internal diameter (mm)	Image
ECT	12	1	94	Figure3.3. a)
ECT	12	2	56	Figure3.3. b)
ECT/ERT Multimodal	12/16	2	56	Figure3.3. c)

a) b) c)

Figure 3.3: Tomography sensors used in the experiments. a) ECT sensor b) ECT/ERT multimodal sensor unit c) Multimodal sensor system mounted in the multiphase flow rig.

3.3.2 Commercial tomographic systems

PTL 300E ECT system from Process Tomography Limited was used in capacitance tomography measurements. Visualization is made on a 32×32 pixel layer. Measurement from two planes can be captured simultaneously. More information can be found in (PTL 2009).

System developed by University of Cape Town is used for ERT measurements. Up to 8, 16 electrode sensors can be coupled and operated with this system. This system utilises a switch DC current pulse technique to get high data capturing rates (Randall et al. 2008).

Table 3.5 summarises the systems and Figure 3.4 shows images of them.

Table 3.5: Tomographic instruments

Instrument	Model	No: of planes	Max: frame rate [fps]	Sensor type
ECT System	PTL300	2	100	8/12
Current pulse ERT system	UCT-ERT	8	37	16

3.4 High-speed camera

High-speed camera was used in flow visualizations. This motion PRO X camera can produce images up to 1000fps (fps - Frames per second) rate with 1280×1024 pixel resolution. However, due to the limited 4GB internal memory, capturing rate has to be lowered to get a series of images for a longer time. Capturing rate had to be reduced to 50fps to have 40s measurement period.

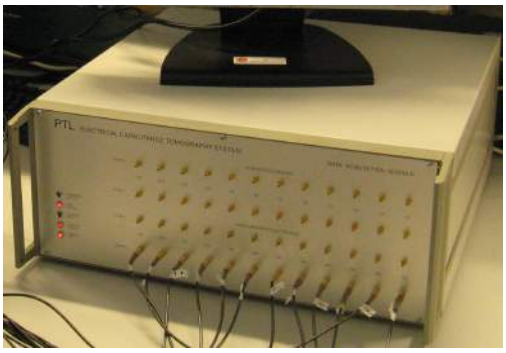

a)

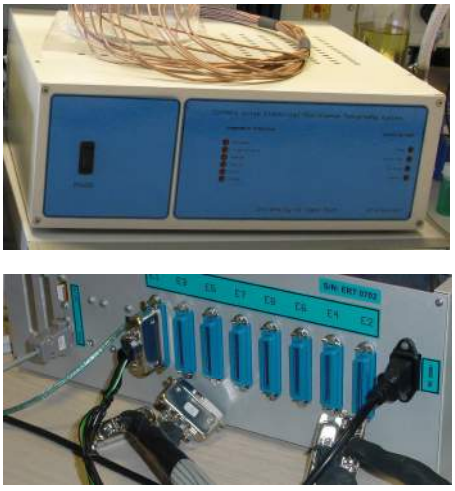

b)

Figure 3.4: a) PTL 300E ECT Module b) 8 plane ERT Module developed by UCT

Chapter 4

Interface detection

4.1 Introduction

In recent years, there has been renewed interest in multiphase flow separations and hence possibility of developing techniques to identify interfaces became an important part. Since the identification of interfaces is a part of flow regime studies, techniques developed can be used in addressing many problems related to flow regimes with other parameters. Possibility of fusion of measurements from different types of techniques can produce much improved and reliable estimations.

Since the ultimate goal of any tomographic system is to construct an image of a cross-sectional distribution of the materials filled in the sensor planes, tomograms can be used to select the interface parameter. Capacitance sensors can be found in interface measurements in many industrial process applications, such as identification of flow patterns, level detection in vessels with multiphase and multilayer and the volume percentage estimations of the different phases in conjunction with production, transport and storage of oil and gas in the petroleum industry (Primrose et al. 2010) and (Zorgani et al. 2010). There are many types of capacitance sensors for level measurements, (Yang & Peng 2003). Since most of the multiphase applications use circular pipes, cylindrical capacitance sensors explained in Chapter 3 are the most frequently used even for estimating levels in process measurements and control applications. Interface detection using ECT has become an interesting application particularly because of the fairly good experience with this established technique of level measurement using capacitance sensors (Bukhari & Yang 2006) and (Ismail et al. 2005). An ECT system, properly designed to encompass the process volume can be used in timely and fairly accurate measurements in process variables. These measurements can then be used in the estimations of parameters such as positions of the different interfaces and the volume fractions α of materials in the separator, (Isaksen et al. 1994). Common number of electrodes in an ECT sensor is 8 or 12, as the focus in ECT has been on generating better tomograms and parameter estimations based on them.

From the point of view of process control engineers, a very accurate tomogram generated using many electrodes and a long CPU time, is not always necessary, since the main focus is on timely actions needed to address crucial problems encountered in the process. Safety systems installed in oil and gas industries also need fast information from unpredictable complex flows

such as a series of slugs coming into the process vessel. Such information can be useful to avoid hazardous situations happened in "The Deep Water Horizon" off-shore platform in the Gulf of Mexico. In this chapter, the possibilities of using ANN based inferential methods along with measured inter-electrode measurements to estimate interface levels are explained.

This tomometric approach is then further extended to see the performances with reduced number of electrodes. Performance of a 12 electrode ECT system is assessed by studying its performance with only 6, 5 and 4 electrodes. The detection/estimation of interfaces is done effectively and in much shorter time compared to the processing of data with tomograms using a 12 electrode system. The inferential method can handle non-linearity and results from it can be easily integrated into other control algorithms addressing the actuators used in separators.

4.2 Interface levels in pipe separators

Interface level measurements of multilayer's in process vessels are still interesting in many industrial applications and academic researches. ECT has been used in interface identifications in three phase separators in recent studies done in the University of Manchester (Bukhari & Yang (2006), Dyakowski & Jaworski (2003)). Research groups in the University of Bergen have studied the detection of interface in bulky horizontal separators. A model based study has done by (Isaksen et al. 1994). Some relevant experimental results have been published by (Hjertaker et al. 2001a) and (Hjertaker et al. 2001b).

A new generation of separators is currently being assessed as a possible replacement of the bulky traditional horizontal separators. The current interest in these pipe separators has triggered interest in the use of ECT, ERT or multimodal tomography in separators, particularly in Norway. This interest in process tomographic methods for usage in pipe separators is very relevant. Recent studies done in Telemark University College have shown that process tomographic methods produce feasible engineering solutions for multi interface detection (Alme & Mylvaganam (2006), Alme (2007)).

These pipe separators have horizontal pipes of diameters in the range of 20–50 cm. A typical structure of a latest pipe separator is shown in Figure 4.1, with the possible localizations of the ECT sensors. In these pipe separators, layered flows are maintained and oil and water are separated in a very efficient manner (Alme 2007). The possibilities of getting fast interface level measurements are important. This has opened a window to ECT to enter the interface measurements due to its non-invasive and fast acquisition nature.

Some results based on lab scale experiments using ECT, performed on pipe separators with static and dynamic flows, are presented in this chapter. These results are based on experiments performed for detecting interface levels in pipe separators using the data driven soft sensor approach with artificial neural networks (ANNs). A very brief discussion on the concept of related soft sensors can be found in the attached Paper 1. The studies presented in this thesis are limited to the measurements and simulations run on lab models of pipe separators with diameters of 94 mm and 56 mm.

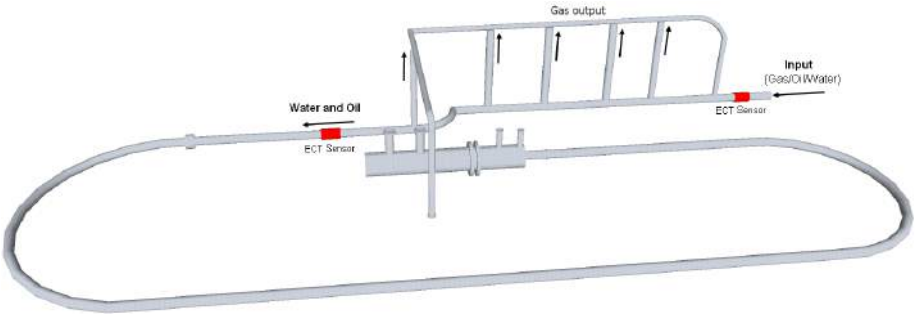

Figure 4.1: Pipe separator for the separation of three phases with suggested locations for ECT sensors as explained in (Ru et al. 2011) and (Alme 2007)

4.3 Capacitance values for varying interface distributions

Generally, the pipe separators are kept horizontally and contain all three phases, water at the bottom, oil in the middle and gas at the top, with unavoidable emulsions and foam as explained in (Alme 2007) and (Ru et al. 2010). After releasing the gas in the earlier stages of the separation, only water/brine and oil are to be separated.

In this experimental study, measurements were made mainly to acquire the inter-electrode capacitance measurements for varying levels of the two phases in stratified form as found in horizontal separator model shown in Figure 4.2.

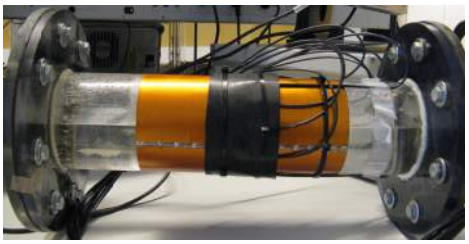

Figure 4.2: Separator section used in the experiments

Measurements were taken for level detection when two phases were present in the separator. The studies were performed for water-air, oil-air and water-oil two phases separately. For verification purposes, corresponding interface levels were measured manually for each and every sample acquired. Steps involved in the measurement procedure are:

- Filling the vessel completely with the low dense component (Air or oil) and acquiring capacitance measurements.
- Introduce the high dense component from the lower bottom part of the side flange, while letting the low dense component to flow out from the top.
- Increasing the high dense component to the separator Draining the low dense liquid out of the separator interface level increase Δh_l is maintained at approximately around 3 mm in each step.
- Recording the capacitance measurements and corresponding interface levels at each step.
- Repeating the second and third steps above, until the separator vessel is filled with high dense fluid.

During the first series of studies, experiments were performed with oil and water/brine alone (Air is the second component) with focus on the interface between them, i.e. estimating the interface height. Here, the electrode orientations should be unchanged during the whole experiment.

4.4 Tomometric approach for interface estimation

4.4.1 ANN based soft sensor approach

ANN can be structured to estimate the parameters related to material properties and geometrical positioning of the sensor. Since most of the separators are horizontal and fixed. The parameterisation can be simplified to estimate height of water or oil as follows;

Since interface height of the dense component, h_l is the only output; output of the ANN can be defined as,

$$h_l \in [0 \;\; D] \tag{4.1}$$

Inputs are inter-electrode capacitance measurements. Hence, N_C number of electrode sensor gives, $M = N_C\,(N_C - 1)\,/2$ number of inputs to the ANN.

$$\mathbf{c} = [C_{1,2} \cdots C_{i,j} \cdots C_{N_C-1,N_C}] \in \mathbb{R}^{M\times 1} \tag{4.2}$$

Then the measurements are arranged for training and validation sets of the model.

$$\begin{array}{ll} \mathbf{c_t} = [\mathbf{c_{t,1}},\, \mathbf{c_{t,2}} \cdots \mathbf{c_{t,n_{ct}}}] \in \mathbb{R}^{M\times n_{ct}} & h_{lt} = [h_{lt,1},\, h_{lt,2} \cdots h_{lt,n_{ct}}] \in \mathbb{R}^{1\times n_{ct}} \\ \mathbf{c_v} = [\mathbf{c_{v,1}},\, \mathbf{c_{v,2}} \cdots \mathbf{c_{v,n_{cv}}}] \in \mathbb{R}^{M\times n_{cv}} & h_{lv} = [h_{lv,1},\, h_{lv,2} \cdots h_{lv,n_{cv}}] \in \mathbb{R}^{1\times n_{cv}} \end{array} \tag{4.3}$$

where subscript t ans v indicate training and validation. n_{ct} and n_{cv} are length of training and validation data. Data matrices defined above are then calibrated based on the established normalization routine explained in Equation (4.4). Normalisation of the k_{th} sample of the capacitance and interface measurements is shown here.

$$\begin{aligned} \mathbf{c_{n,k}} &= (\mathbf{c_k} - \mathbf{c_{k,min}}) \,./\, (\mathbf{c_{k,max}} - \mathbf{c_{k,min}}) \\ h_{ln,k} &= (h_{lk} - h_{lk,min}) \,./\, (h_{lk,max} - h_{lk,min}) \end{aligned} \tag{4.4}$$

where ./ denote dividing each element in the vector $(\mathbf{c_k} - \mathbf{c_{k,min}})$ by the corresponding element in vector $(\mathbf{c_{k,max}} - \mathbf{c_{k,min}})$.

Then the normalised quantities are structured to be used in the ANN model training and validation as given in Equation (4.5).

$$\begin{aligned} \mathbf{c_{nt}} &= [\mathbf{c_{nt,1}},\ \mathbf{c_{nt,2}} \cdots \mathbf{c_{nt,n_{ct}}}] \in \mathbb{R}^{M \times n_{ct}} \quad & h_{lnt} &= [h_{lnt,1},\ h_{lnt,2} \cdots h_{lnt,n_{ct}}] \in \mathbb{R}^{1 \times n_{ct}} \\ \mathbf{c_{nv}} &= [\mathbf{c_{nv,1}},\ \mathbf{c_{nv,2}} \cdots \mathbf{c_{nv,n_{cv}}}] \in \mathbb{R}^{M \times n_{cv}} \quad & h_{lnv} &= [h_{lnv,1},\ h_{lnv,2} \cdots h_{lnv,n_{cv}}] \in \mathbb{R}^{1 \times n_{cv}} \end{aligned} \tag{4.5}$$

Depending on the success of the model, it can later be used for the estimation of parameter h_{ln} with new experimental data. Architecture of the ANN used is explained briefly in following sections.

4.4.2 ANN architecture

For different number of electrode sensors, ANN architecture has to be changed to get a better estimation, but two hidden layered architecture with tan-sigmoid activation function was used for all estimations. The selected architecture might not be optimum one with 12 electrode sensor measurements, but this was selected with the view of comparing different number of electrodes as explained in following sections. The selected architecture is shown in Figure 4.3. It has 15 and 5 neurons in first and second hidden layers. Number of electrode in sensor decides the number of inputs to the input layer. Input layer gets 6, 10, 15 and 66 inputs for selected 4, 5, 6, and 12 electrode sensors respectively. The only output of the network is interface level.

4.5 Estimation of interface level

4.5.1 Overview of the capacitance data

First, sample sets of absolute inter-electrode measurements were investigated to see the typical variations and then, the normalised values of capacitance measurement frames of each two phase flows are taken for the analysis. Figure 4.4 shows the absolute capacitance values and normalised values of air-water two phase flow level measurements. Typical "U" form and their deformations along with the interface changes can be seen with absolute measurements, but normalised data shows the increase of magnitudes against the interface level increases.

The normalised values of capacitance measurement frames of each interface levels of air-oil and oil-water can also be presented along with absolute measurements as did with air-water. Similar dynamics can be seen against the interface variations. The presentation of the measurement in Figure 4.4 is for information only. Relevant estimations and analysis are presented in the following sections.

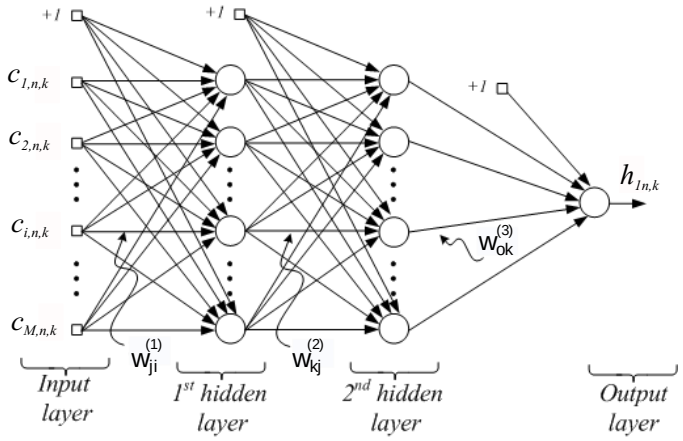

Figure 4.3: ANN architecture used in the estimations. Here inputs are normalised capacitance measurements ($\mathbf{c_{n,k}} = [C_{1,n,k} \cdots C_{i,n,k} \cdots C_{M,n,k}] \in \mathbb{R}^{M\times 1}$) and output is corresponding normalised interface height of the dense liquid ($h_{ln,k}$).

4.5.2 Results from ANN based interface detection

Figure 4.5 shows the level estimates produced using the ANN model for air-water, air-oil and oil-water two phase layered flows separately. The symbol '■' indicates the training data used in the ANN model development. '◊' represent the ANN estimates.

Root Mean Square (RMS) errors of validation were ±6 mm and ±3 mm for air-water and air-oil two phase level estimations. For oil-water experiments RMS was ±3 mm. Higher RMS uncertainty can be seen in air-water experiments. This is mainly due to the higher permittivity of water which can affect the capacitance values. Though RMS uncertainty involved with oil-water interface level shows ±3 mm which is similar to air-oil interface estimations, Figure 4.5 c) illustrates some data points with relatively larger deviations in comparison with air-oil. A larger number of data samples in the model training in oil-water experiments has helped to produce an improved model. This may also be a reason to have an improved estimation uncertainty over the air-oil combination.

4.6 Performances with reduced number of electrodes

As mentioned earlier, ECT technique and its development are mainly working for getting better cross-sectional images of the sensing area. However, image construction time may be a drawback in some applications where the fast acquisition is more important than accurate tomogram - especially in safety related applications and control applications. In such cases, information extracted from the raw measurements would be more useful. If the information needed is still with the reduced number of electrode sensors, it would be even better. How measurement speed

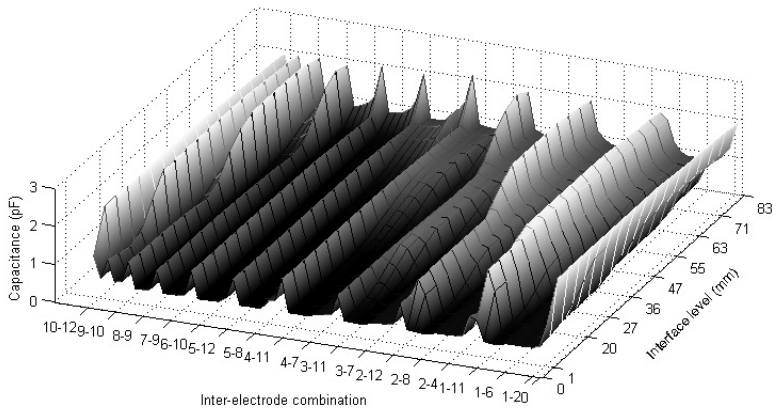

a)

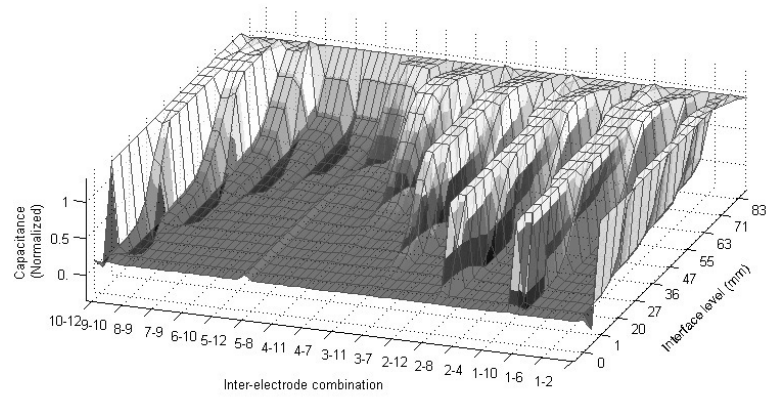

b)

Figure 4.4: Overview of a set of ECT measurements of water-air experiments a) Absolute capacitance values showing typical "U" shaped frame. b) Variations in Capacitance values after the normalization with some negative values

is improved with the reduction of the electrodes can be found in attached Paper 1 with more details.

Selected capacitance measurements for given 6 and 4 electrode sensors are shown in Figure 4.7. It can be seen in Figure 4.7 that even with the limited number of experiment points, relationship between capacitance measurements and interface level are observable.

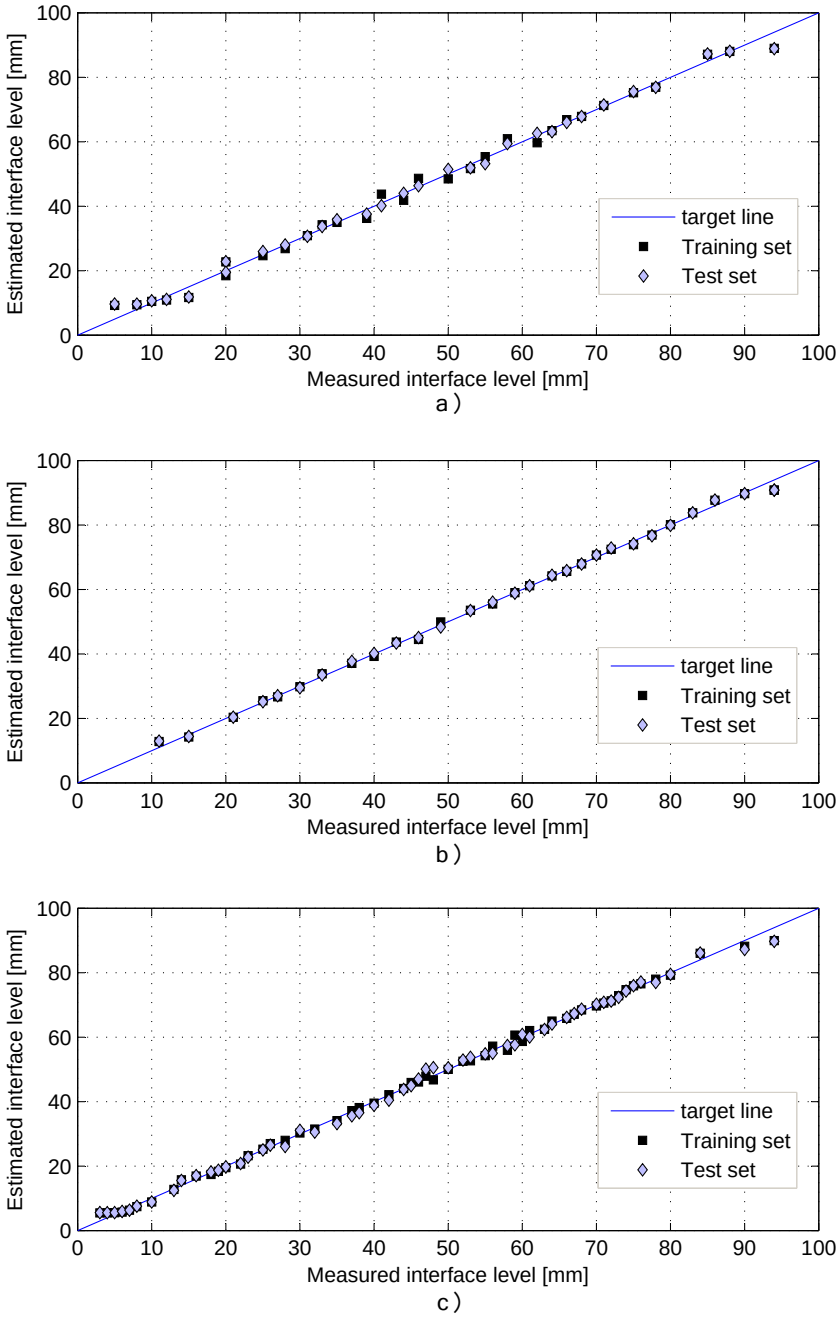

Figure 4.5: Estimate results for 12 electrode sensor, with calculated Root Mean Square (RMS) uncertainties ± 6 mm, ± 3 mm and ± 3 mm for each a) air-water b) air-oil and c) oil-water two phase flows

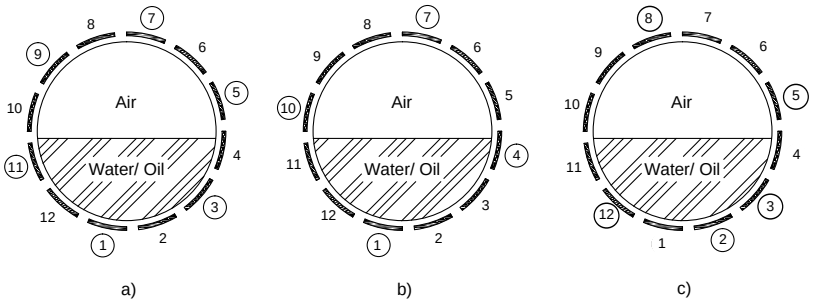

Figure 4.6: Schematic diagram of selection of electrodes a) symmetrically placed six b) symmetrically placed four c) asymmetrically five

Similarly, for asymmetric excitation of 5 electrode sensors shown in Figure 4.6 (c), inter-electrode capacitance measurements of the 2^{nd}, 3^{rd}, 5^{th}, 8^{th} and 12^{th} electrode combinations were chosen from 12 electrode sensor data. These data are used for training and validation in an inferential method based on neural networks available in MATLAB, neural network toolbox.

4.7 Estimation with 6 selected electrode sensor data

As given in the Figure 4.7 a) c) and e), distribution of inter-electrode measurement samples shows relatively strong dynamics in comparison to corresponding 4 electrode sensor selections.

Then, ANN model estimations for each two phase flow setup were developed preserving the same architecture explained in section 4.4.2.

4.7.1 Results from ANN based algorithms for interface detection

In comparison to the result produced by 12 electrode sensor model shown in Figure 4.5, estimations of 6 electrode sensor based model have higher uncertainty. When two phases are air-water or oil-water, interfaces below 20 mm gives higher uncertainties in estimations as shown in Figure 4.8. Though estimations above 20 mm are also showing some more deviations compared to the results with 12 electrode sensor based model, they are not so significant.

RMS errors of validation were $\pm$5 mm for air-water and oil-water two phases. It was $\pm$4mm for air-oil. Higher RMS uncertainties shown in air-water and oil-water experiments are mainly due to higher permittivity of water compared to the air and oil as stated earlier. Hence, the lower RMS uncertainty involved with air-oil estimations can be understandable. Figure 4.8 b) illustrates the estimation results, when air-oil are the flow components. in the detection of air-oil interfaces due to the values of permittivities of air and oil lying close to each other, certainty will be somewhat higher compared to the interface detection in the cases of air to water and oil to water transitions.

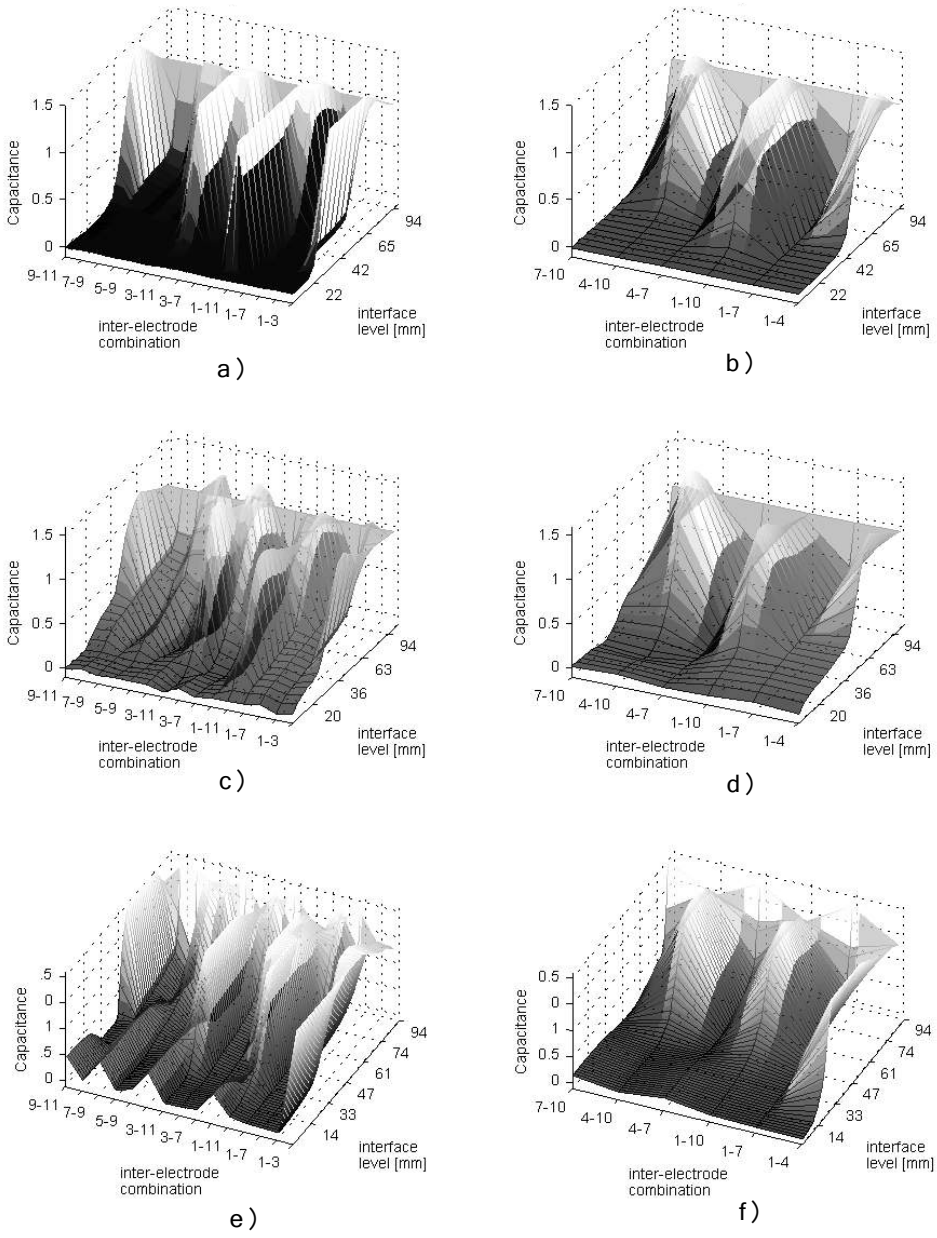

Figure 4.7: Overview of capacitance values for each 4 and 6 selected electrode sensors. a), b) from air-water two phase flows with 6 and 4 electrode sensors, c), d) from air-oil with 6 and 4 electrode and e), f) from oil-water with 6 and 4 electrode respectively

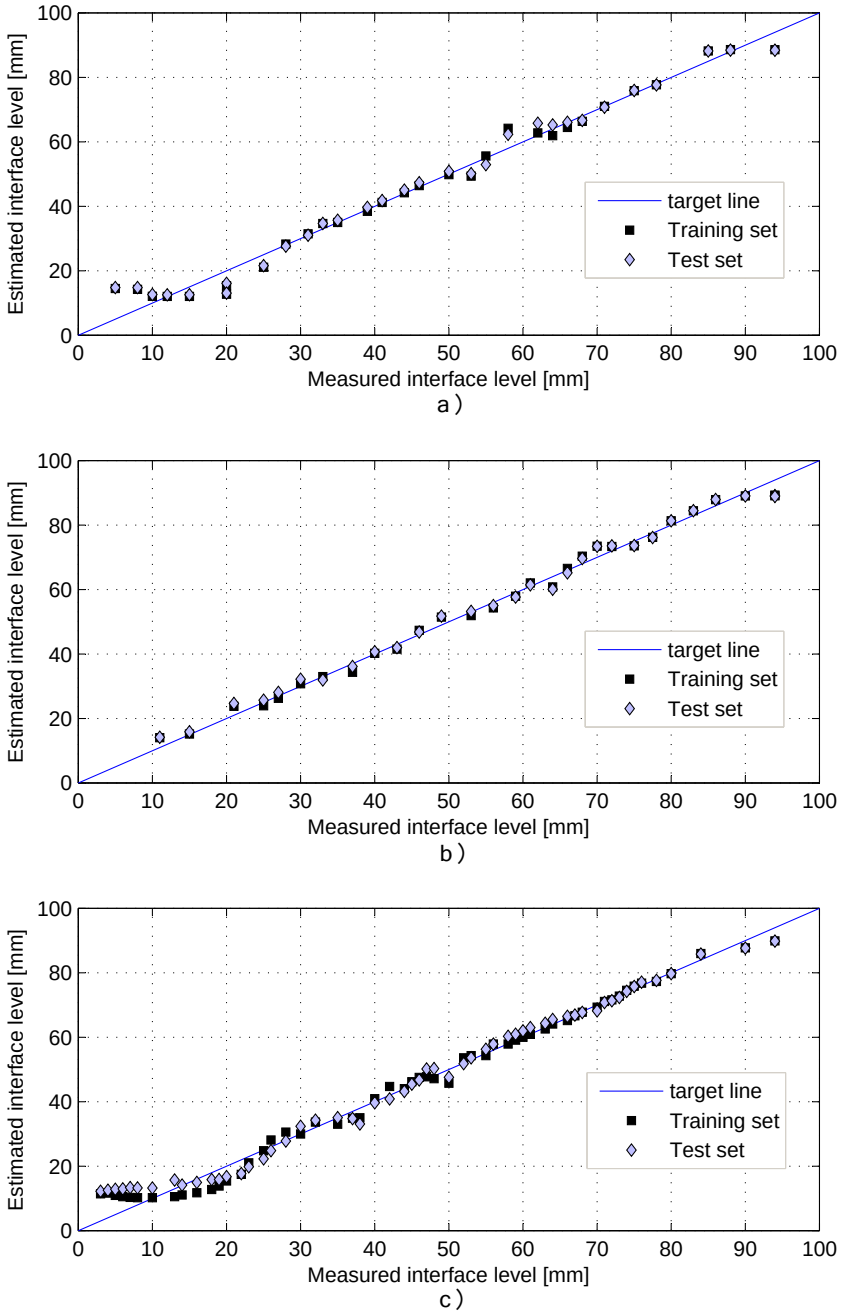

Figure 4.8: Estimate results for 6 electrode sensor, with calculated RMS uncertainties ±5 mm, ±4 mm and ±5 mm for each a) air-water b) air-oil and c) oil-water two phase flows

4.8 Estimation with 4 selected electrode sensor data

As shown in the Figure 4.7 b), d) and f), capacitance measurements equivalent to 4 electrode sensor have the least information, but it still shows that there is some useful information that can be used in the interface level estimations.

Figure 4.7 clearly shows how capacitance values are increased when interface level is increased. Hence, interface level estimations with ANN model are tested with all two phase combinations.

4.8.1 Results from ANN based algorithms for interface detection

Figure 4.9 a) shows the results related to the interface detection from air-water flow measurements by comparing the measured values against estimated values. ANN model shows an increased uncertainty in the ranges 20 mm to 50 mm and 55 mm to 70 mm of water levels. RMS based uncertainties are $\pm$7 mm for air-water flow and $\pm$5 mm for air-oil flows.

RMS uncertainty of oil-water combination is $\pm$6 mm. It is bit higher compared to air-oil case. Uncertainty has increased with the reduction of the electrode combinations as expected. In addition to the 6 electrode case higher uncertainties can be seen around 15 mm and 30 mm water levels.

4.9 Asymmetric electrode arrangement

Possible selections of asymmetric electrode arrangements for the ANN based interface estimation are studied. 5 electrodes selected from 12 electrode sensor are 2^{nd}, 3^{rd}, 5^{th}, 8^{th} and 12^{th} for this study (Figure 4.6). Results are more similar to the 6 selected electrode sensor, when two phases are water and air. 6 selected electrode sensor model shows the largest RMS uncertainty at around interface height 10 mm, but 5 electrode sensor based model does not show sensitivity till interface level reaches 30 mm.

When two phases are air-oil, 5 electrode sensor model shows results similar to corresponding 6 and 4 electrode systems. Largest RMS error 10mm is observed at interface height 12 mm. Results shown in Figure 4.10 clearly indicate that 5 electrode based model produces better estimation compared to the 4 selected electrode model (Figure 4.9).

Same can be observed with the results of air-water two phase model. Slopes of the regression line of estimated vs. measured interfaces and RMS errors have been included in the Table 4.1. Among many possible 5 asymmetric electrode selection combinations, 2^{nd}, 4^{th}, 5^{th}, 7^{th} and 10^{th} was also studied and results were included in the Table 4.2 with Root Mean Square Error (RMSE) values. This was done mainly to see whether the electrode position affects the estimations.

4.10 Execution times of the ANN

The time taken by ANN to produce the estimations is considered as the execution time. The reduction of execution times in algorithms with many repeat runs in a program is crucial in

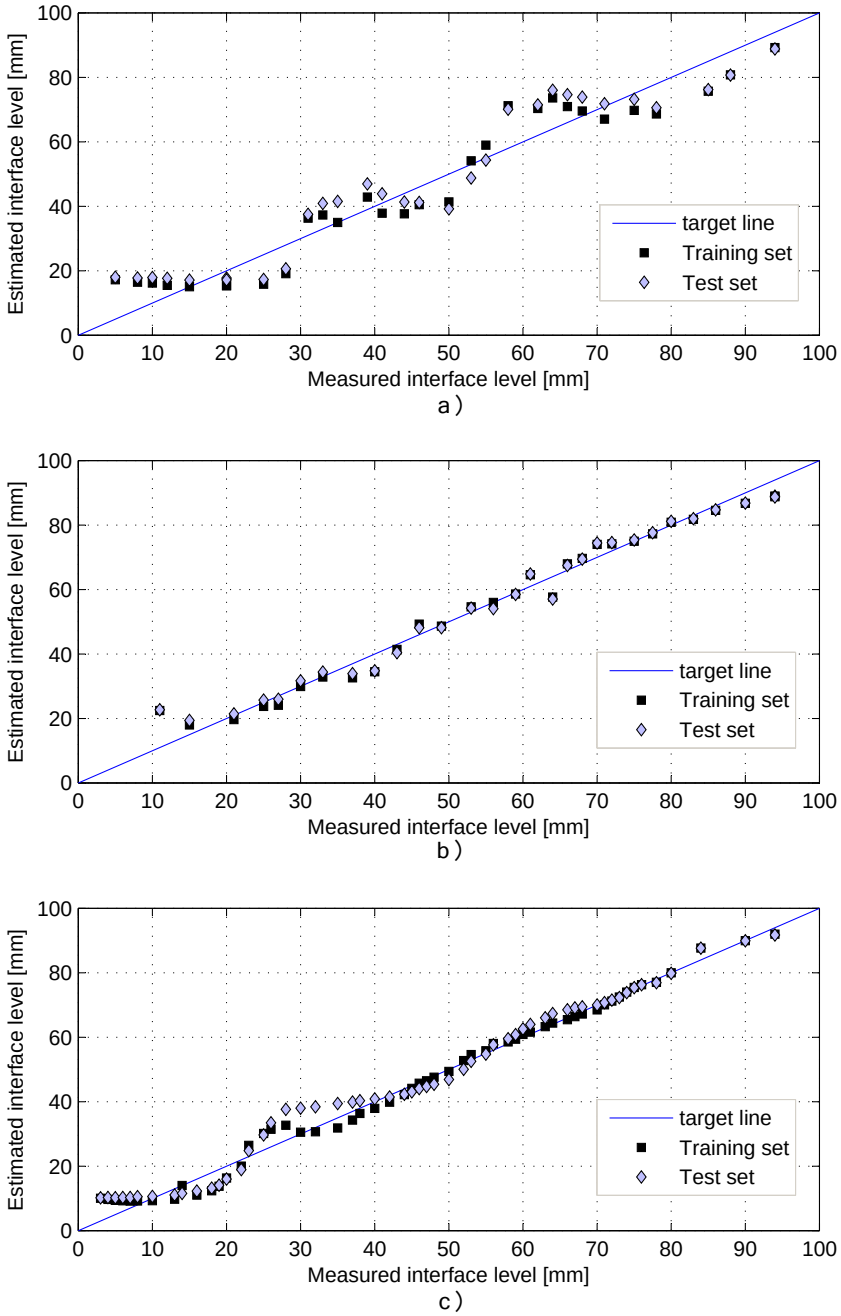

Figure 4.9: Estimate results for 4 electrode sensor, with calculated RMS uncertainties ± 7 mm, ± 5 mm and ± 6 mm for each a) air-water b) air-oil and c) oil-water two phase flows

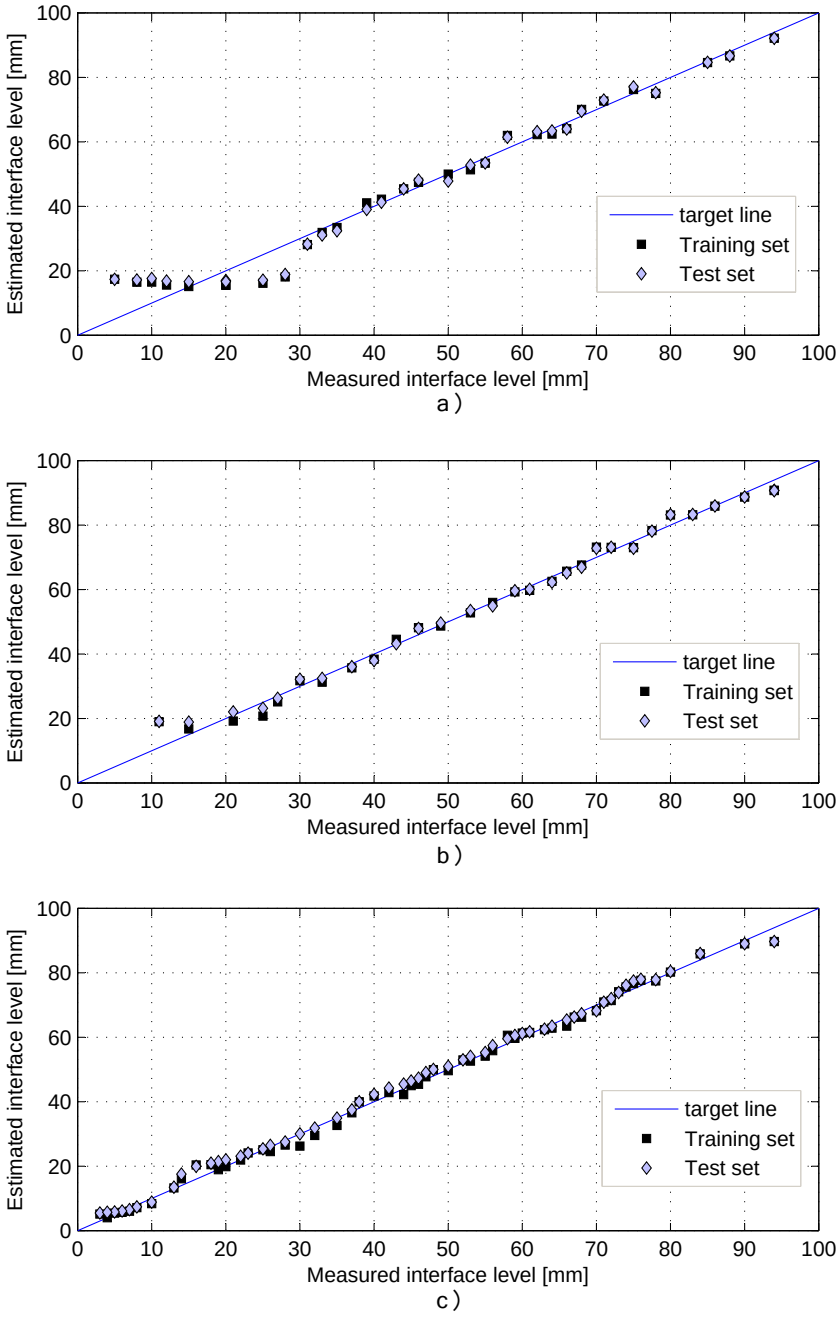

Figure 4.10: Estimate results for 5 electrode sensor, with calculated RMS uncertainties ± 8 mm, ± 5 mm and ± 5 mm for each a) air-water b) air-oil and c) oil-water two phase flows

Table 4.1: Root mean square error estimates from actual measurements and ANN estimates

Phases	No: of electrodes		Training	Validation
Water Air	12	RMSE	4 mm	6 mm
		Slope	0.97	0.95
	6	RMSE	4 mm	5 mm
		Slope	0.98	0.91
	5	RMSE	6 mm	8 mm
		Slope	0.98	0.92
	4	RMSE	5 mm	7 mm
		Slope	0.93	0.91
Oil Air	12	RMSE	2 mm	3 mm
		Slope	0.97	0.95
	6	RMSE	3 mm	4 mm
		Slope	0.96	0.96
	5	RMSE	3 mm	6 mm
		Slope	0.97	0.97
	4	RMSE	3 mm	5 mm
		Slope	0.96	0.94
Water Air	12	RMSE	3 mm	3 mm
		Slope	0.98	0.96
	6	RMSE	4 mm	5 mm
		Slope	0.97	0.96
	5	RMSE	5 mm	6 mm
		Slope	0.96	0.97
	4	RMSE	5 mm	6 mm
		Slope	0.97	0.94

Table 4.2: Root mean square error estimates with different electrode selection

Phases	No: of electrodes	Electrode selection	RMSE
Water Air	6	2-4-6-8-10-12	5 mm
	5	2-3-5-8-12	8 mm
	5	2-4-5-7-10	10 mm
	4	2-5-8-11	7 mm
Oil Air	6	2-4-6-8-10-12	4 mm
	5	2-3-5-8-12	6 mm
	5	2-4-5-7-10	6 mm
	4	2-5-8-11	5 mm

achieving better and fast response in real time applications of ECT or ERT systems. Then the information can be easily integrated with other measurements to be used in the applications such as flow control and flow prediction.

Relationship between number of measurement inputs and the time taken by the interface

estimation model is studied here. It is clear that the same ANN network architecture is used after weight training in the estimation. Hence, the time taken by estimation depends only on the forward calculation time of trained model. Time involved with the forward path of this ANN model can be calculated using Equation (4.6) as did in (Vuurpiji 1998). A simplified equation for the estimation time is given in (4.7).

$$T_{ANN} = \sum_{l=2}^{n_{lay}} \left(n_{nu,l} \left(\left(n_{nu,(l-1)} + 1 \right) \left(T_{add} + T_{mul} \right) + T_{fun} \right) \right) \tag{4.6}$$

$$T_{ANN} = n_{con} \left(T_{add} + T_{mul} \right) + \left(n_{nu,h} + n_{nu,o} \right) T_{fun} \tag{4.7}$$

where, n_{lay} is the number in layers of ANN, and n_{con} is the number of connections. $n_{nu,l}$ represents the number of neurons in l^{th} layer. $n_{nu,h}$ and $n_{nu,o}$ are the number of hidden and output neurons in the network. T_{add}, T_{mul} and T_{fun} are the times taken for performing addition, multiplication and executing the activation functions respectively.

Estimation models used in 12, 6, 5 and 4 electrode sensors have same structure except the number of inputs. Hence, only the number of connections,n_{con} are different. For 12, 6, 5 and 4 selected electrodes models, n_{con} would be 1091, 326, 251 and 191 respectively. These numbers of connections make the difference in addition and multiplication times involved among each models.

4.10.1 Estimation of execution time

Each trained ANN model was run for 6000 times and average time taken was selected and results from each model are included in Table 4.3.

Execution times were separately calculated using the Equation (4.7). Here T_{fun}, T_{add} and T_{mul} needed were measured independently by running those operations separately for 1×10^7 times. All these calculations and estimations were performed in MATLAB platform on a dual core personnel computer with 2.8 GHz CPU clock frequency and 4GB RAM. Implementation in a parallel processing architecture can lower the estimation time.

Relationship between number of connection and the execution time was then studied separately. Both theoretical and experimental results are shown in the Figure 4.11. Here, only the number of connections in the input layer is changed while keeping the remaining architecture unchanged. Both results indicated that the relationship between execution time and the number of network connections is linear.

Table 4.3: Total time required for estimation of one sample

No: of electrodes in sensor	Estimation time (μs)	
	Theoretical	MATLAB ANN
12	8.1	9.87
6	3.4	5.95
5	2.84	5.91
4	2.25	5.7

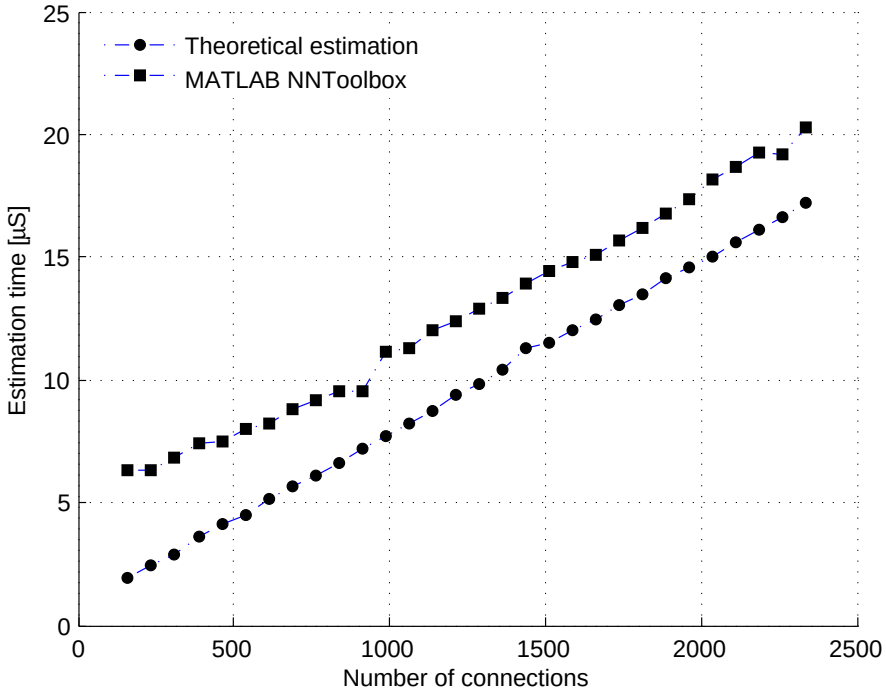

Figure 4.11: ANN estimation time, with the number of inputs changed and the rest of ANN architecture unchanged

Then the studies extended further to investigate the relationship between number of hidden neurons in each layer and execution time. Two hidden layered networks used for 12, 6 and 4 electrode sensor based estimations were studied separately. Here, all possible combinations of hidden neurons in two layers were taken in to account as clearly shown in Figure 4.12. Figure clearly shows how execution time varies with the different combinations of the hidden neurons. Meshes correspond to each models show that execution time is increased when number of inputs increased. Figure 4.13 shows the simplified representation of what was given in Figure 4.12. It can be clearly seen from the figure that for all three models, the relationship between execution time and the number of hidden neurons are linear. This has been fist investigated by (Alme 2007) with three layered ANN. It can be further extended that at least with 4 layered ANN networks number of hidden neurons has a linear relationship with execution time and it is independent of the number of layers.

As mentioned earlier, the architecture used may not be the optimal for the estimations, since it was preserved for the comparison of the models. More simplified architectures may be possibly specially with the measurement from a fewer number of electrodes. This was just checked with 6 and 4 electrode sensors and results are shown in Figure 4.14. Here, the hidden layers were assigned 12 and 9 neurons respectively. The two phases used in this study were oil and air.

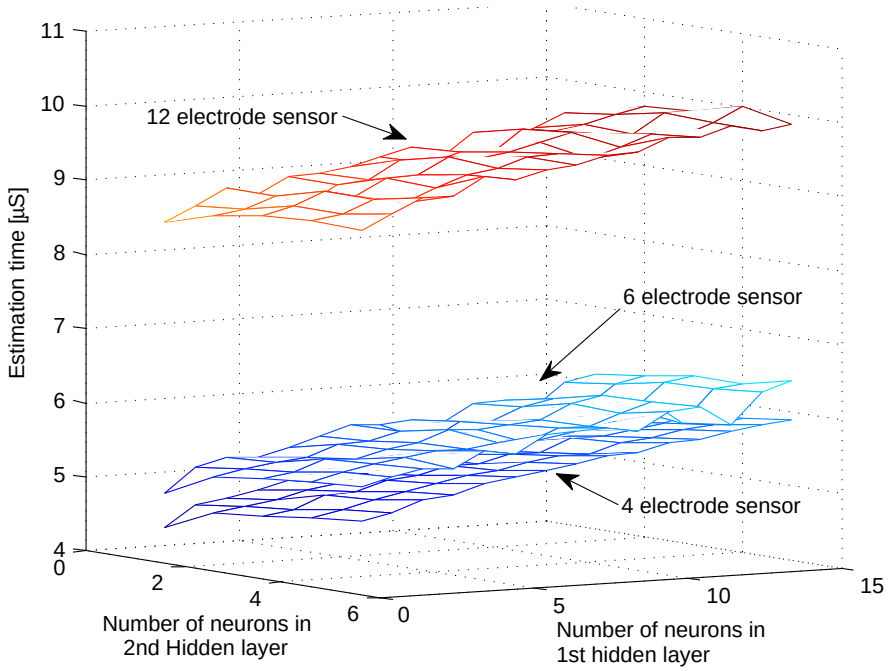

Figure 4.12: ANN estimation time when combinations of hidden neurons in each layer are changed

4.10.2 Uncertainty of estimation time

As stated in a previous section the time taken by ANN models to produce estimations are calculated by running each model a number of times and averaging. Here, for the Standard deviation calculations, it was run for 500 times in MATLAB and mean estimation time, $\mu_{T_{ANN}}$ and standard deviation, $STD_{T_{ANN}}$ of each ANN model were included in the Table 4.4. It can be seen that despite varied average estimation time involved with each models, RMS uncertainty is more similar to each other, except 12 and 4 electrode sensors with dynamic measurements.

Table 4.4: Time taken in the forward calculation of ANNs with different number of inputs

No: of electrodes in sensor	ANN estimation time (μs) $(\mu_{T_{ANN}} \pm STD_{T_{ANN}})$	
	Static measurements	Dynamic measurements
12	9.87 ± 0.30	10.1 ± 0.06
6	5.95 ± 0.25	5.23 ± 0.23
5	5.91 ± 0.30	4.92 ± 0.44
4	5.7 ± 0.22	4.5 ± 0.61

Lowest estimation time is achieved with the estimations based on 4 electrode sensor as expected.

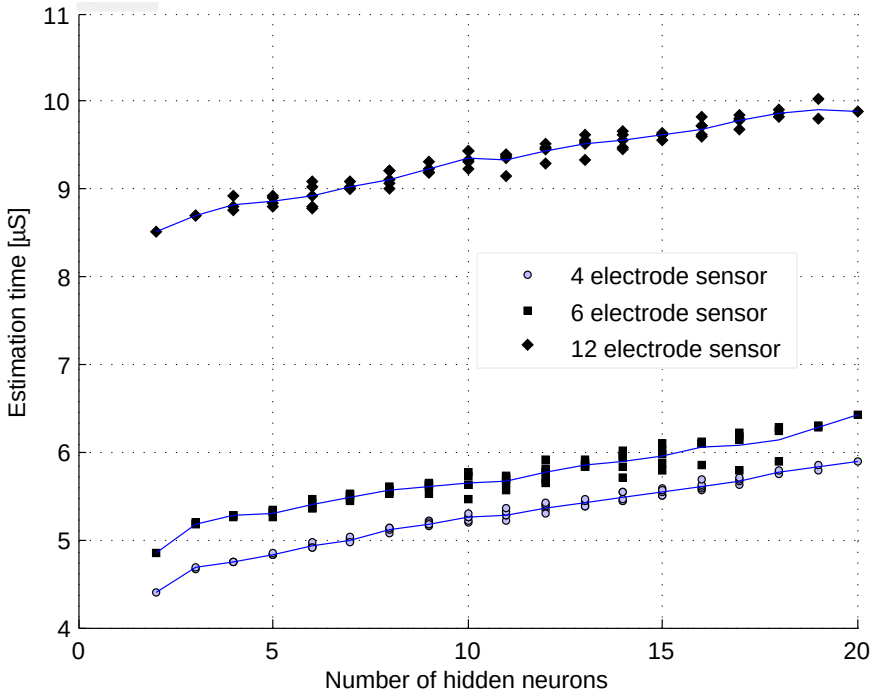

Figure 4.13: ANN estimation time variation against the number of inputs as given in (Figure 4.12)

4.11 Performance with two phase dynamic flows

Interface estimation of dynamic flows was studied for air-water two phases. Flow was generated in the multiphase flow facility at HIT and ECT measurements were captured. Inlet water and air flow conditions were 40 kg/min and 0.01 kg/min. Flow was $+1^{\circ}$ upwardly inclined flow in 56 mm diameter pipe. Here, the interface height was calculated using pipe geometry and liquid fraction, α_l. Results with 4 and 6 electrode sensor selection can be found in attached Paper 1. ANN estimation times with dynamic flows given in Table 4.4, are also from this experimental results. The inter-electrode measurements were captured in real-time, though ANN models were run in offline. But this approach is good enough to show that these real-time estimations will also produce good results.

4.12 Comparison of Interface estimations

Interface measurements in horizontal and near horizontal flows are being studied at HIT for many years. Gamma ray densitometry and PIV measurements were used in the experimental studies by (Vestøl & Melaaen 2006). Some of his results with gamma ray densitometry were compared with the ECT images as explained in this section. Two phase flows (Gas-liquid) in horizontal pipe and 1° downward pipes were studied with ECT measurements. A typical tomogram of ECT along with a vertical beam GRM at the mixture velocity U_{mix}, of 5 m/s and

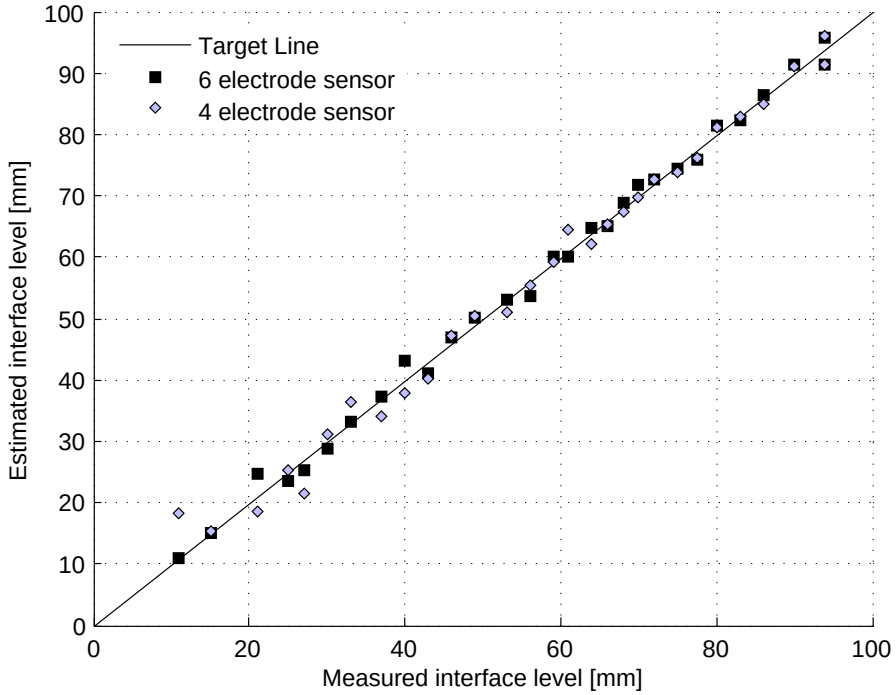

Figure 4.14: Estimation with better ANN architecture for 4 and 6 electrode sensors

liquid fraction α_l, of 0.01 are shown in the Figure 4.15. Air-oil interface can be clearly visible with both ECT and GRM results under given inlet conditions. It is around position 0.5 (as given in the figure) even the camera image captured through the transparent section proves the validity as shown in Figure 4.16.

Air-oil two phase flows

Flows in horizontal pipes are studied with 5 different oil fractions α_o. They were 0.001, 0.0025, 0.005, 0.0075 and 0.01. Mixture velocities U_{mix} were maintained at either 5 m/s or 10 m/s depending on the experiment. Results with both GRM and ECT techniques are shown in Figures 4.17 and 4.18. ECT based Interface profile indicates deviations either upward or downward near the pipe wall. Unlike in the GRM measurements, the interface profile is bending downward for the low oil fractions, 0.001 and 0.0025 . GRM measurements show more uniform interface levels throughout the pipe cross-section, but curves upward at the pipe wall. Both techniques correctly indicate that increase in oil fraction α_o at both mixture velocities U_{mix}, 5 m/s and 10 m/s would increases the interface level height. Figure 4.19 shows both GRM and ECT based calculation of interface levels. It can be clearly observed that the ECT image (pixel) based calculations always stay above the GRM based calculations. When interface level goes down, the difference in the interface levels using these two techniques increases. Uncertainties involved with each ECT calculations and Camera images evidence that these layered flows are wavy stratified.

The same sets of experiments were performed with 1° downward flows with the same set

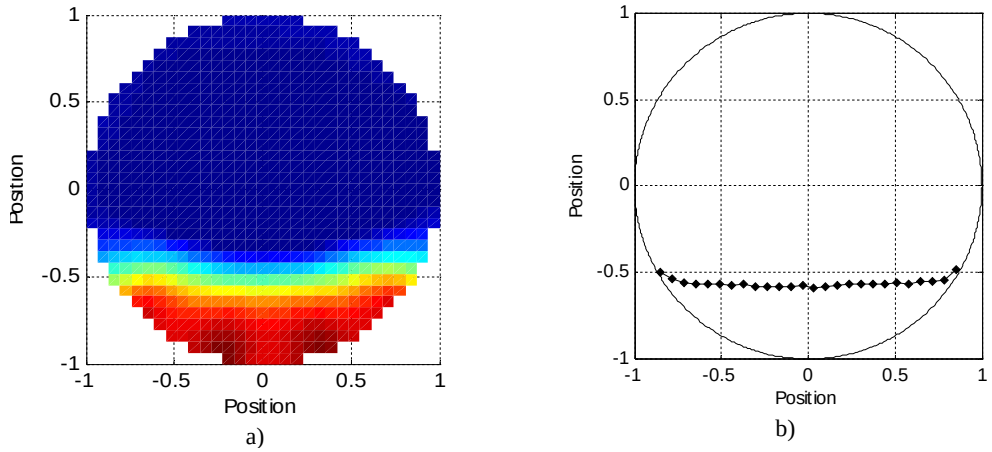

Figure 4.15: ECT and GRM measurements of horizontal flow with mixture velocity, U_{mix}, of 5 m/s and oil fraction, α_o, of 0.01. The interface levels are clearly seen to be around position -0.5

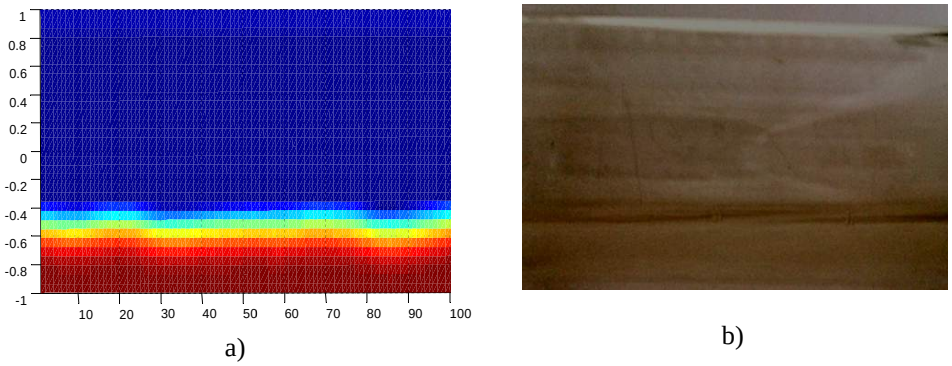

Figure 4.16: a) ECT measurements for horizontal flow with mixture velocity, U_{mix}, 5 m/s and oil fraction, α_o, 0.01. b) A still camera image of a corresponding flow

of oil fractions. Results are shown separately for mixture velocities U_{mix}, of 5 m/s and 10 m/s in Figures 4.20 and 4.21. ECT based interface profile clearly shows downward deviations near the pipe wall as observed with horizontal flows. The similarities in interface profile from both techniques can be clearly seen and the trends discussed in the case of horizontal flows are seen here too. Interface level increases with the increase of oil fractions α_o, but compared with the horizontal flows interface heights are less.

Comparison of GRM and ECT based estimations are given in Figure 4.22. As observe with horizontal flows, ECT base calculations give slightly higher interface heights and uncertainties involved are larger than horizontal flows. However, the two measurement methods show a ten-

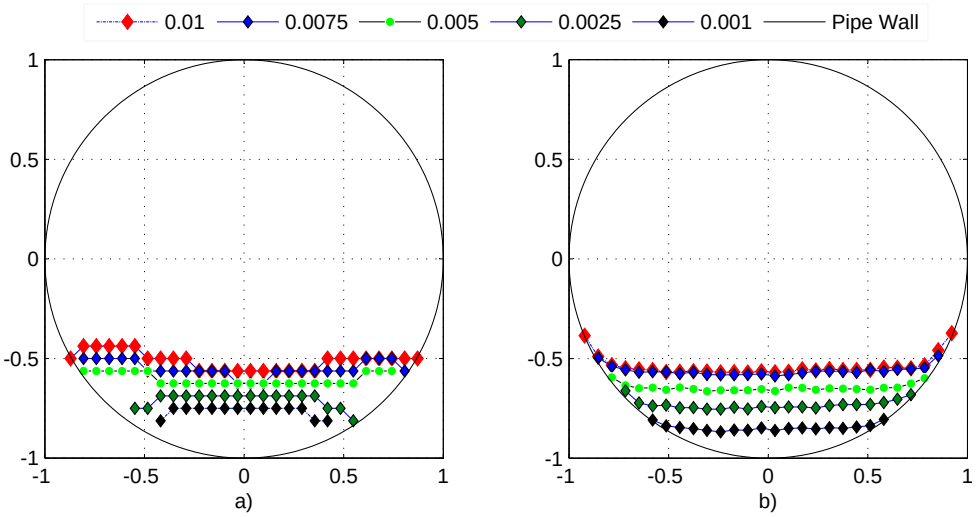

Figure 4.17: Interface level measurements with ECT (left) and vertical beam GRM (right) for air-oil flows with mixture velocity, U_{mix}, 5 m/s and different liquid fractions, α_l, when pipe inclination is 0°. Oil fractions, α_o, used are given in legend on top

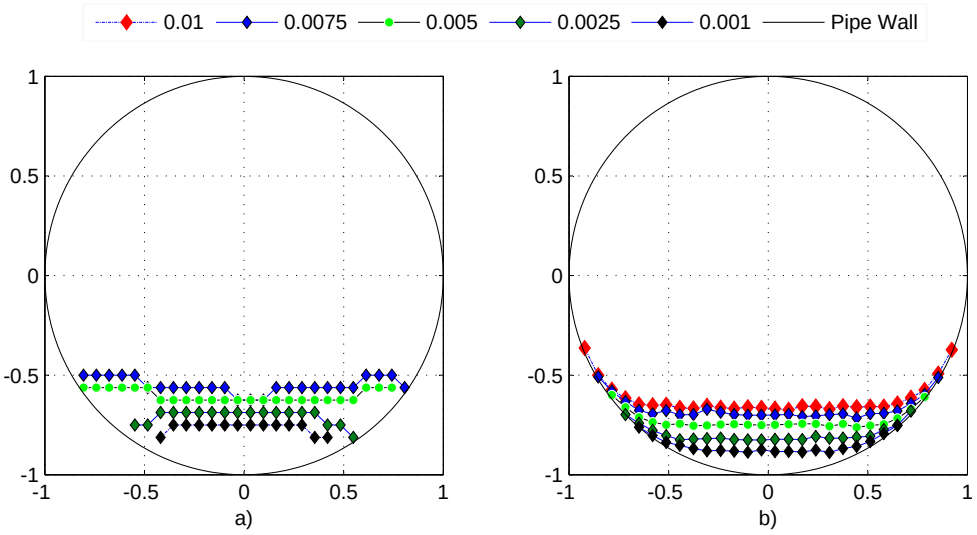

Figure 4.18: Interface level measurements with ECT (left) and vertical beam GRM (right) for air-oil flows with mixture velocity, U_{mix}, 10 m/s and different liquid fractions, α_l, when pipe inclination is 0°. Oil fractions, α_o, used are given in legend on top

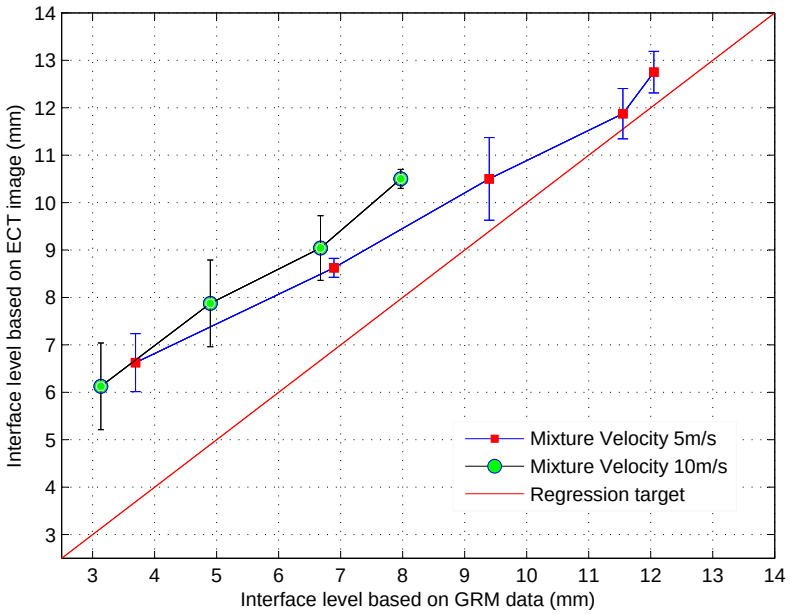

Figure 4.19: Interface levels based on ECT and GRM for horizontal flows with RMS uncertainties

dency to give a higher estimate of the interface levels when comparing them with the interface levels obtained from external measurements performed through the transparent pipe section.

This may be attributed to wetting of the pipe walls by the oil in this set of experiments. Both techniques show higher interface levels compared to the level observed through camera images. As (Vestøl & Melaaen 2006) explained, gamma ray passing through the middle of the pipe has less uncertainty. It will increase when come closer to the wall, because a large portion of the Gamma beam occupies the pipe wall. More details can be found from (Kumara 2010) and (Vestøl & Melaaen 2006). Mainly due to soft-field effect, ECT tomograms get distorted and it results the unclear interface boundaries. Since only 32 layers of pixels cover the whole pipe cross-sectional height, spatial resolutions goes down and increases the uncertainties in interface level and α calculations.

GRM results show the interface curvature near the pipe wall in all experiments. As explained by (Vestøl & Melaaen 2006), the measurements near the wall were performed using angular gamma beams through the pipe center. GRM Results show that the interface is uniform except the near the pipe walls. This may be due to wetting of the pipe wall, which is not so easy to observe.

Comparison of these ECT and GRM techniques is given in the Table 4.5. GRM used in these measurements is no match with the ECT when speed of the measuring is vital. However, long measurement time taken by the GRM makes the measurements much accurate. Speed of the

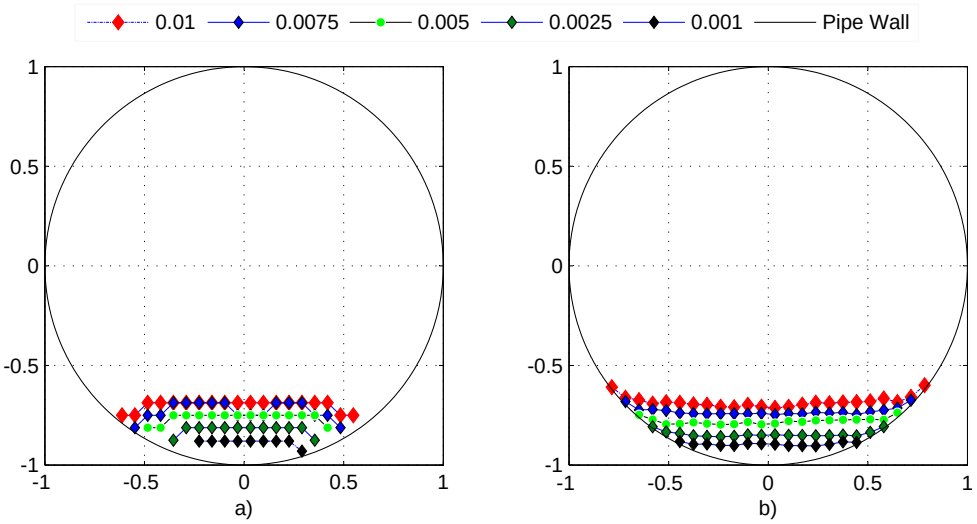

Figure 4.20: Interface level measurements with ECT (left) and vertical beam GRM (right) for air-oil flows with mixture velocity, U_{mix}, 5 m/s and different liquid fractions, α_l, when pipe inclination is -1°. Oil fractions, α_o, used are given in legend on top

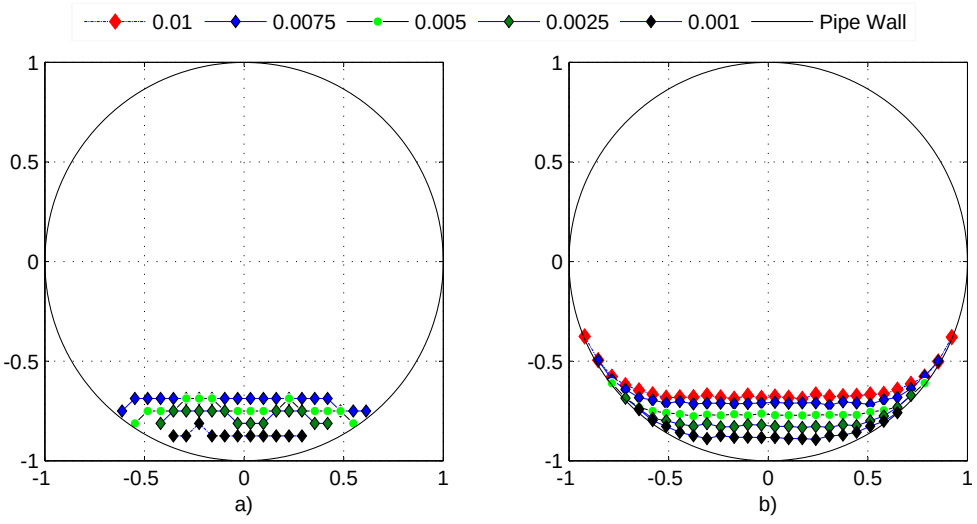

Figure 4.21: Interface level measurements with ECT (left) and vertical beam GRM (right) for air-oil flows with mixture velocity, U_{mix}, 10 m/s and different liquid fractions, α_l, when pipe inclination is -1°. Oil fractions, α_o, used are given in legend on top

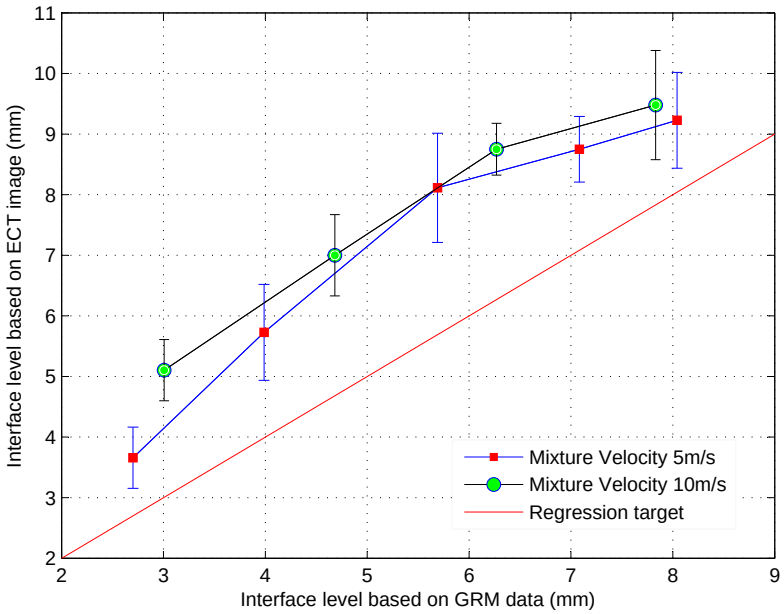

Figure 4.22: Interface levels based on ECT and GRM for -1° downward to horizontal flows with RMS uncertainties

GRM measurements can be improved to a certain level by increasing the strength of radioactive source. But according to the government health and safety regulations, it cannot be increased beyond 20mSv per year (Norwegion radiation protection authority 2005). This GRM does emit 0.2μSv per year and is well below the allowable limit.

Table 4.5: Performance comparison of ECT and GRM

Selected parameters of the ECT/GRM systems	GRM	ECT
Horizontal Resolution	3	3
Vertical Resolution	1	3
Dimention of data	1×32-1D array	32×32-2D pixel grid
Measurement speed	25min	0.01s
Measurement mode	Time average measurements	Online

ECT Results presented are averaged pixel values. So, it is useful to study how pixel values varies or disperse from the mean value. It can be done by calculating the standard deviation, STD, of each pixel over a specified time interval. The standard deviation of pixel arrays presents the fluctuations or variations over the whole pipe cross-section.

For the mixture velocity U_{mix} = 5 m/s and α_o = 0.01, standard deviation of the pixel values

of first 6000 tomograms were calculated and then plotted in a mesh as shown in Figure 4.23.

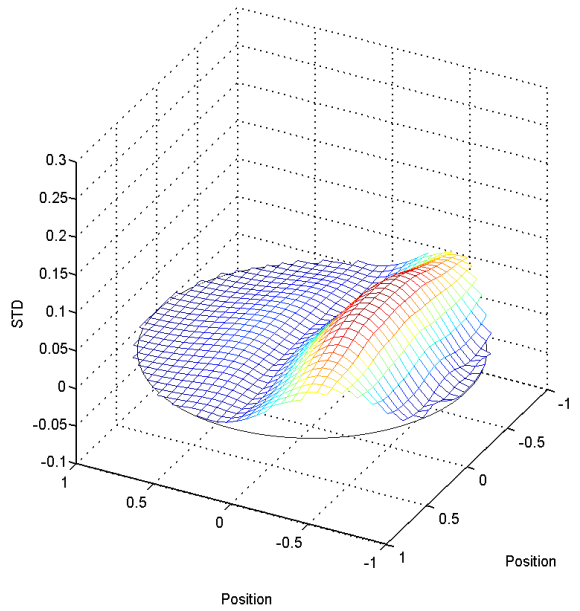

Figure 4.23: Standard deviation of pixel grid arrays at mixture velocity, U_{mix}, 5 m/s and α_o 0.01 for horizontal flow

It can be observed in Figure 4.23 that the standard deviation is higher around the interface boundary. This implies that the variation or fluctuation near the air-oil interface is higher and towards the above and below seems more stagnant (no or less changes in the flow dynamic). This is a very acceptable indication since the flow pattern is uniform and wavy stratified.

Both ECT and GRM have their own strong features to be used in measurements as given in Table 4.5. Possible fusions of these two measurements can be useful in making control decisions. Such combinations may be helpful in avoiding disadvantages involved with the separate use.

CFD flow simulation under corresponding experimental conditions has been performed by (Vestøl 2013) using the OLGA simulator, which is used for one dimensional simulation of gas, oil and water flows. Comparison of the results with -1° and 0° inclined flows with the mixture velocity U_{mix}=5 m/s are given in Figure 4.24. Results show that both measurement techniques follow the same trend as OLGA simulator. However, it gives a slightly higher interface boundary over the measurements. ECT gives about 3 mm and 4 mm offsets to the simulated results with -1° and 0° inclined flows. GRM results always lies between simulated and ECT results. Since the interface heights are very low, it is still hard to come to any conclusion with these limited information. It would be interesting to study the performances with different interface heights.

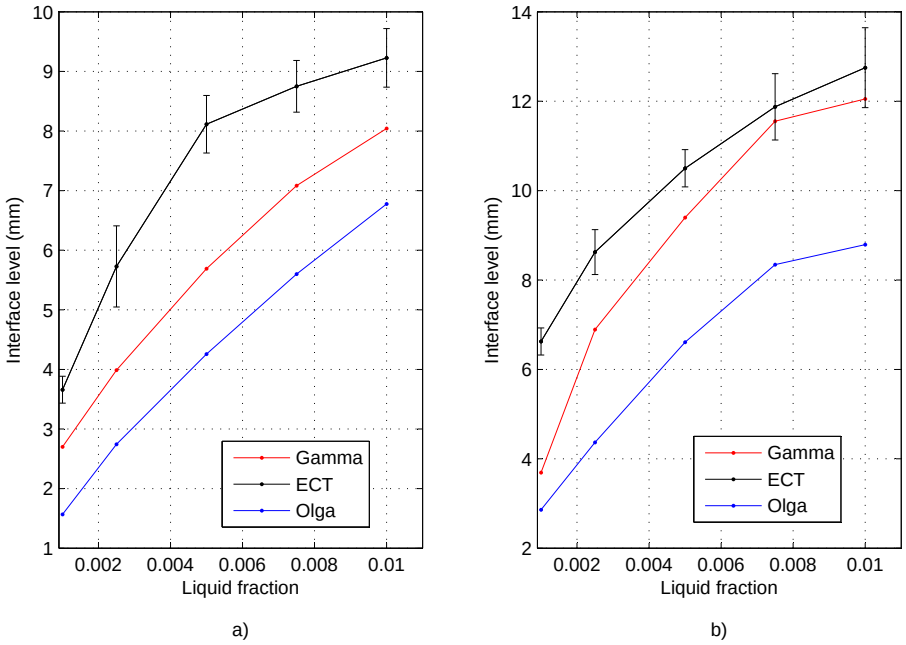

Figure 4.24: Measured and simulated interface level as a function of oil (liquid) fraction, α_o for flow of air-oil at inclinations a) -1° and b) 0°. Both figures show that interface level measurements (ECT and GRM) are getting closer when the liquid fraction, α_l, is increased

4.13 Discussion of the results

This study was mainly to see the possible estimation of interface level in horizontal pipe flows using capacitance measurements captured from ECT systems. Then, the study was extended for reduced number of electrode sensors accepting some losses in accuracy. Estimation with 6 electrode sensor produces better results compared to 5 and 4 electrode sensor results. Lower RMS error with 6 electrode sensor estimations shows that it is better among all reduced electrode sensors. With 4 electrode sensor RMS error goes almost up to 9 mm. To have a better comparison of 4, 5, 6 and 12 electrode models, architecture was unchanged. This might be the case of getting some relatively poor estimates of heights. When the two phases are air-oil, all 6, 5, and 4 selected electrode sensors can produce acceptable results with the loss of some accuracy. The higher relative permittivity of water leads to high capacitance changes making the differences between other media in the layers less discernible.

Even a few drops of water in air phase can make very significant changes in capacitance values. Hence, in the static layered flow measurements, we had to make sure that there were no water drops in the gas phase. However, this is not happening in practice and liquid droplets

would always be in the gas phase. Tomograms of air-water two phase flows do not show clear interfaces due to this reason. But, the air-oil two phase flow tomograms indicate better interface boundary. Results based on ECT measurements compared with GRM measurements (Vestøl 2013) evident that the interface heights calculated from pixel data are comparable, though they are slightly higher than the estimates based on GRM. Possibility of using a fewer number of selected electrodes to estimate interface, would be very helpful in increasing the redundancy in case of a failure of some electrodes. Separately trained ANN models have to be used in such cases.

ECT with reduced number of electrodes can be used in applications where fast estimation of interface level is important with acceptable uncertainties. When water is present in the flow, it is difficult to lower the number of electrodes below 6 without jeopardizing the performance of the system. When water is not a part of the in the pipe, even 4 electrodes sensors can be used. That would easily speed up the estimation. Accuracy of the measurements will be further improved, if 4 electrode sensor is used instead of selected 4 electrode sensor (selection of 4 electrodes from 12 electrode sensor.).

It would be very helpful to get much reliable estimations, if the ANN model is validated separately using other measurement techniques. Possibility of fusion with different techniques would further improve the estimation and the reliability. This model can be further improved to estimate air, oil, water three phase flow interfaces and hence component fractions.

Chapter 5

Slug flow studies - Detection of characteristic parameters

5.1 Introduction

Slug flow is one of the common flow patterns observable in multiphase flow applications. Gas liquid slug flow in pipelines can be explained as an alternating flow of elongated gas bubble and liquid slug shown in Figure 5.1 (Perez 2007). Slugs generated in horizontal and inclined pipes are called hydrodynamic slugs and typically, length of such a slug will be less than 500 pipe diameters (Cook & Behnia 2000). In horizontal and inclined pipe flows, increase of gas velocity, increases the amplitude of the wavy interface. Once the air velocity is sufficient to take the water to the top of the pipe by blocking the gas flow, this fast moving volume is called as a slug. As slug moves forward liquid is shed uniformly from its back and finally makes a stratified area called liquid film region. Studying the complex dynamics governs the gas liquid slug flows are very challenging. Slug flow patterns occur under a wide range of flow rates and other flow conditions like inclination angle. This further increases the complexity of the slug flow characterizations and predictions. A lot of experimental and theoretical studies have been done on slug flows for many years. Fluid flow models developed by (Dukler & Hubbard 1975) and (Ruder et al. 1989) on gas liquid flows in horizontal pipes are still being investigated and used in many research and simulation works.

Characterization of slug flows is very useful in developing correlation for the flow simulations and slug flow control applications. Possibilities of studying slug flow characteristics using existing ECT and ERT measurements are discussed in this chapter. Raw measurements from ECT and ERT are used in the analysis here instead of tomograms. Parameters calculated in these studies are slug translational velocity, slug front and tail velocities, liquid film thickness, slug frequency and liquid slug length.

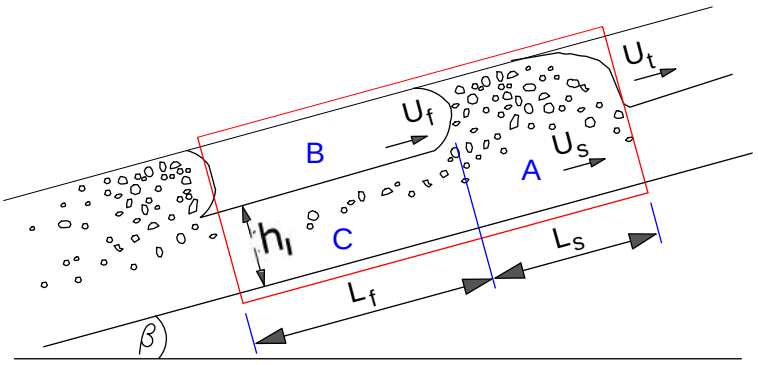

Figure 5.1: Slug unit representation with characteristic parameters, h_l- film thickness, U_s- liquid slug velocity, L_s- liquid slug length, L_f- film length, U_t- translational velocity

5.2 Slug parameter estimations using ECTm/ERTm and high-speed camera

Figure 5.1 shows a simplified physical representation of a single slug unit including the bubble. Basic slug unit consists of a slug body (A in figure) and a liquid film with their lengths given as L_s and L_f respectively in Figure 5.1. The gas pocket called as Taylor bubble (B in figure), (as defined by (Perez 2007)) and the liquid film zone underneath (C) are also shown in the same figure. Height of liquid hold up (or the film thickness) is h_l. The velocity of the whole slug unit at the front of the slug body is called as slug translational velocity U_t. When slug is moving forward, liquid (in film region) at the slug front is scooped up and moved with the slug velocity, U_s. Since the slug flow is by nature a random phenomenon, even with precisely controlled inflow conditions, these slug parameters vary with time.

By using time series of raw ECT and ERT measurements, characterization of slugs in a liquid gas two phase flows can be easily done. Possibilities of using ECT techniques in the flow parameter estimations have been discussed in details by (Ismail et al. 2005) and (Bertani et al. 2010). However, main concern in tomography technique is the construction of very accurate tomograms, which is not so critical in many flow control applications in process industries as explained in Chapter 4. ERT technique fails to construct accurate tomograms in horizontal and inclined flow measurements, unless conducting fluid component is having electrical contacts with all ERT sensor electrodes. However, with the tomometric approach, it is still possible to extract some useful flow information.

Slug characterization using time series of two capacitance probe signals and two conductance probe signals has been tested and validated in (Perez 2007) and (Al-Lababidi 2006) respectively. Pressure fluctuations associated with the slug phenomena can also be used to estimate the slug flow parameters. As explained in (Reinecke et al. 1988), pressure drop information along the slug unit can be used to study the characteristics of the flow patterns. Possibilities of usage of differential pressure signals in slug flow control have been investigated by (Havre

et al. 2000). Differential pressure between points A and B shown in Figure 3.2 is measured using pressure transducer PDT121. Typical plots of time series for the pressure signals with corresponding slug flow is given in Figure 5.2.

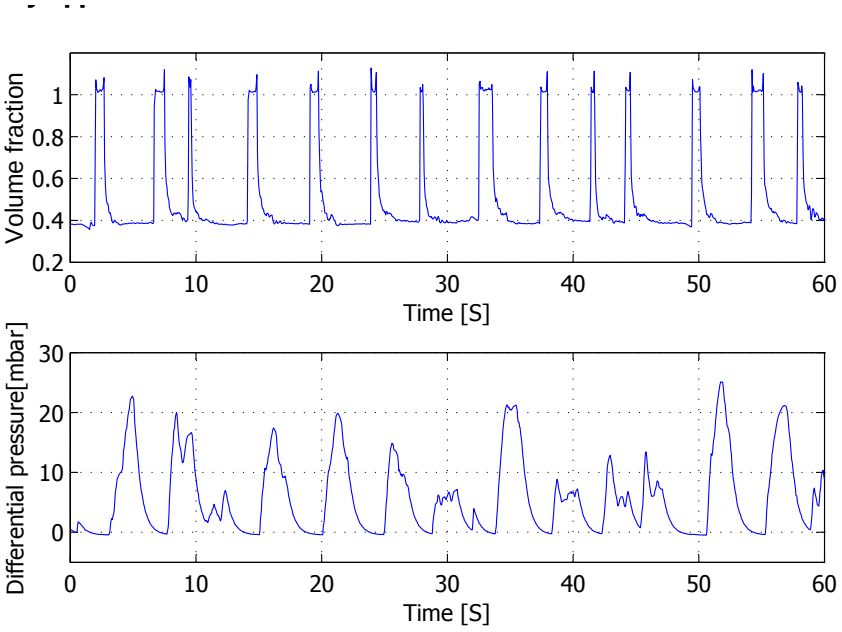

Figure 5.2: Typical time series from the differential pressure signals as registered by PDT121

5.2.1 Measurements and experiment matrix

Experiments were performed in the multiphase flow facility explained in the Chapter 3. Inclination of the test section, β, was maintained at $+1^{\circ}$ to the horizontal to generate slug flows. Inter-electrode capacitance and resistance measurements were captured separately using ECT and ERT systems with the loop running under the experimental conditions given in Table 5.1. MotionPRO X high-speed camera was also used to capture the flow phenomena. Differential pressure measurements given by PDT121 also captured while the experiments were running.

All experiments were performed maintaining inlet volumetric flow rates of water and air at the set values. Superficial air and water flow rates of each experiment along with the measurement modalities are given in the experiment matrix in Table 5.1.

5.2.2 Calculation of slug translation velocity

Cross-correlation of the time series data of liquid volume fraction from twin plane tomography sensors can be used to calculate the slug translational velocity of each experimental run. . Typical time series of two separate ECT and ERT twin plane systems are shown in Figures 5.3 and 5.4 respectively.

Table 5.1: Superficial air and water velocities of each set of experiments and the measurement techniques used for each set of experiments conducted in the current study. For some values of superficial water velocity, corresponding high speed camera images of usable quality were not available.

		Superficial water velocity (m/s)		
		0.20	0.27	0.33
Superficial air velocity (m/s)	0.28			
	0.56			
	0.83			
	1.11			
	1.39	ECT		ECT
	1.67	ERT	ECT	PDT121
	1.95	Images		Images
	2.22			
	2.50			
	2.78			

(Al-Lababidi 2006) has used the same technique with conductivity probe signals to estimate slug translational velocity. Results have been compared with ultrasonic measurements. Volume fraction data calculated by averaging in the pipe cross-sectional distribution of water and air two phases have been used to estimate the slug translational velocity by (Rogero 2009). Here, the measurements have been acquired from wire-mesh sensors. The approach explains in this thesis is also based on the cross-correlation technique, but the time series signals from twin plane tomography sensors were calculated in a similar manner explained by (Rogero 2009). Liquid volume fraction can be easily calculated using ECT measurements as given in Equation (5.1).

$$\alpha_l = \frac{2}{N_C\,(N_C-1)} \sum_{i=1}^{N_C} \left(\sum_{j=1}^{N_C} C_{i,j} \right) \qquad \forall\ i<j \tag{5.1}$$

where $N_C = 12$ and C_{ij} is capacitance measurement between electrode i and j.[1]

The same method does not work with ERT measurement of horizontal flows, since some electrode loose contact with conductive medium. Hence, the average of each voltage measurement frame is calculated as given in the Equation (5.2).

$$V_{mean} = \frac{2}{N_R\,(N_R-3)} \left(\sum_{i=1}^{N_R-1} \left(\sum_{j=i+1}^{N_R-1} (E_{i,i+1} - E_{j,j+1}) \right) + \sum_{i=2}^{N_R-2} (E_{i,i+1} - E_{N_R,1}) \right) \tag{5.2}$$

where $E_{i,i+1} - E_{j,j+1}$ denotes the voltage measurement between j^{th} and $(j+1)^{\text{th}}$ when current is applied between i^{th} and $(i+1)^{\text{th}}$ electrodes. The time delay, τ_{max}, corresponding to the maximum value of the cross-correlation function gives the transit time of the flow between the two sensors. From the calculation of the cross-correlation as given in Equation (2.27), time delay, τ_{max}, can

[1] More on this α_l calculation can be found in (PTL 2009)

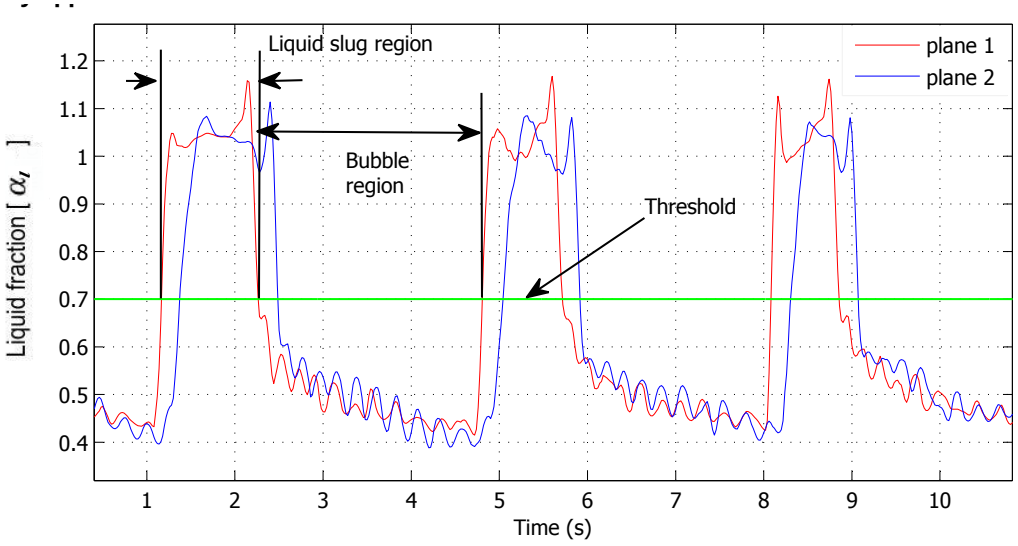

Figure 5.3: Typical slug pulse as obtained from ECT time sequences. The point where the volume fraction exceeds the threshold value is considered as the liquid slug front boundary and where it crosses to go below the threshold is selected as the tail boundary

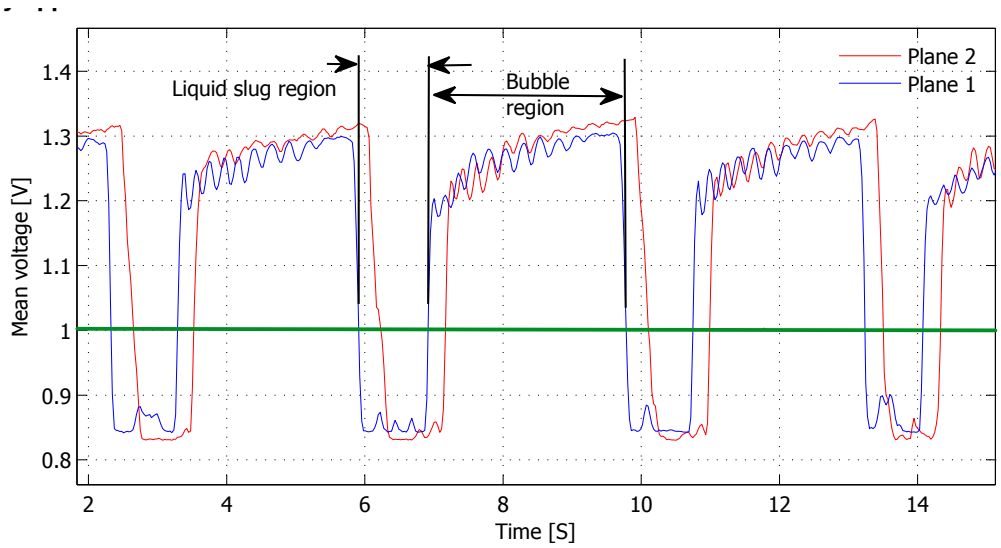

Figure 5.4: Typical slug pulse as obtained from ERT time sequences. The point where the mean voltage drops below threshold value is considered as the liquid slug front boundary and where it crosses to go over the threshold is selected as the tail boundary. Time length between slug front and tail is liquid slug region. Time length between slug tail and front is gas bubble region

be found by selecting the correlation peak. Slug velocity, U_s, can be evaluated using the time delay, τ_{max}, and distance between the two sensor planes, L_{pla}, as:

$$U_s = \frac{L_{pla}}{\tau_{max}} \tag{5.3}$$

Distance between two sensor planes is 0.19m in both ECT and ERT sensor modules. Both ECT and ERT measurements were used in the estimation of the slug velocity. Captured raw capacitance and resistance measurements were correlated separately. Flowan software developed by Process Tomography Limited was used to estimate the slug velocities for verifying the results. Flowan software uses pixel correlation for velocity estimation.

5.2.3 Slug front and tail velocity

Slug front and tail velocities, (U_s and U_f), were estimated using volume fraction signals based on ECTm. When volume fraction crosses the threshold values at slug front and tail, time stamps corresponding to these events, are selected from both sensor planes of ECT module. Then the time taken by each slug front and tail to pass the distance between two sensor planes can be calculated using correlation Equation (5.3). Slug front and tail velocities can be computed using this information.

5.2.4 Liquid film thickness

Time series volume fraction signal, α, of a typical slug flow clearly shows the slug body region (A) and bubble region (B). Then, the liquid film thickness, h_l,(under the Taylor bubble region) shown in Figure 5.1 can be easily calculated using the pipe geometry as given in Figure 5.5.

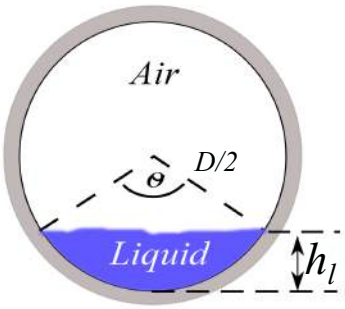

Figure 5.5: Cross-sectional geometry of liquid layer in two phase flow with arc angle θ describing the section occupied by the liquid of height h_l

5.2.5 Slug frequency estimation

The number of slugs moving past these two sets of sensors in the two different planes pl_1 and pl_2 within the observation period can be counted and used to calculate the slug frequency as given in Equation (5.4).

$$f_s = \frac{n_s}{T_{ob}} \tag{5.4}$$

where f_s is the slug frequency, n_s is the number of slugs passed during the observation period T_{ob}.

A threshold value has to be defined to decide the existence of slug (Al-Lababidi 2006). When the signal exceeds the threshold, one is added to the slug count. Figure 5.4 shows the threshold value as 1V for the signals from ERT system. It is 0.7 (70% of the volume fraction of liquid) for the ECT signals as marked on the Figure 5.3.

Average of the inter-electrode ECT/ERT measurements was used to construct signals shown in figures. This averaging process helps to identify the boundaries of the slug bodies. Images captured from the high-speed camera were also run frame by frame to count the number of slugs to verify the results.

5.2.6 Slug lengths

Length of the liquid slug body (A in Figure 5.1) is marked as L_s. Time window, t_s, associated with the slug body as indicated in the Figure 5.3 is first calculated. Here, the same t_s, defined based on the threshold values in the slug frequency calculation, is applied to locate the time window of the slug body.

Then, with the corresponding estimated slug flow velocities, each slug length, L_s, is calculated as follows.

$$L_s = t_s U_s \tag{5.5}$$

Images of a typical slug front and tail captured by high-speed camera are also shown in Figure 5.6.

5.3 Results from slug flow studies

Estimates of slug translational velocity, slug front and tail velocity, slug frequency and slug length are given here. Results based on high-speed camera images, differential pressure data and the 'Flowan' software are also presented.

Careful examinations on time series measurements indicates the complex nature involved with the slug flows. Especially in the slug frequency and length estimations, sudden waves, which cross the thresholds might be considered as slugs. Such observations correspond to the superficial gas and water velocities 0.28 m/s and 0.2 m/s are briefly discussed here. Time series signals calculated based on ERT measurements are given in Figure 5.7. Liquid slug lengths, L_s, calculated using ERT measurements of sensor plane 1, as explained above, are shown in Figure

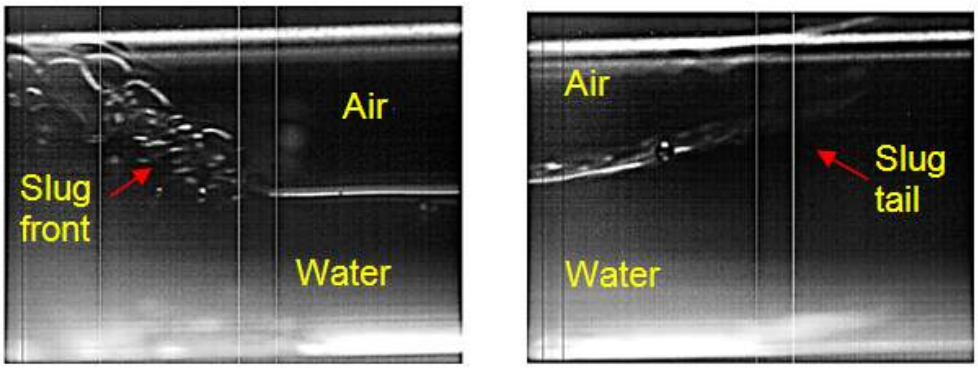

Figure 5.6: Images of slug front and tail based on high-speed high resolution photographs captured from Motion PRO X camera at 50 fps speed

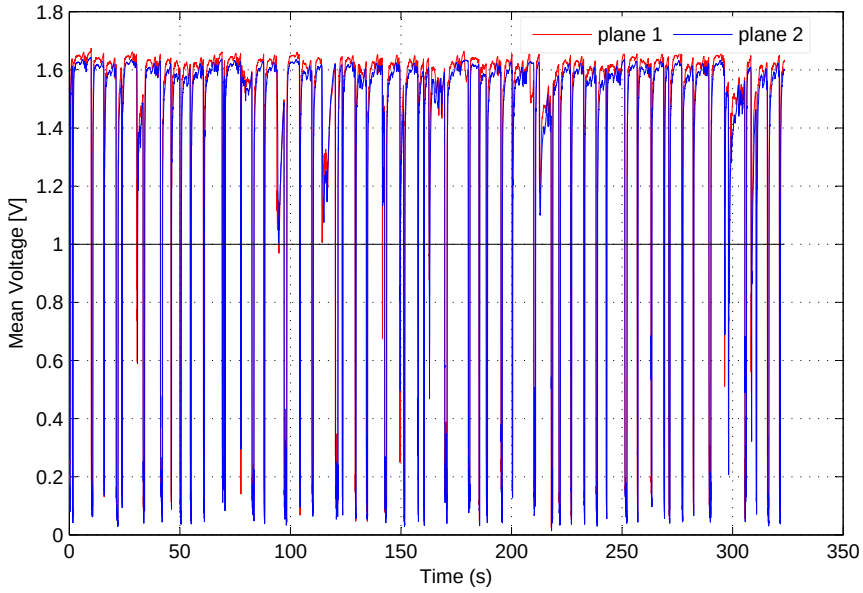

Figure 5.7: Time series of mean voltage captured from ERT under U_{LS} 2 m/s and U_{GS} 0.28 m/s

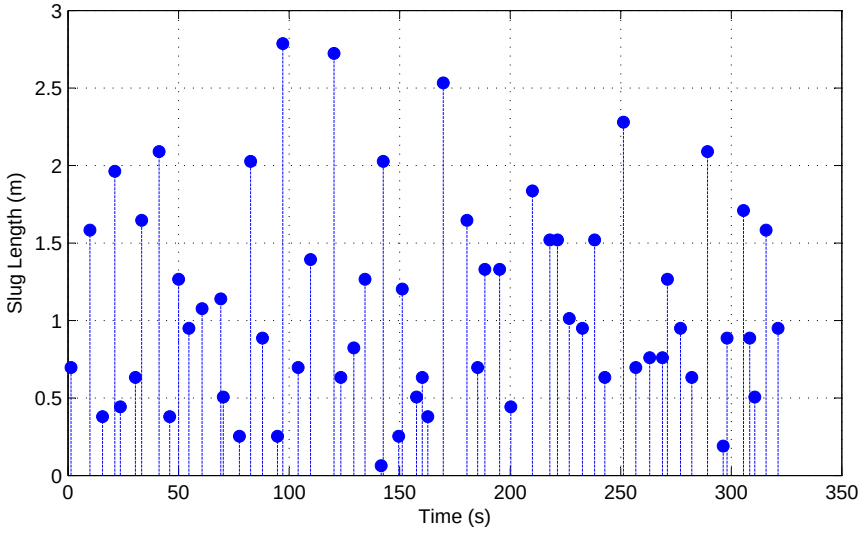

Figure 5.8: Liquid slug lengths calculated from the ERT measurements shown in Figure 5.7

5.8. This figure can be used to get clarifications in doubts involved in deciding the variations in the signal due to slug or a wave. A small slug length, about 0.1m, shown at around 140s time stamp in the Figure 5.8 looks doubtful. Then, time series signals (shown in Figure 5.7) were zoomed and observed at around 140s as shown in Figure 5.9. It can be seen that the signal from plane 1 crosses the threshold limit, but the signal from plane 2 does not. Hence, it can't be considered as a slug, it looks merely a rolling-wave. The next smallest slug appeared at around 296 s and it's length was 0.19m. This can be considered as a short slug, since it has been observed in both sensor planes as shown in the Figure 5.10.

5.3.1 Slug translation velocity

Slug translation velocity calculated based on the ECT and ERT measurements are presented in Figure 5.11. Variations in slug translation velocities against the increase in superficial gas velocities are discussed here.

It can be seen in Figure 5.11, that all three curves show an increase in slug velocities with increasing superficial gas velocities. ERT measurements show an increase of slug velocity about 0.1 m/s at 0.8 m/s superficial gas velocity and decrease of about 0.13 m/s at superficial gas velocity 1.1 m/s compared to the ECT and 'Flowan' based calculations. Highest velocity difference 0.35 m/s (between ECT and ERT) is observed at the superficial air velocity 2.2 m/s as shown in the figure.

To determine whether these estimation differences are due to different data capturing rates of ECT and ERT systems, sensitivities of the slug velocities to the data capturing rates were tested. Since, the data capturing rate is 100 fps in ECT system, uncertainty involved with the time delay,

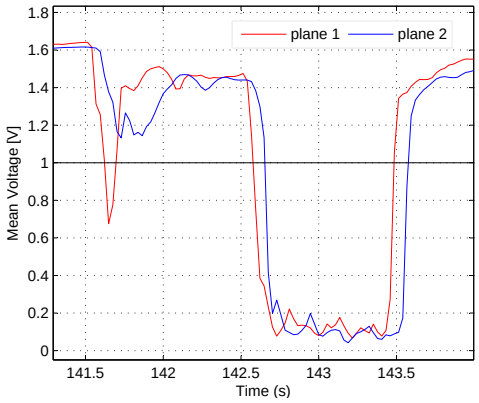

Figure 5.9: Typical wave captured with ERT system

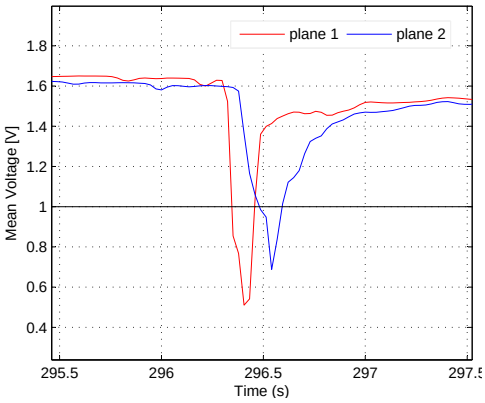

Figure 5.10: Typical small slug observed with ERT system

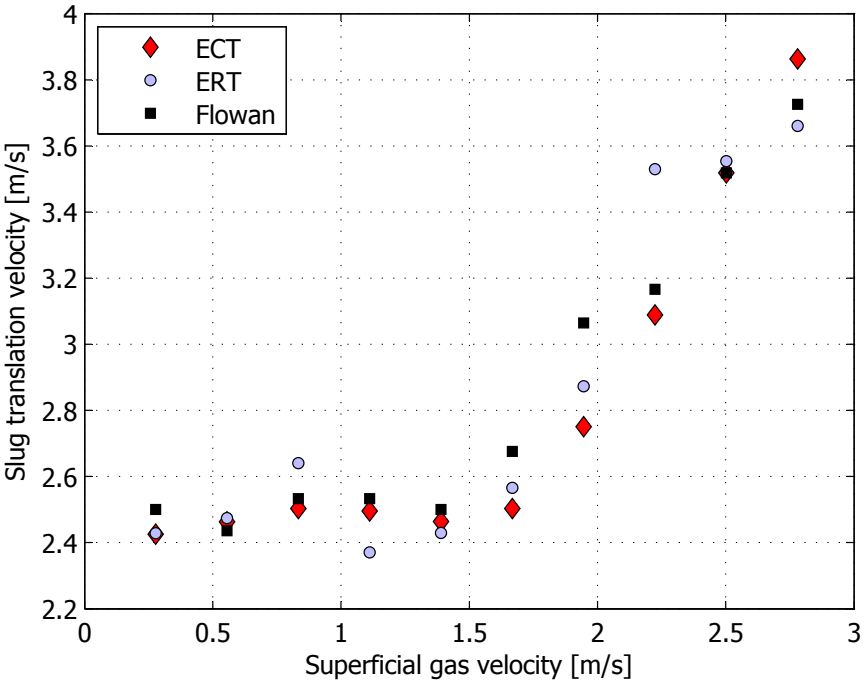

Figure 5.11: Slug velocity with water superficial velocity at 0.2 m/s

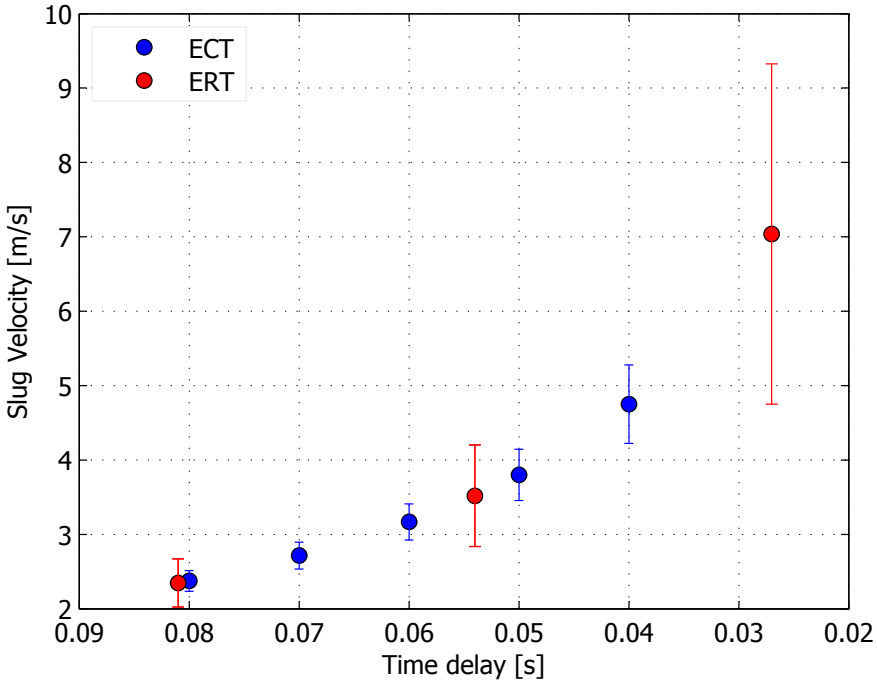

Figure 5.12: Estimated uncertainties for different slug velocities. Time delays calculated here are always a fraction of the data capturing rate. Hence, calculations may miss the values lying in between. This error uncertainty increases when capturing rate decreases and the slug velocities increase. Error bars given in figure show the range. ECT is showing relatively small errors compared to ERT. This is due to the high capturing rate of ECT.

τ_{max}, becomes ± 0.005 s. The corresponding uncertainty associated with ERT is ± 0.013 s.

When τ_{max} is increased, slug flow velocity is decreased and hence uncertainties of the calculated slug velocities are also decreased. When the time delay, τ_{max}, is decreased, both slug velocity and uncertainty are increased. Figure 5.12 presents the uncertainty increase in the velocity range considered of this work. This may be one of the reasons for higher velocity estimates resulting from ERT data.

5.3.2 Slug front and tail velocity

Slug front and tail velocities (U_s and U_f) calculated from the experimental data captured under the superficial air velocity 0.28 m/s and water velocity 0.2 m/s for each slug are given in Figure 5.13. It can be clearly seen that these velocities vary from slug to slug. However, slug front velocity is always slightly higher than the corresponding tail velocity. The mean slug front and tail velocities from each experiment are calculated and plotted along with the translational velocity as shown in Figure 5.14. When the superficial air velocity is increased, slug front and tail velocities are also increased. The velocity difference between slug front and tail also seems to be increasing.

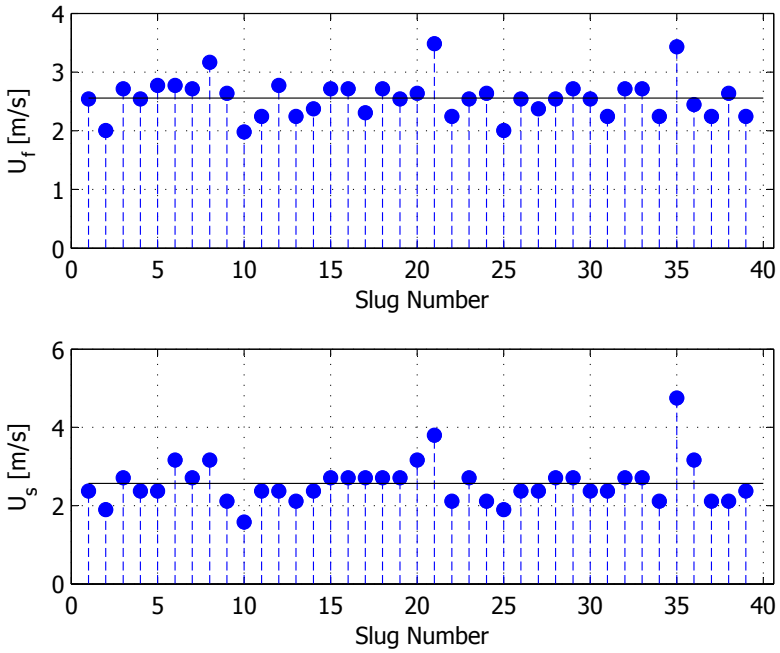

Figure 5.13: Calculated slug front and tail velocities Under U_{GS}=0.28 m/s and U_{LS}= 0.2 m/s

5.3.3 Liquid film thickness

As given in Figure 5.15, liquid film thickness is not varying much with the increases superficial velocities. Film thickness calculated using high-speed camera images are a bit lower than the ECT based calculations. Most of the time, presence of air bubbles and uneven nature of the interface made it difficult to measure the interface level from captured images. The ECT based calculation is affected by the wetted inner pipe wall, it may give higher water volume fractions and the h_l calculated from water volume fraction also affected. This might be the cause for getting slightly increased h_l shown in Figure 5.15.

5.3.4 Slug frequency

Slug frequency decreases when the superficial gas velocity increases as explained in (Kang et al. 1999). The results given in Figure 5.16, show a slight decrease in slug frequency. It can be easily understood that results based on the image data are showing higher slug frequencies compared to the ECT and ERT based calculations even though they follow similar trends. An offset of about +0.05 Hz, compared to the other ECT/ERT based calculations is observed. Limitations in the memory storage in the camera restrict the possibilities of data capturing time period to 40s. The addition of one slug increases the slug frequency (image based calculation) by 0.025 Hz due to the limited observation time period. The ECT and ERT measurements were made for

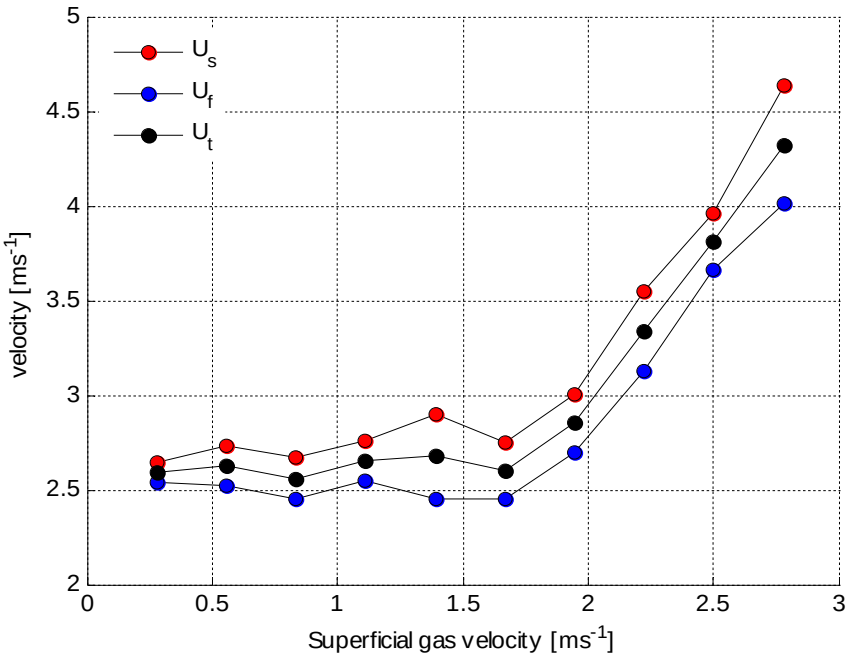

Figure 5.14: Calculated slug front and tail velocities with U_{LS}= 0.2 m/s

4 min and hence the calculations were more reasonable. The maximum difference in frequency calculations between ECT and ERT is about 0.01 Hz at the superficial air velocity of 1.1 m/s.

The differential pressure measurements cannot be used for validation of the slug frequencies, if the above mentioned method is employed. This is due to the peaks of the pressure signals does not indicate similar magnitude even though the pattern is similar. However, the slug frequency can be determined using PSD (Power Spectral Density) analysis of differential pressure signals. Here, the frequency corresponds to the maximum power is picked as the slug frequency.

Another set of experiments was performed by changing the water superficial velocity to 0.33 m/s. Results based on the ECT measurements and the frequencies calculated with differential pressure based estimates are given in Figure 5.17. PSD of the differential pressure signals at given experimental conditions are shown with power spectrums in Figure 5.18. Both calculations show that the slug frequency is increased with the increase of superficial gas velocities.

5.3.5 Slug lengths

Each individual liquid slug length calculation was made using Equation (5.5) as explained earlier. Slug velocities plotted in Figure 5.11 are used in the liquid slug length calculation.

Slug lengths calculated using ECT measurements at superficial water velocities 0.2 m/s and

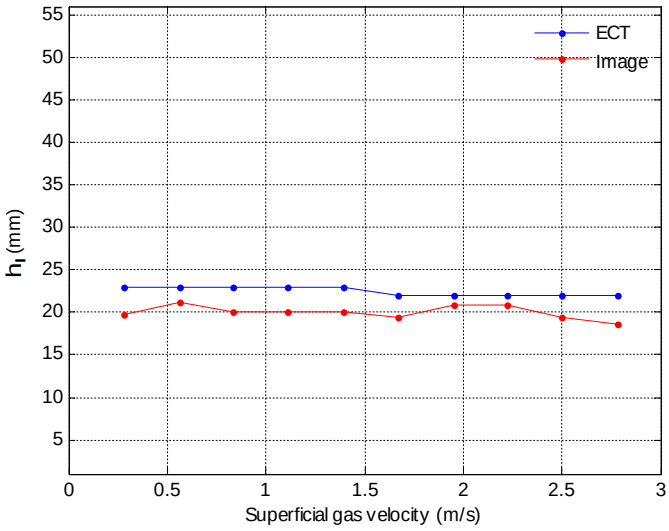

Figure 5.15: Liquid film thickness calculated with water superficial velocity 0.33 m/s

0.28 m/s with different gas velocities are given in the Figures 5.19 and 5.20. It can be clearly seen in both figures that the slug lengths of each experiment vary randomly. The longest from these experiments is 4m and the shortest is less than 0.5m. The Figure 5.21 illustrates how the mean slug length (calculated using ECT measurements) with uncertainties varies, when gas velocity increases. Uncertainty range is approximately ± 0.2 m and is more similar for all experimental points. Lower gas velocities may generate shorter liquid slugs, but higher gas velocities tend to produce longer slugs as explained in (Cai et al. 1999). Figure 5.22 shows the slug length estimations with ECT, ERT and image based measurements. All 3 curves show decrease in slug lengths with an increase in superficial water velocities. At superficial gas velocity 2.2 m/s, image data based calculation gives 1.7 m for the mean slug length. Difficulties involved in estimating exact time window of the slug are one of the reasons for the variations in image based approach. The slug translational velocity used in the slug length calculation was based on the ERT signals. This might also be a reason for getting some higher and lower slug length values. To see whether the trend observed exists with different flow conditions, another two sets of experiments were performed varying superficial water velocities to 0.27 m/s and 0.33 m/s separately. Results after the ECT measurement based calculations are presented in Figure 5.23. It can be seen clearly in Figure 5.23 that the mean liquid slug length decreases with increase in superficial gas velocity.

5.3.6 Variations in velocities in cross-sectional area

Cross-correlations between corresponding measurement signals from both planes were performed to see the possible dynamic across the pipe cross-section. Observations with ERT measurements are given in the Figure 5.24. Velocity range given by the correlations varies between 0

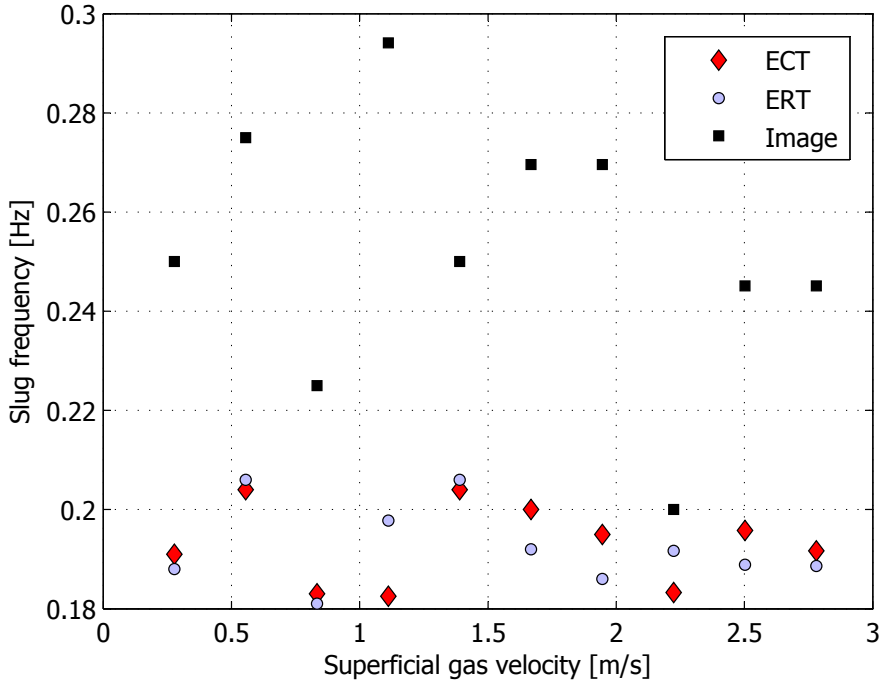

Figure 5.16: Slug frequencies with water superficial velocity at 0.2 m/s based on ECT, ERT raw data and pixel based analysis from different frames of images.

m/s and 7 m/s. Figure 5.24 shows that measurements from electrode combinations $E_{1,2}-E_{3,4}$[2], $E_{1,2}-E_{10,11}$, $E_{1,2}-E_{1,16}$, $E_{2,3}-E_{5,6}$, $E_{2,3}-E_{1,16}$, $E_{4,5}-E_{14,15}$ and $E_{5,6}-E_{14,15}$ give velocity as 7 m/s. The combinations $E_{2,3}-E_{6,7}$, $E_{3,4}-E_{7,8}$ and $E_{4,5}-E_{7,8}$ covering the pipe bottom give an estimated velocity of 2.3 m/s. Since all signal combinations are not having information related to the pipe flow fluctuations, contribution to the average velocity estimation varies. Those cover a larger sensing area of the pipe cross-section; especially the interface may contain better information related to the real velocities and variations. Low measurement frequency has limited the possible velocity variations to three values discussed earlier.

The resolution of the correlation can be improved by interpolating the values near the correlation peak. Then the peak is found by a fitting a quadratic function of the three values surrounding the peak (Long 2006). Correlation results with ECT measurements given in Figures 5.25, 5.26 and 5.27 are with these improved resolutions.

Figure 5.25 shows the cross-correlation of capacitance measurement $C_{1,8}$, $C_{1,9}$, $C_{1,10}$, $C_{1,11}$, $C_{7,9}$, $C_{7,10}$, $C_{7,11}$ and $C_{8,12}$ at both planes, shows estimated velocities over 4 m/s. Those will be over 3 m/s, for the experimental results presented in Figure 5.26 under given conditions. Measurement combinations across the cross-section can be seen in each inset of corresponding figures. Those combinations correspond to the measurements from the top part of the pipe and indicate in blue lines. During the most of the time in slug flows, this top part contains

[2] $E_{1,2}-E_{3,4}$ - Current is applied through electrode 1 and 2 and voltage between electrode 3 and 4 is measured

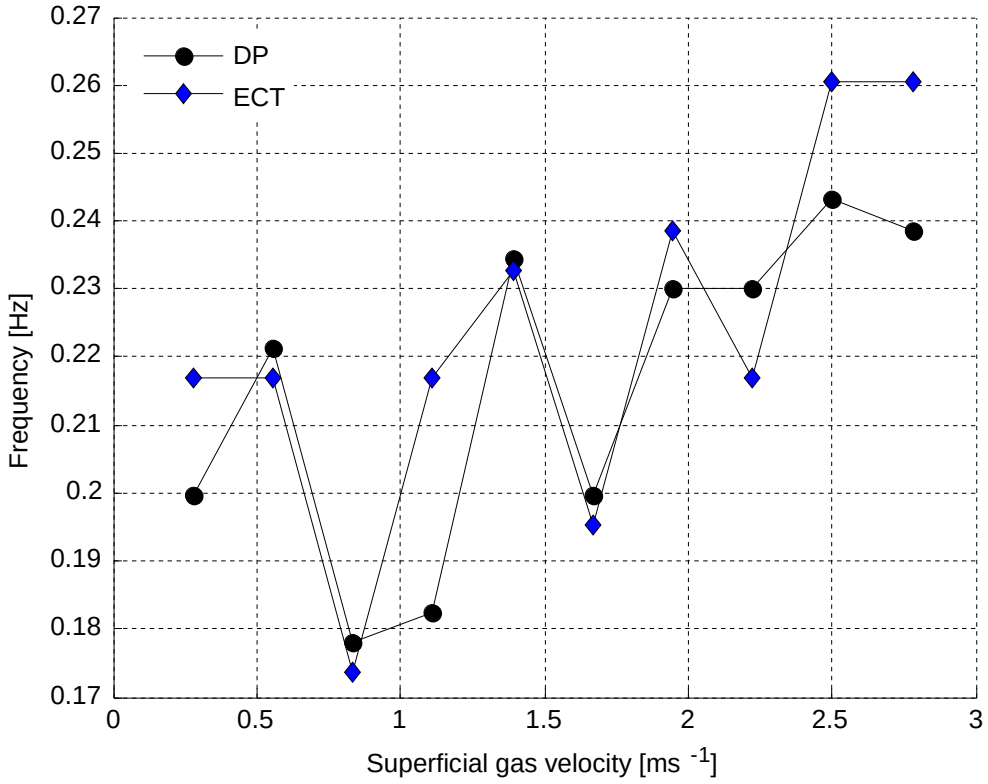

Figure 5.17: Slug frequencies with water superficial velocity at 0.2 m/s based on differential pressure and ECT measurements.

air. Measurement near pipe walls where liquid is always occupying gives lowest velocities. Combinations correspond are $C_{1,2}$, $C_{1,12}$, $C_{2,3}$, $C_{3,4}$, $C_{4,5}$, $C_{5,6}$, $C_{6,7}$ and $C_{7,8}$ and given in red lines. Less dynamic in liquids near bottom of the pipe wall would be the reason for having such lower values. Even within the Taylor bubble region, these areas contain liquid. ECT results show much variation compared to the ERT.

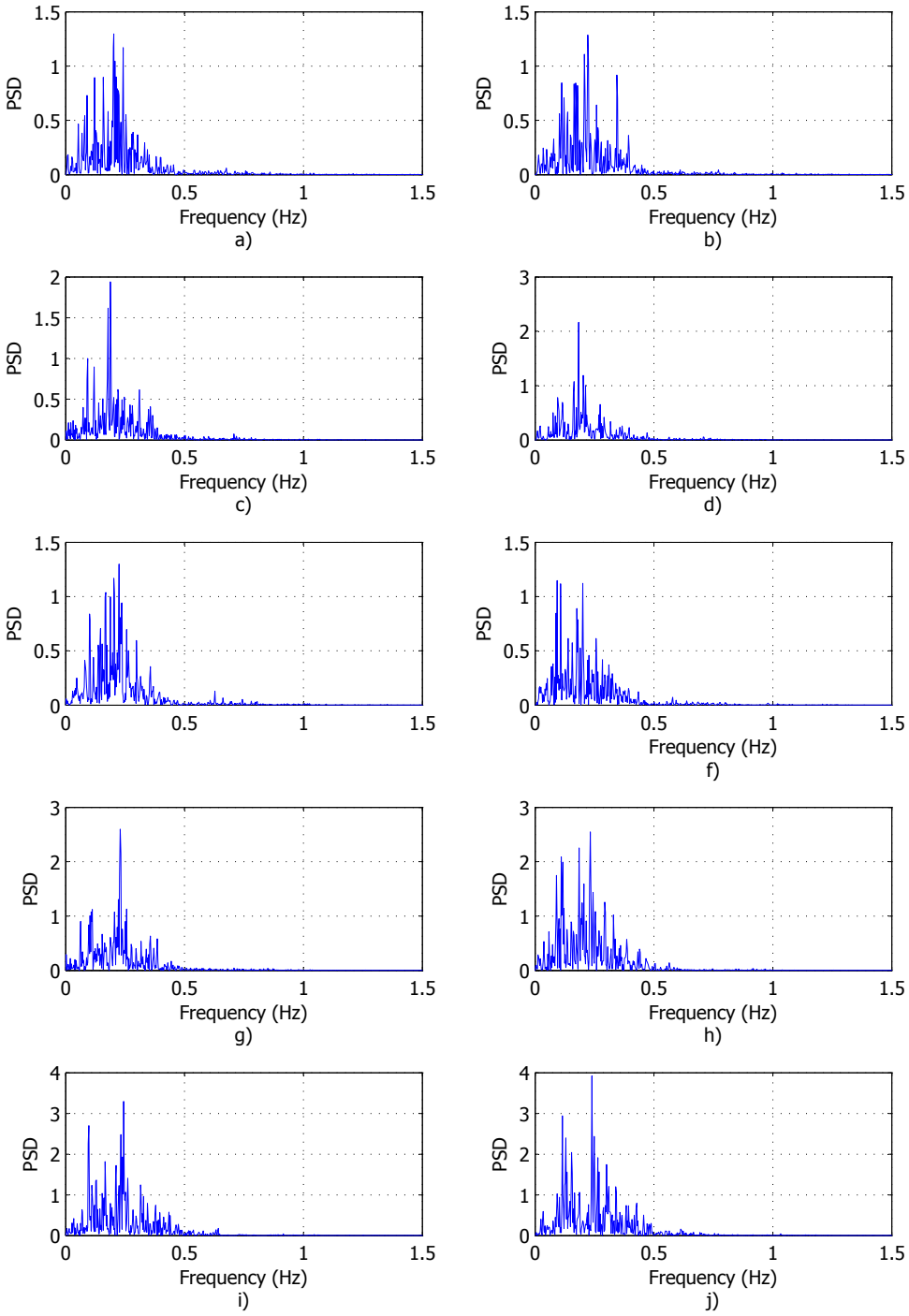

Figure 5.18: PSD of the differential pressure signal at superficial water velocity 0.33 m/s and air velocities a) 0.28 m/s b) 0.56 m/s c) 0.83 m/s d) 1.11 m/s e) 1.39 m/s f) 1.67 m/s g) 1.95 m/s h) 2.22 m/s i) 2.5 m/s j) 2.78 m/s. Dominant frequency (peak) of spectrum is selected as the slug frequency of the given flow

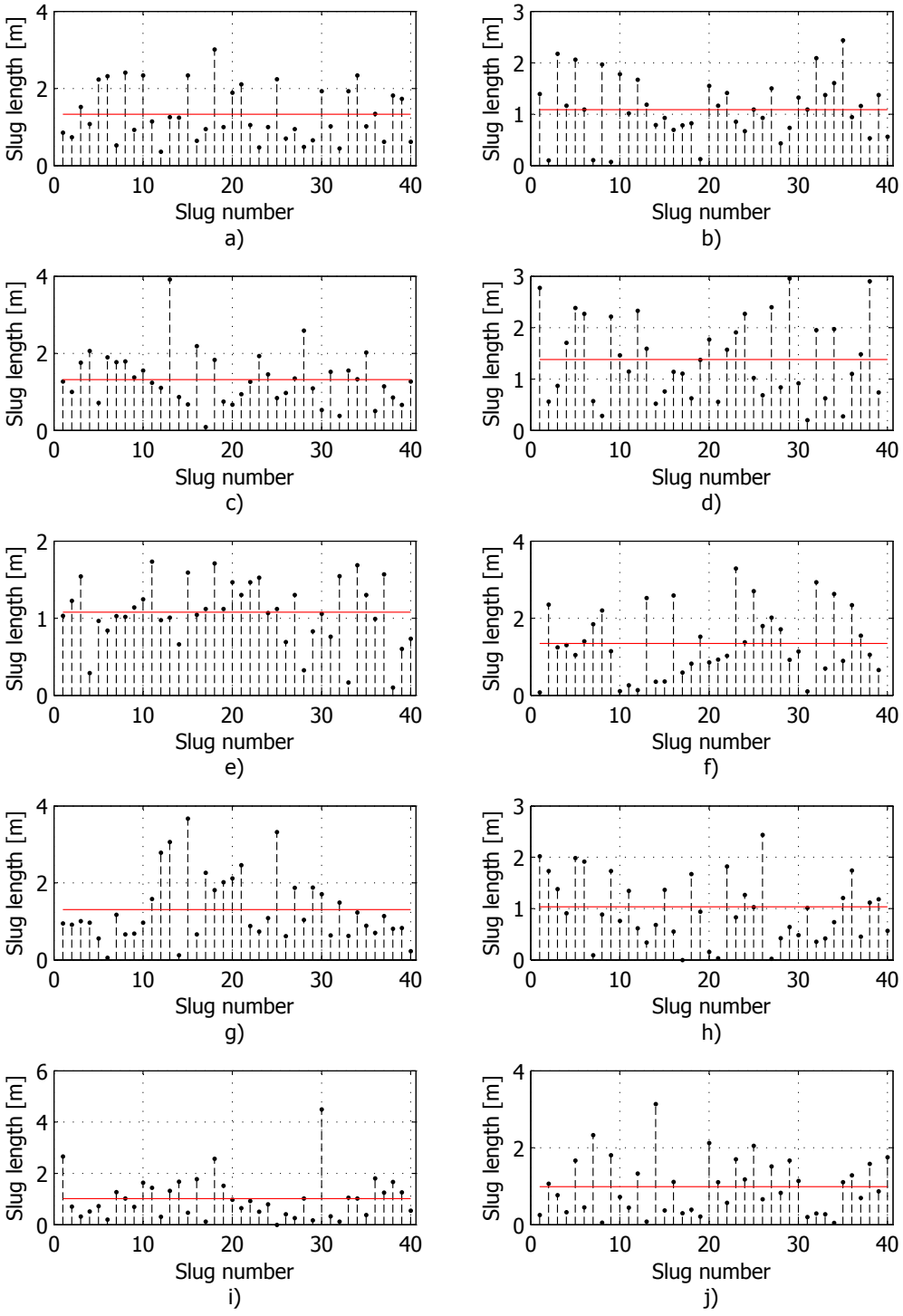

Figure 5.19: Slug lengths calculated from ECT signals at superficial water velocity 0.2 m/s and air velocities a) 0.28 m/s b) 0.56 m/s c) 0.83 m/s d) 1.11 m/s e) 1.39 m/s f) 1.67 m/s g) 1.95 m/s h) 2.22 m/s i) 2.5 m/s j) 2.78 m/s

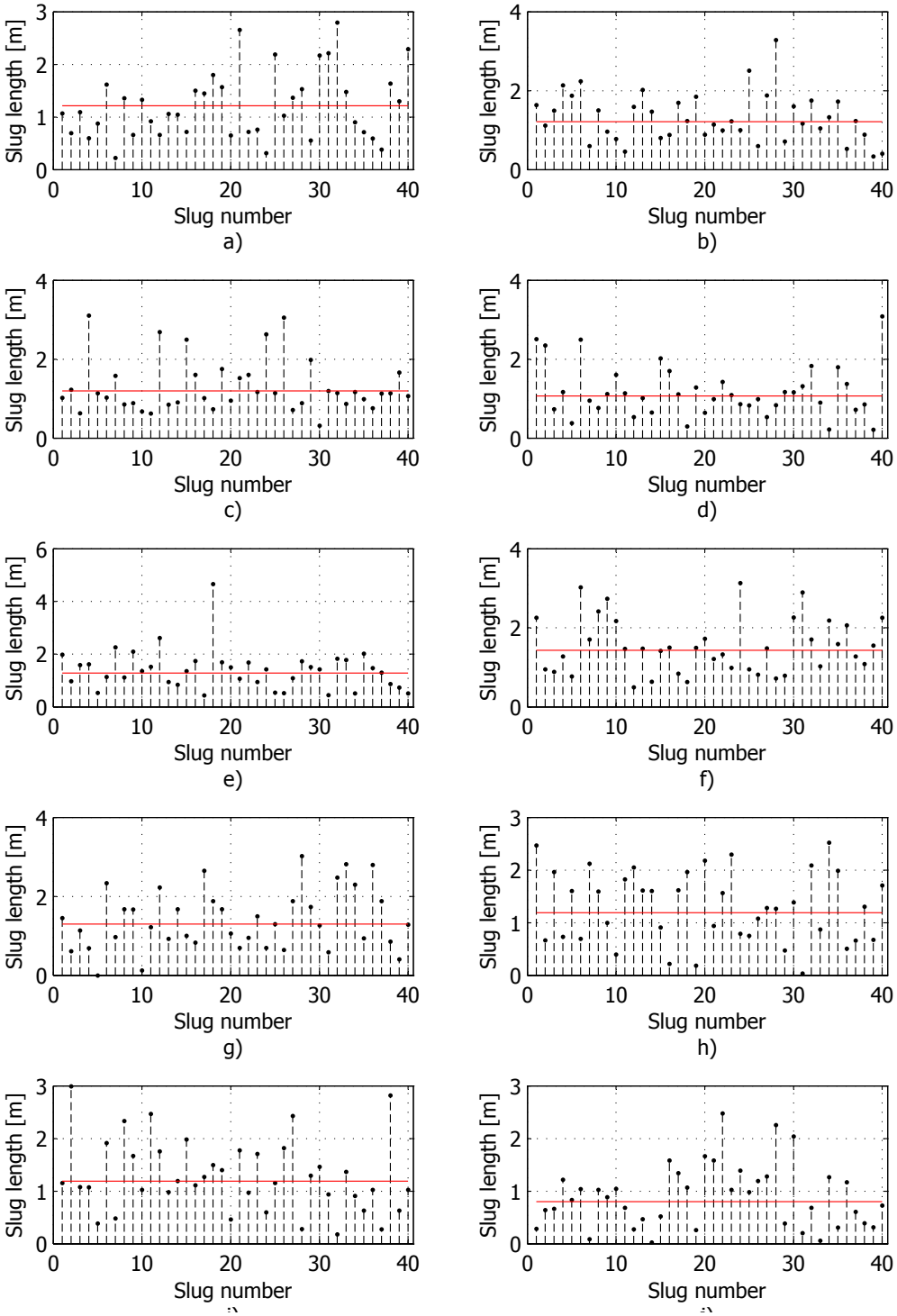

Figure 5.20: Slug lengths calculated from ECT signals at superficial water velocity 0.28 m/s and air velocities a) 0.28 m/s b) 0.56 m/s c) 0.83 m/s d) 1.11 m/s e) 1.39 m/s f) 1.67 m/s g) 1.95 m/s h) 2.22 m/s i) 2.5 m/s j) 2.78 m/s

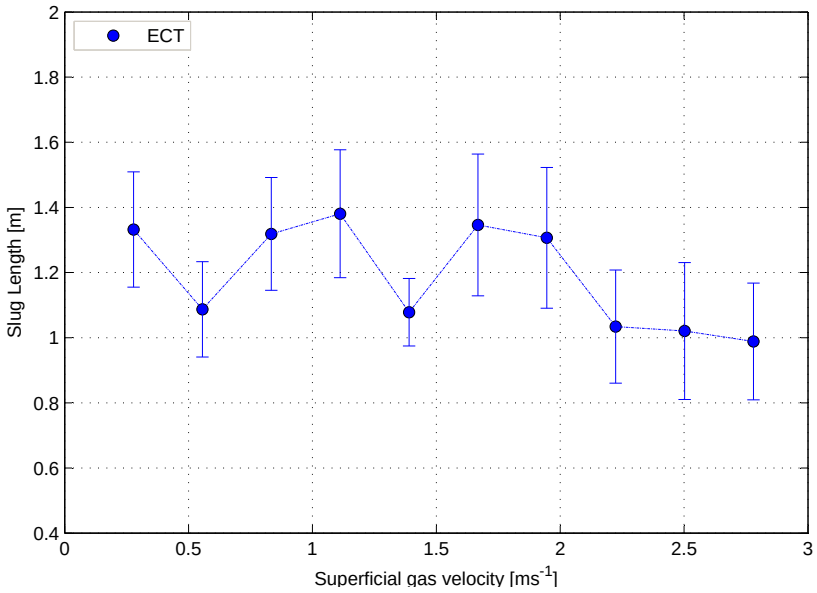

Figure 5.21: Mean slug length calculated from ECT measurements for U_{LS}=0.2 m/s and given U_{GS} with STD

5.4 Discussions of slug parameter estimation results

The estimation results show that tomometric approach on slug flow parameter estimation is possible. Data acquisition frequency is very important mainly for better slug velocity estimations. However, the number of data points are not so large, verification with other techniques evident that estimation results are satisfactory. Study of the dynamic based on the measurements across the sensor cross-section using cross-correlation also gives promising results, though they cannot be used to determine the liquid film thickness.

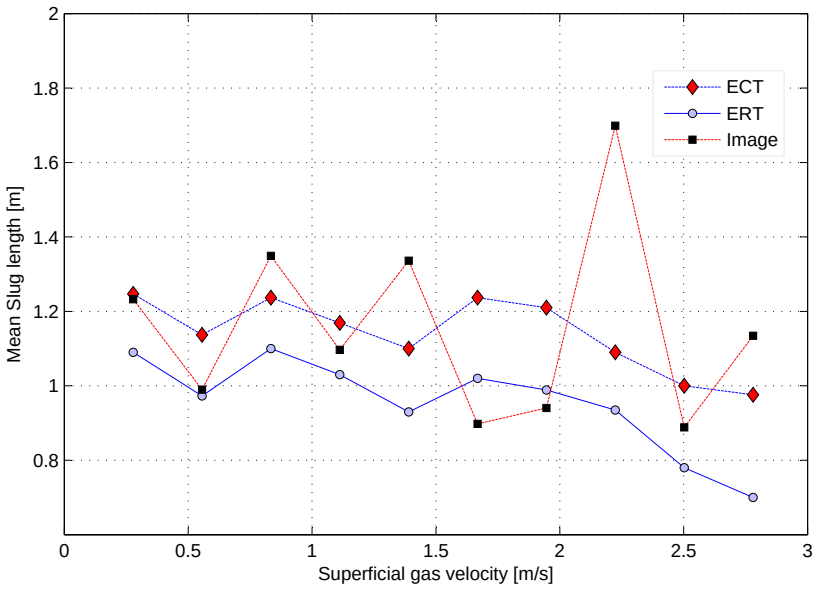

Figure 5.22: Mean slug length estimations with ECT, ERT and image data for U_{LS}=0.2 m/s and given U_{GS}

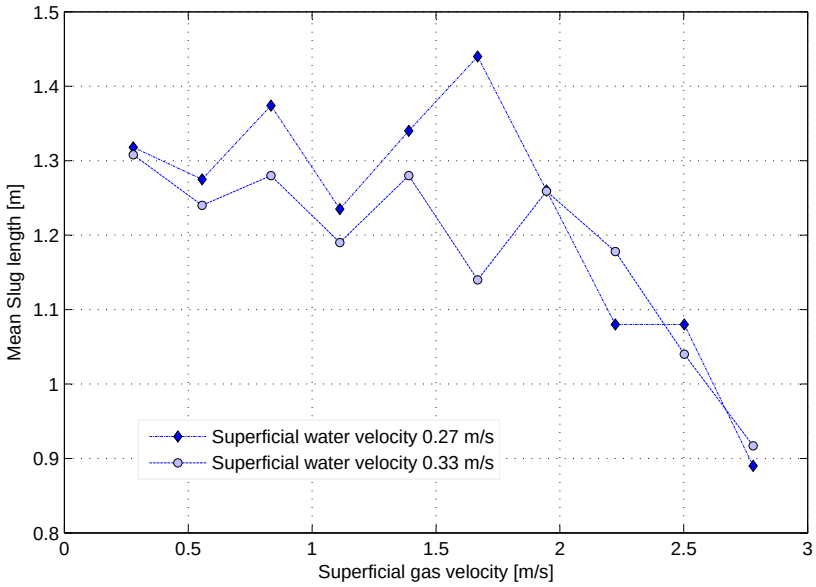

Figure 5.23: Mean slug length calculated with ECT measurements for U_{LS}=0.27 m/s and U_{LS}=0.33 m/s for given U_{GS}s

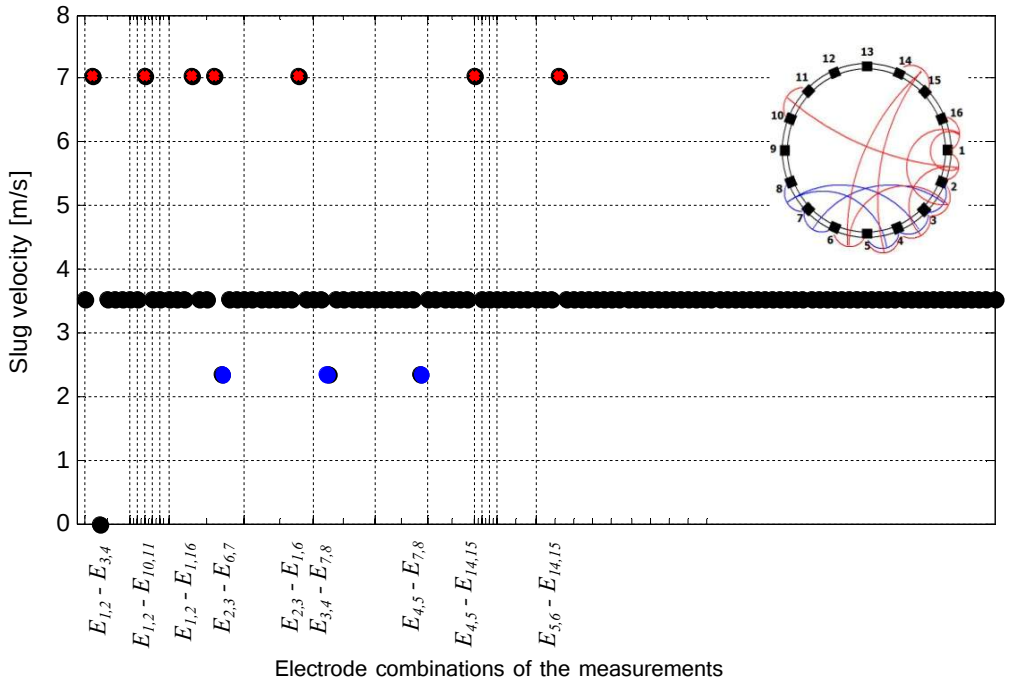

Figure 5.24: Slug velocities with cross-correlation of individual ERT measurements at superficial gas and water velocities 2.78 m/s and 0.2 m/s

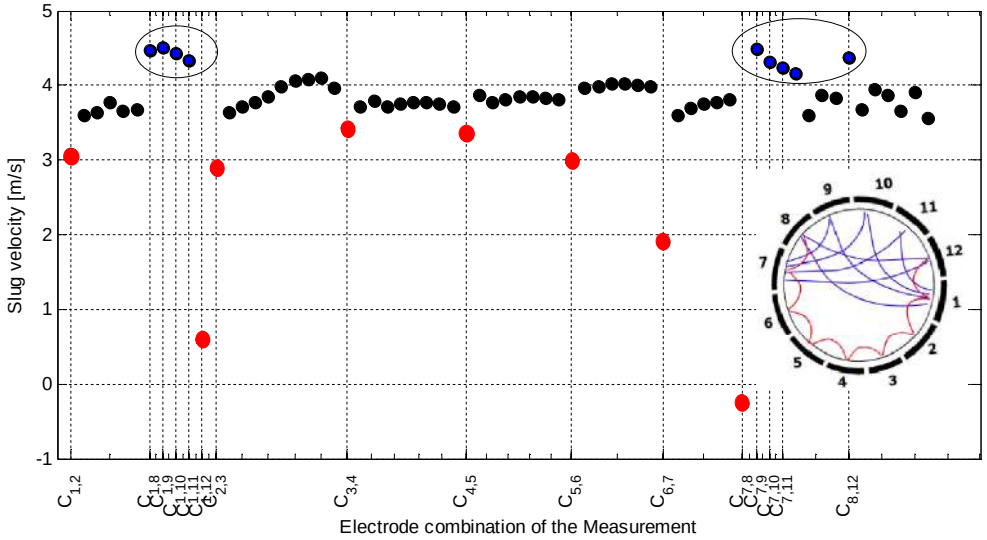

Figure 5.25: Slug velocities with cross-correlation of ECT measurements at superficial gas and water velocities 2.78 m/s and 0.2 m/s. The capacitance values indicated on the axis refer to the respective electrode combinations on plane 1 and plane 2.

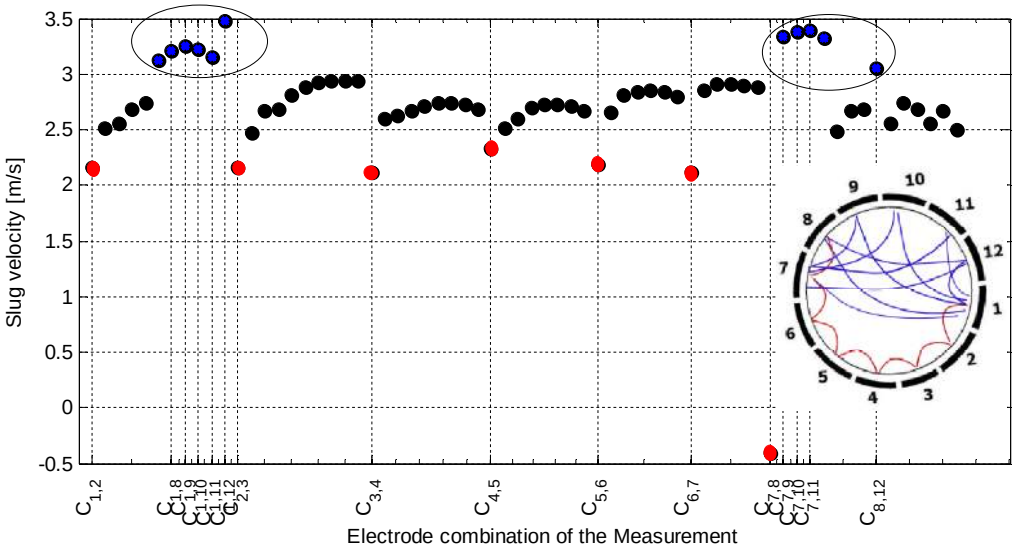

Figure 5.26: Slug velocities with cross-correlation of ECT measurements at superficial gas and water velocities 1.95 m/s and 0.2 m/s. The capacitance values indicated on the axis refer to the respective electrode combinations on plane 1 and plane 2.

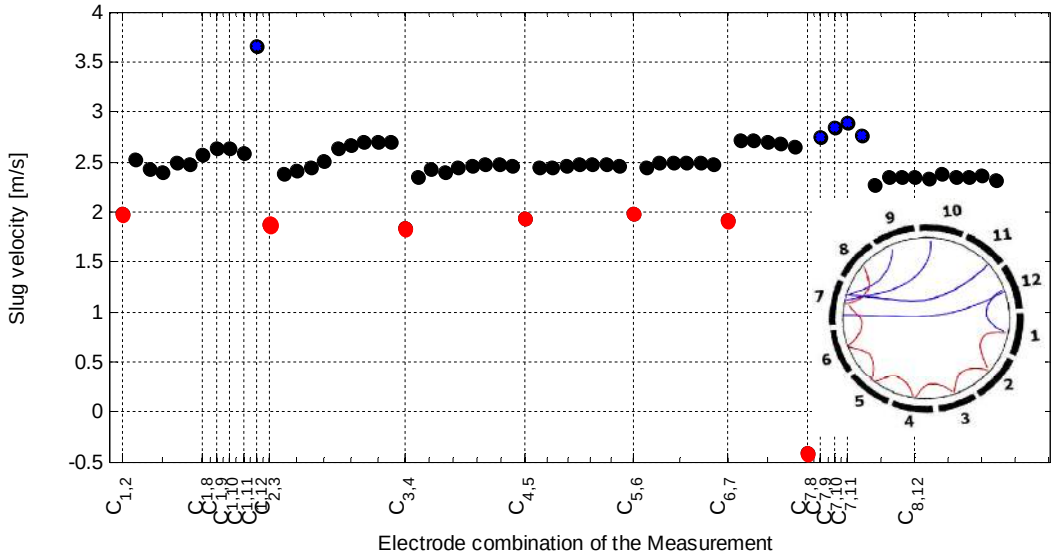

Figure 5.27: Slug velocities with cross-correlation of ECT measurements at superficial gas and water velocities 0.83 m/s and 0.2 m/s. The capacitance values indicated on the axis refer to the respective electrode combinations on plane 1 and plane 2.

Chapter 6

Flow regime identification for multiphase flow control

Use of the properties of capacitance data matrix from electrical capacitance tomography in flow regime identification and some flow parameter estimations is discussed in this chapter. Detection of reverse flow in pipes with ECTm is also discussed separately.

6.1 Properties of the capacitance matrix

Characteristic in the eigenvalue distribution of normalised capacitance matrices for three basic flow patterns have been analysed and compared by (Fang & Cumberbatch 2005).

Core flow, annular flow and stratified flow are the flow patterns investigated with numerical simulations and theoretical analysis. Possibilities of identifying flow regimes mainly annular flow, stratified flow and slug flows in horizontal pipes are investigated following the approach given by (Fang & Cumberbatch 2005) with experimental data. Here, the analyses were first done for static flow patterns and then extended to dynamic flow measurements.

As explained in the Chapter 2, typical single measurement frame captured using an ECT system contains only independent inter-electrode measurements. This is mainly to reduce the time involved with the measurement sequence. Measurements in such a typical data frame captured using 12 electrodes sensor can be arranged in an upper triangular matrix as explained in the matrix given in Equation (6.1).

$$\mathbf{C_m} = \begin{pmatrix} C_{1,2} & C_{1,3} & C_{1,4} & \cdots & C_{1,N_C} \\ 0 & C_{2,3} & C_{2,4} & \cdots & C_{2,N_C} \\ 0 & 0 & C_{3,4} & \cdots & C_{3,N_C} \\ \vdots & \vdots & \vdots & \ddots & \vdots \\ 0 & 0 & 0 & \cdots & C_{N_C-1,N_C} \end{pmatrix} = \begin{cases} a_{i,j} = C_{i.j+1} & for\ i \leqslant j \\ 0 & for\ i > j \end{cases} \tag{6.1}$$

where N_C Number of electrode in the sensor. $i = 1,2,3,...N_C$ and $j = 1,2,3,...(N_C - 1)$.

To make the complete measurement matrix, which fills all combinations of inter-electrode measurements, lower triangle elements are filled with relevant available measurements. Then

the constructed measurement data matrix would be as given in Equation (6.2).

$$\mathbf{C}_{\tilde{\mathbf{m}}} = \begin{cases} a_{i,j} = C_{i.j+1} & for\, i \leqslant j \\ a_{i,j} = C_{i+1,j} & for\, i > j \end{cases} \tag{6.2}$$

Properties of the data matrix, $\mathbf{C}_{\tilde{\mathbf{m}}}$, given in Equation (6.2) are then used in the analysis. Theoretical analysis given in (Fang & Cumberbatch 2005) explains that there is a strong relationship between the leading eigenvalue of the data matrix and corresponding liquid volume fraction. The following sections provide the results of three basic flow patterns.

6.1.1 Identification of stratified/layered flows

Static layered flows of liquid were generated in the horizontal pipes. 56 mm and 94 mm diameter pipes were used in the experiments. Liquid level was increased from 0 mm to the pipe diameter and inter-electrode measurements correspond to each level was collected. Interface levels were measured by using a ruler.

Static layered flows

Calculated eigenvalues of normalised capacitance data matrix against the interface level are investigated. Figures 6.1, 6.2 and 6.3 show results of water-air, water-oil and oil-air two phase flows respectively. It can be seen clearly that leading eigenvalue increases linearly with interface level, despite the type of components available in the separator section. The magnitude of the second largest eigenvalue increases with the increment of the interface height until the interface level reached around 60 to 70 mm and drops down to zero afterwards. Variations in other eigenvalues are not so significant compared to the first two leading ones. Dominant eigenvalues plotted against corresponding dense fluid fractions α_w in Figures 6.1 b) and 6.3 b) and α_o in Figure 6.2 b) show linear relationships between these two variables. Parameters of linear regression lines are given in the Table 6.1 below.

Table 6.1: Regression parameters which explain relationship between leading eigenvalue,Ei_d, and liquid fractions,$\alpha_{w/o}$,α_w and α_o.

Phases	regression line
Water and oil	$\alpha_{w/o} = 0.12Ei_d - 0.28$
Oil-air	$\alpha_o = 0.11Ei_d - 0.13$
Water-air	$\alpha_w = 0.12Ei_d - 0.19$

Gradient of the regression line is almost same in all three instances, though there is around 0.15 and 0.05 offsets between them. Figure 6.4 shows the variation in leading eigenvalue in all three two phase combinations together. Linear relationship between interface level and magnitude is more similar despite the flow components in the pipe section.

When one of the components is water, the uncertainty around the linear regression line is high. Deviation from the linear relationship is significant around $\alpha = 0$ and $\alpha = 1$, when water is present. Such a behaviour was also observed in the ANN based interface level estimation

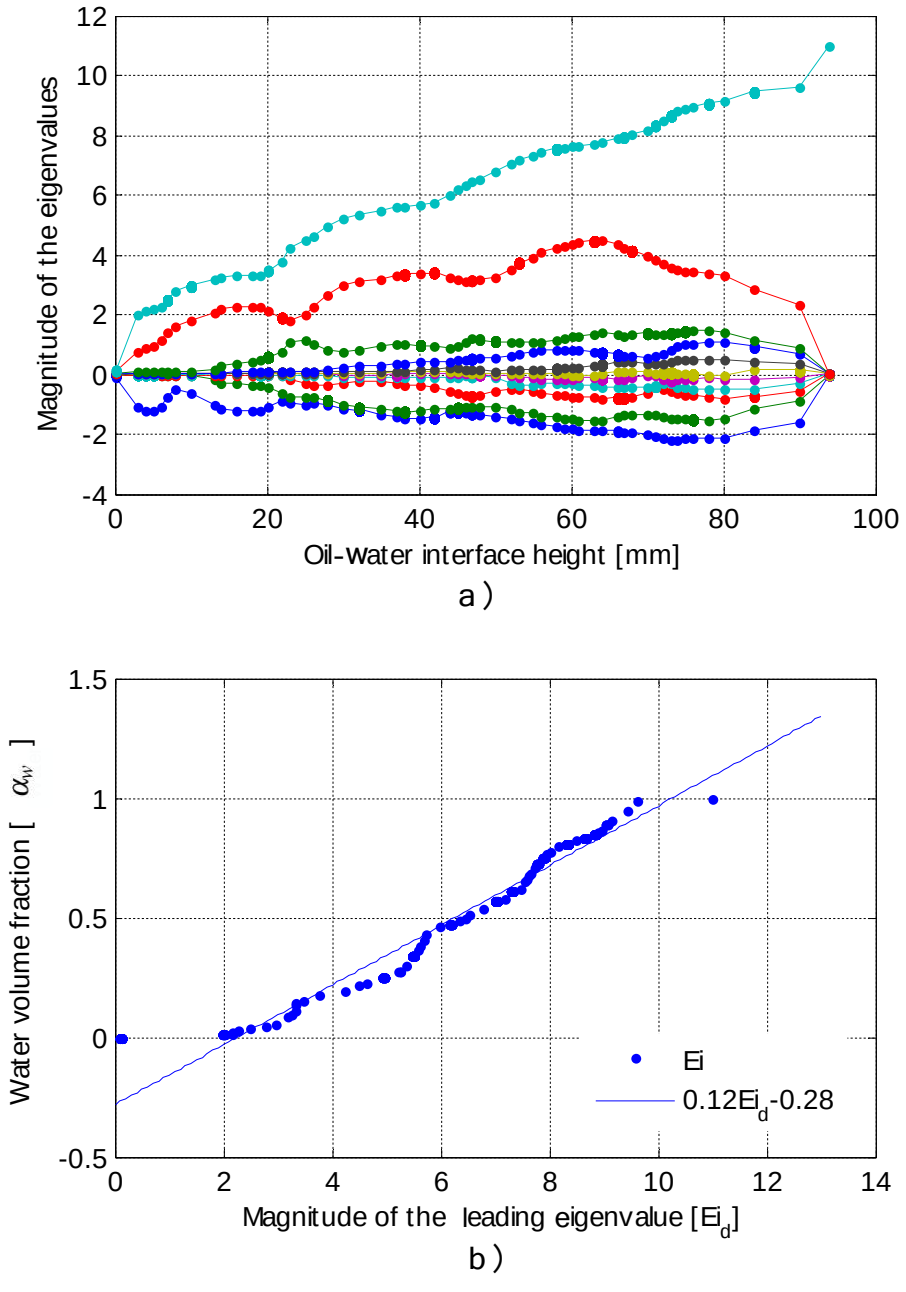

Figure 6.1: a) The eigenvalues Ei plotted against the interface height for oil-water stratified layers b) relationship between Ei_d and α_w

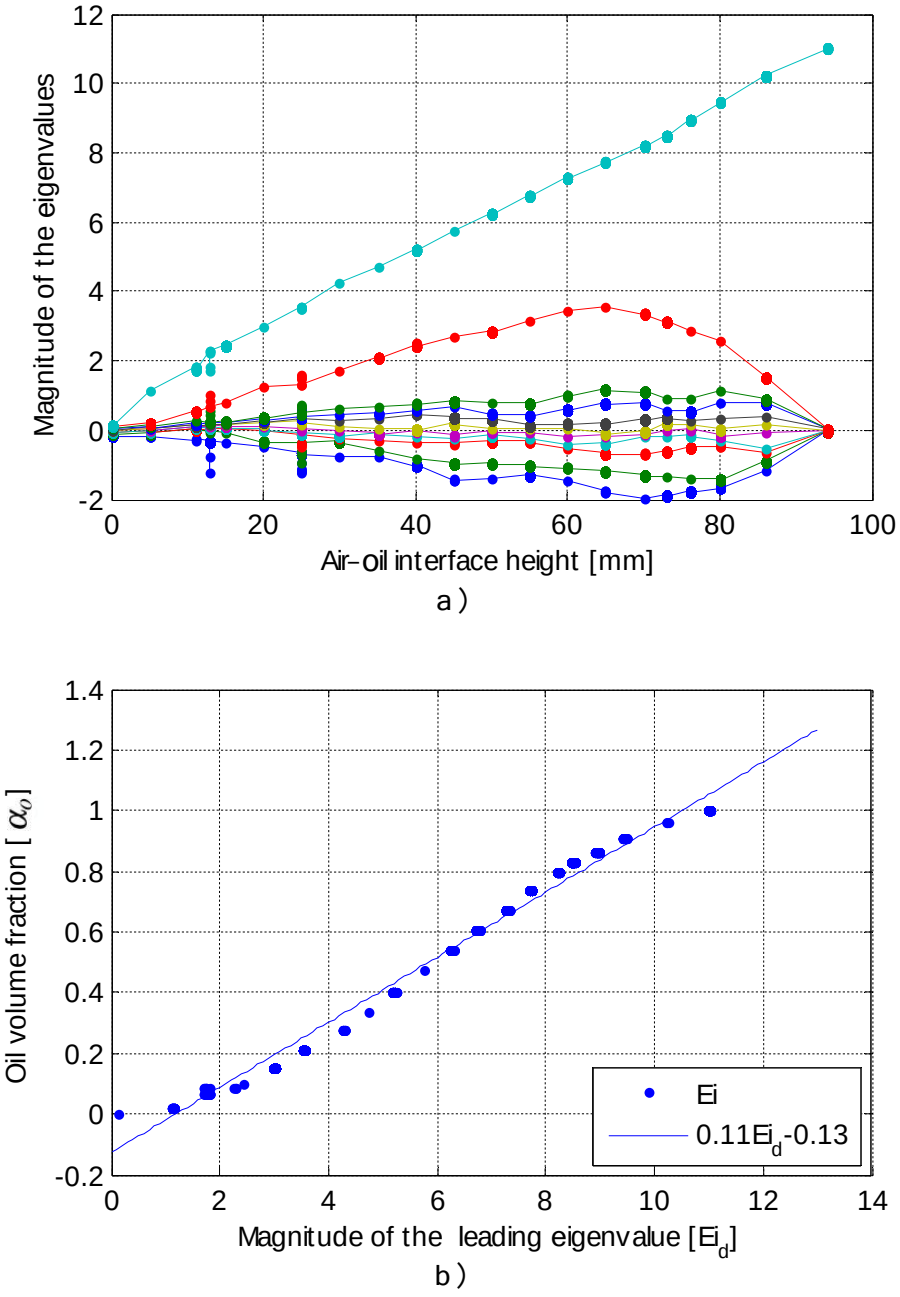

Figure 6.2: a) The eigenvalues Ei plotted against the interface height for air-oil stratified layers b) relationship between Ei_d and α_o

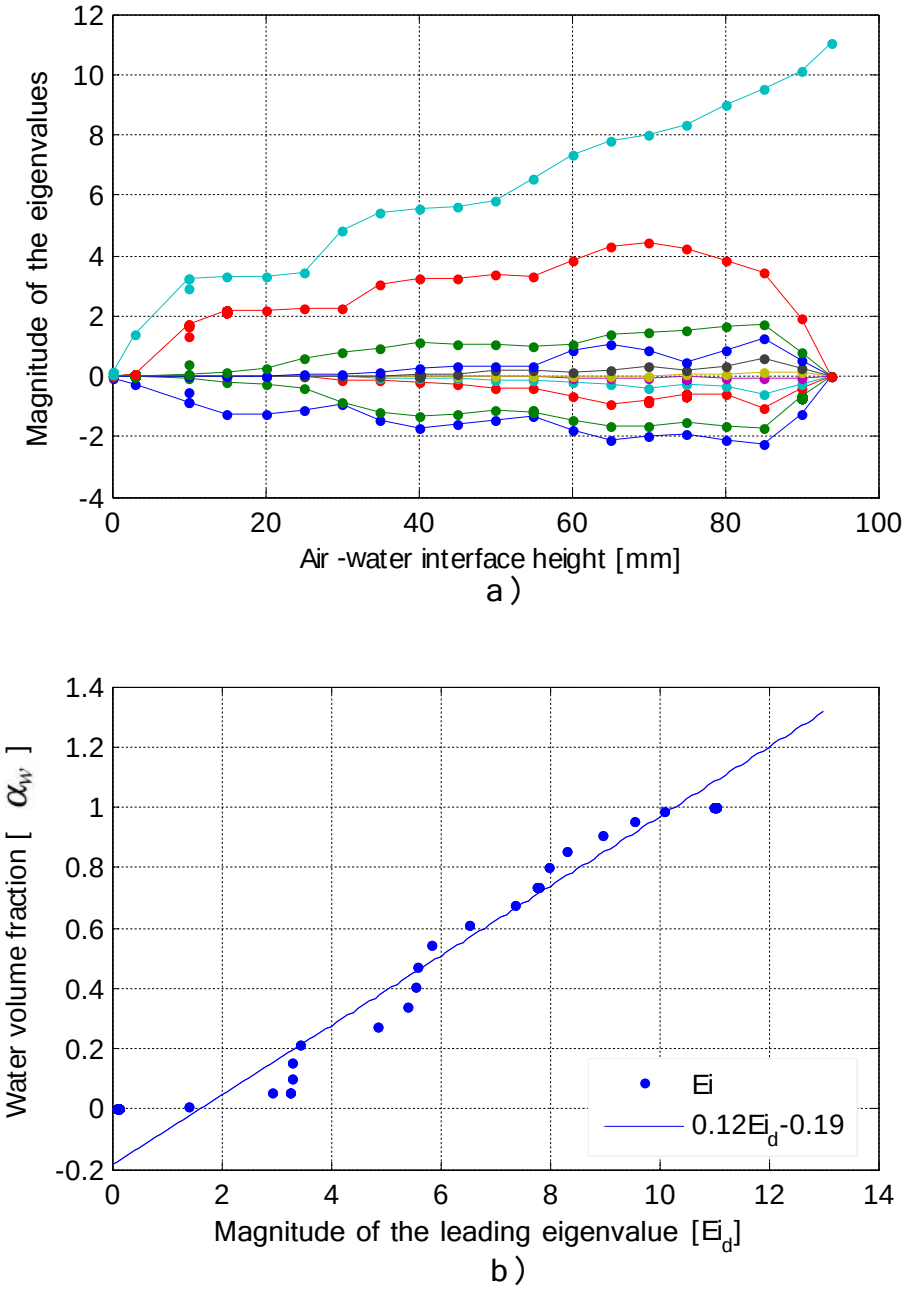

Figure 6.3: a) The eigenvalues Ei plotted against the interface height for Air-water stratified layers b) relationship between Ei_d and α_w

discussed in the Chapter 4. However, when two components are oil and air, variation is more linear and deviations from the regression line are minimal even at the zero and fully developed oil levels. It can be clearly noticed in Figure 6.4 a) and b) that leading eigenvalue has a better linear relationship with interface level compared to the volume fraction. Figure 6.4 b) shows that the magnitude of the eigenvalues corresponds to volume fractions between 0- 0.2 and 0.8-1 is not linear. Corresponding interface levels shown in Figure 6.4 a), do not show such variations. This can be clearly observed with oil-air two phase flow results. Though, larger uncertainties at zero are common with most of the measurement systems. Here, the uncertainty of the interface level measurements has also contributed to increase of non-linearity mainly at lower volume fractions. However, the parameter, interface level (h_I) can only be available with stratified flows while volume fraction is applied in other flow pattern characterization. Hence, further analysis is done with increased focus on volume fractions.

Dynamic Layered flows

Measurements from the horizontal layered flow (two phase) in 56 mm diameter pipe was utilised in the further studies. An overview of a layered flow under inlet superficial velocities $U_{WS} = 0.33\,m/s$ and $U_{GS} = 0.33\,m/s$ is given in the Figure 6.5. As the figure clearly illustrates, interface level indicates in the camera image shows a good agreement with the interface information shown in tomogram. Measurement results also show that capacitance measurements between the electrodes pairs below the interface are larger (close to 1). Further investigations were performed by comparing Gamma measurement results presented by (Vestøl 2013) on the layered flow under the same conditions. Here, the liquid volume fractions were calculated based on the pipe geometry and interface level measured using single beam Gamma densitometry. Results, when two phases are air-oil and air-water, are given in Figures 6.6 and 6.7.

Figure 6.6 indicates a linear relationship between dominant eigenvalue and volume fraction as observed in the stagnant two phase layered flow studies.

The measurements available are not so sufficient to provide a firm conclusion that this relationship is linear for every possible layered heights and volume fractions. However, available dynamic and static layered flow results give strong evidences on such a linear relationship. Regression parameters calculated in static and dynamic flow measurements are somewhat different. This might be due to various reasons. One of them is due to incorrect volume fraction calculation. Volume fraction was calculated using interface level measurements and pipe geometry information. However, the interface height near the pipe wall is slightly different and do not take into consideration in the calculation. Some other primary cause might be the wetted pipe wall. Most of these layered flows are stratified wavy flows and therefore the larger wetted area an above the interface level can be followed. Since ECT measurements are very sensitive near the pipe boundary, it increases the capacitance values and thus the magnitude of the eigenvalues.

As shown in Figure 6.7, when two phases of the flow are water and air, this gets worse. Apart from the above given reasons, this might be due to common issue involved with conductivity and sensitivity effect involved with water in ECT measurements.

Despite all the reasons, identification of the stratified flow pattern looks possible with this approach without having many issues. All layered flow results shown in corresponding figures

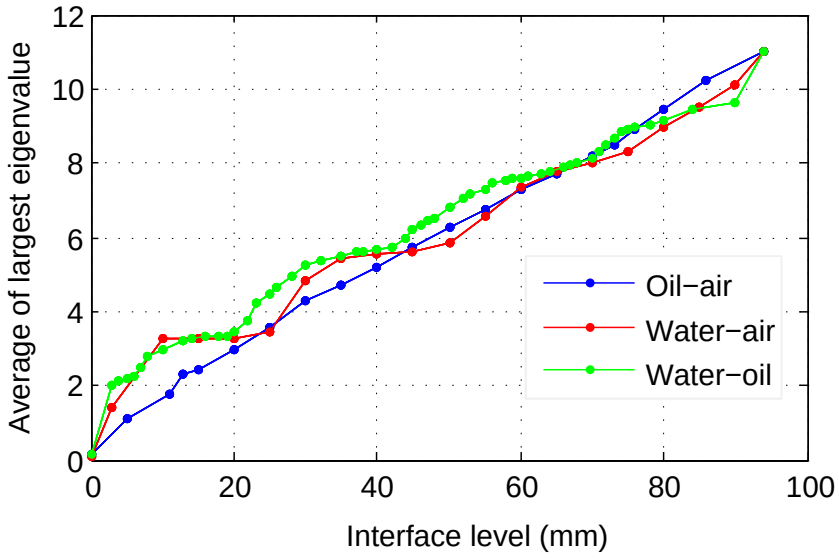

a) Level as a function of largest eigenvalue

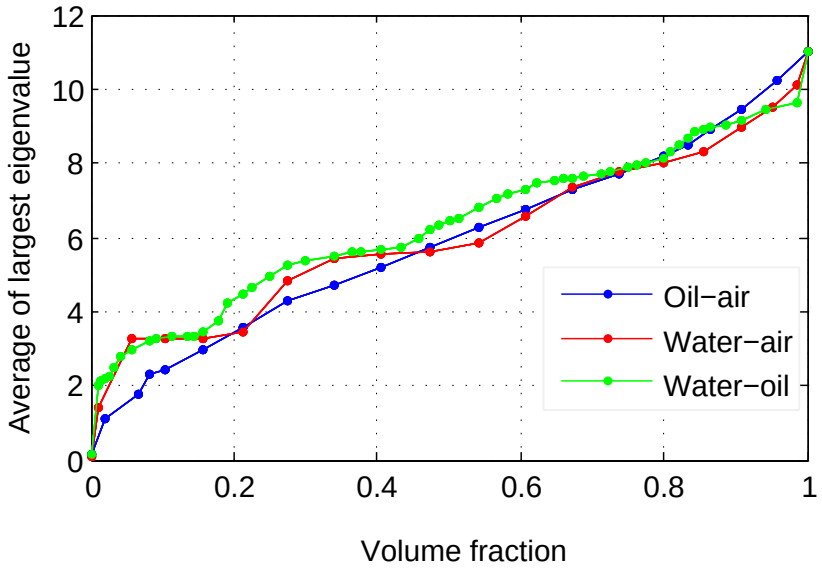

b) Volume fraction as a function of largest eigenvalue

Figure 6.4: Interface height and volume fraction of two phase layered flows against highest eigenvalue

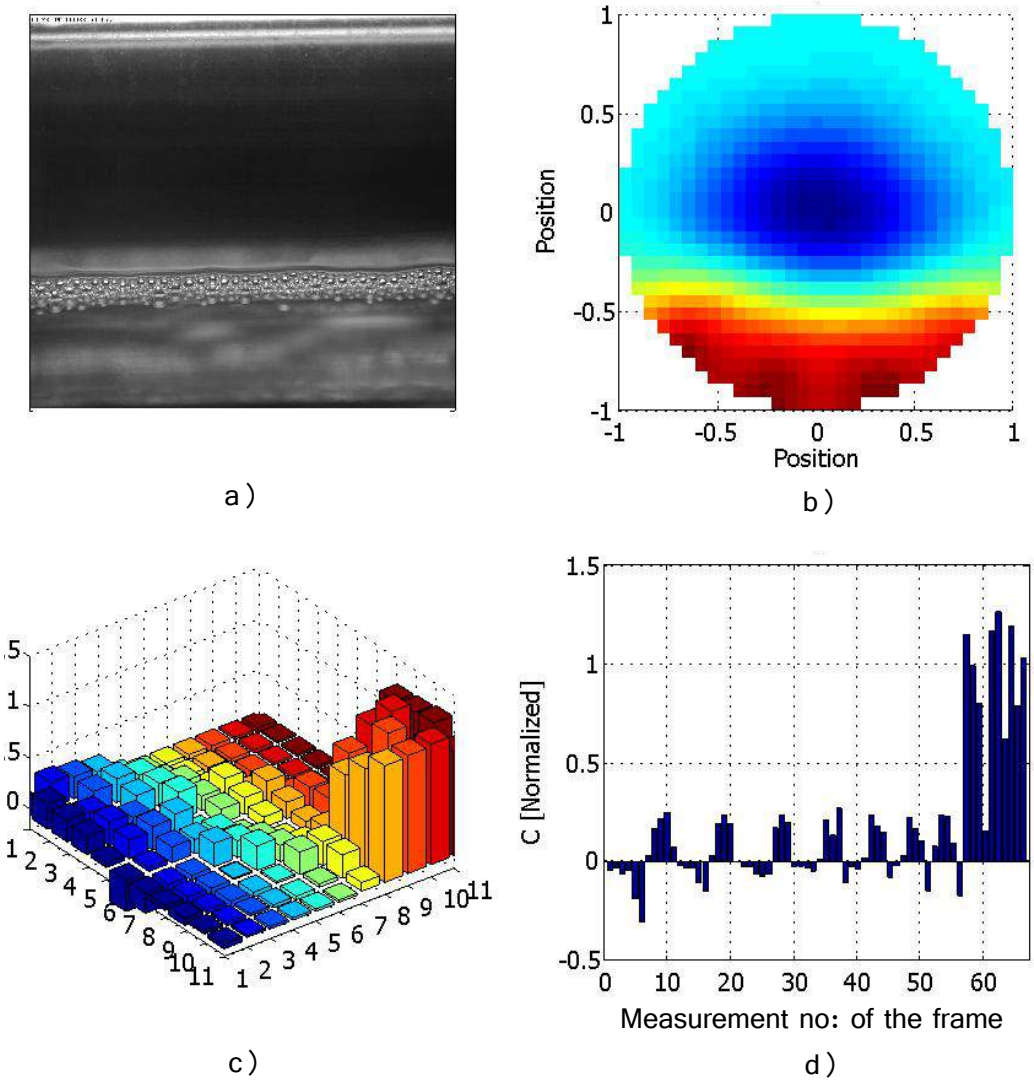

Figure 6.5: Layered flow observation with a horizontal flow under inlet component velocities $U_{WS} = 0.33\,m/s$ and $U_{GS} = 0.33\,m/s$. a) High-speed camera image b) Constructed ECT tomogram c) Data matrix d) Measurement in the data frame.

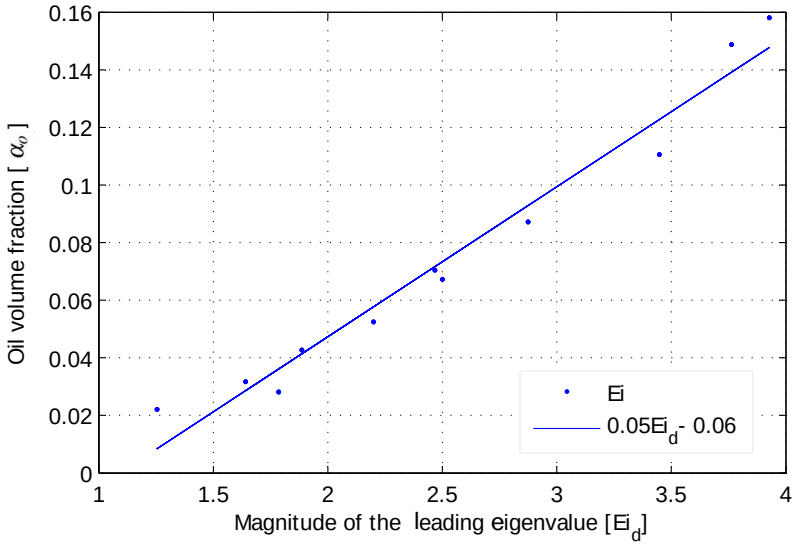

Figure 6.6: Oil fraction based on gamma measurements as a function of leading eigenvalue with regression line for comparison

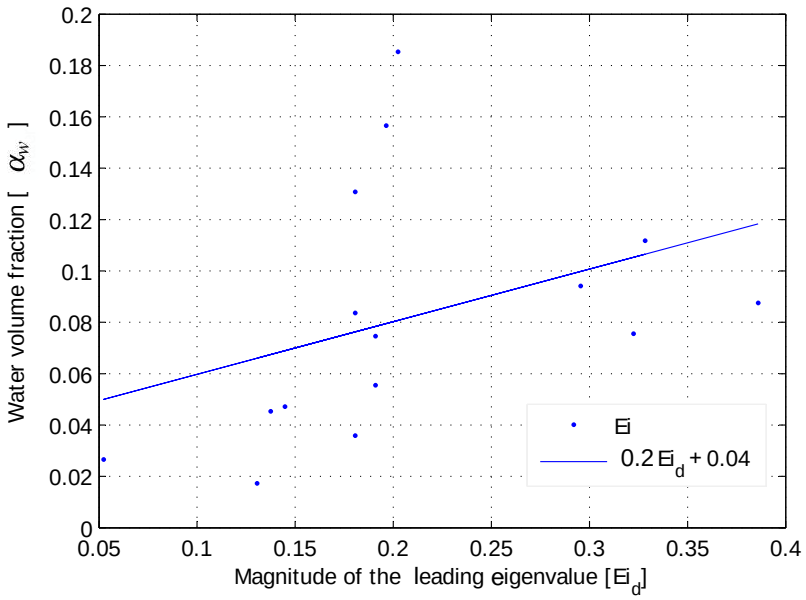

Figure 6.7: Water fraction based on gamma measurements as a function of leading eigenvalue with regression line for comparison

clearly suggest that second and third largest eigenvalues are having opposite signs as mentioned by (Fang & Cumberbatch 2005).

6.1.2 Slug flow identification

Same 56 mm diameter test section attached to the flow rig was utilised in the slug flow studies, but the test pipe section kept at $+1$ degree to the horizontal to generate slugs.

Inlet flow rates were first maintained at 30 kg/min, water and 0.35 kg/min, air. As explained in Chapter 5, slug body region and bubble region are the two clearly recognizable sections in a typical slug unit. High-speed camera images, corresponding ECT tomograms and constructed data matrices of those two typical flow regions are presented in Figures 6.8 and 6.9.

Figure 6.8 a), which is a high-speed camera image, shows a fully developed slug body region. Constructed ECT tomogram and capacitance data matrix explained in Figures 6.8 b) and c) also prove that most of the pipe cross-section covered by the sensor plane is filled with the water. Normalised inter-electrode capacitance measurements, used in the construction of the above tomogram are shown in Figure 6.8 d). Most of them have normalised capacitance values above 0.6. This observation indicates the dominance of the high permittivity component. Figure 6.9 corresponds to a typical bubble region of a horizontal slug flow. It is more like a stratified flow regime representation. Inter-electrode measurement distribution tomogram resembles the scenario presented in Figure 6.5, which represents a typical stratified flow.

Eigenvalue variations with regard to the water fractions under the above mentioned inlet flow conditions are given in Figure 6.10 a). Here, water volume fraction was calculated based on inter-electrode capacitance measurements as explained in Equation (5.1). Figure 6.10 a) clearly illustrates that the leading eigenvalue is positive and nearly linear as explained in (Fang & Cumberbatch 2005). The linear relationship shows the usability of the dominant eigenvalue in estimation of the water volume fraction as given in Figure 6.10 b). Figure 6.10 b) exhibits clearly a linear fit between α_l and Ei_d. The overall RMSE of the volume fraction estimate was 0.01 and the largest uncertainty of an estimate is found to be around volume fraction 0.4.

Transitions involved with slug flows in horizontal pipes can be described as sequential collections of levels in layered flows, which are increasing and decreasing their levels in transients. Similarities in eigenvalue variations in layered and slug flow presented in this chapter provide evidences.

Second and third leading eigenvalues marked in red and dark blue colours in Figure 6.10 a) show that their signs are opposite as observed with stratified flows. Even the distribution of eigenvalues and their variations along with increased water volume fraction shows that these types of slug flows are derivations of stratified flows.

Figure 6.10 c) which explains corresponding leading eigenvalue variations and volume fraction variations with respect to the time, clearly illustrates the fact again that largest (dominant) eigenvalue has similar dependency on the volume fraction signal. Hence, it should be possible to use this largest eigenvalue variation to extract some slug parameters as did with volume fractions in Chapter 5.

Unlike layered flow studies, there was no any method available to measure the actual water volume fraction to compare with dominant eigenvalue variations. To make a clear conclusion, these results should be verified with different techniques.

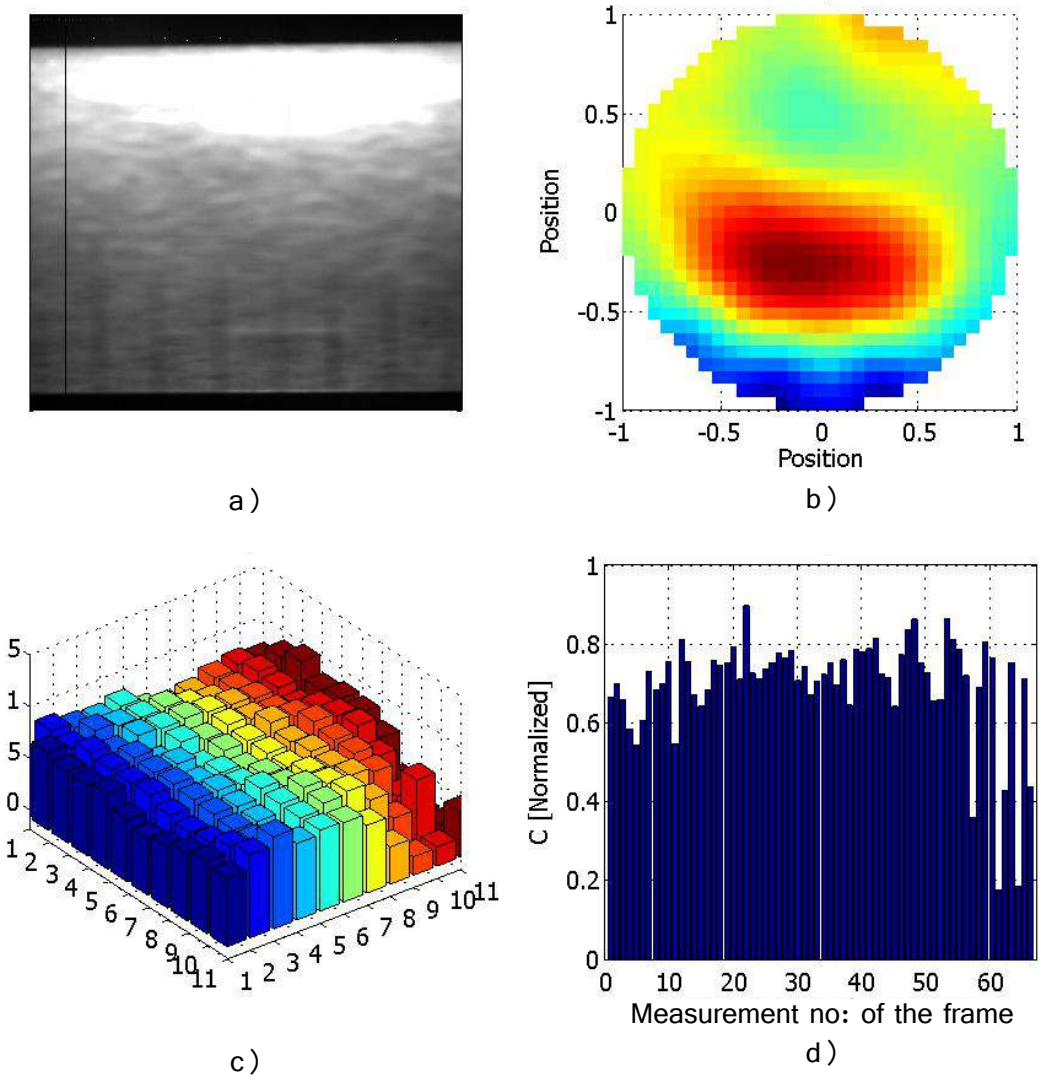

Figure 6.8: Liquid slug body observation with a inclined flow under inlet component velocities $U_{WS} = 0.20\,m/s$ and $U_{GS} = 2.39\,m/s$. a) High-speed camera image b) Constructed ECT tomogram c) Data matrix d) Measurement in the data frame.

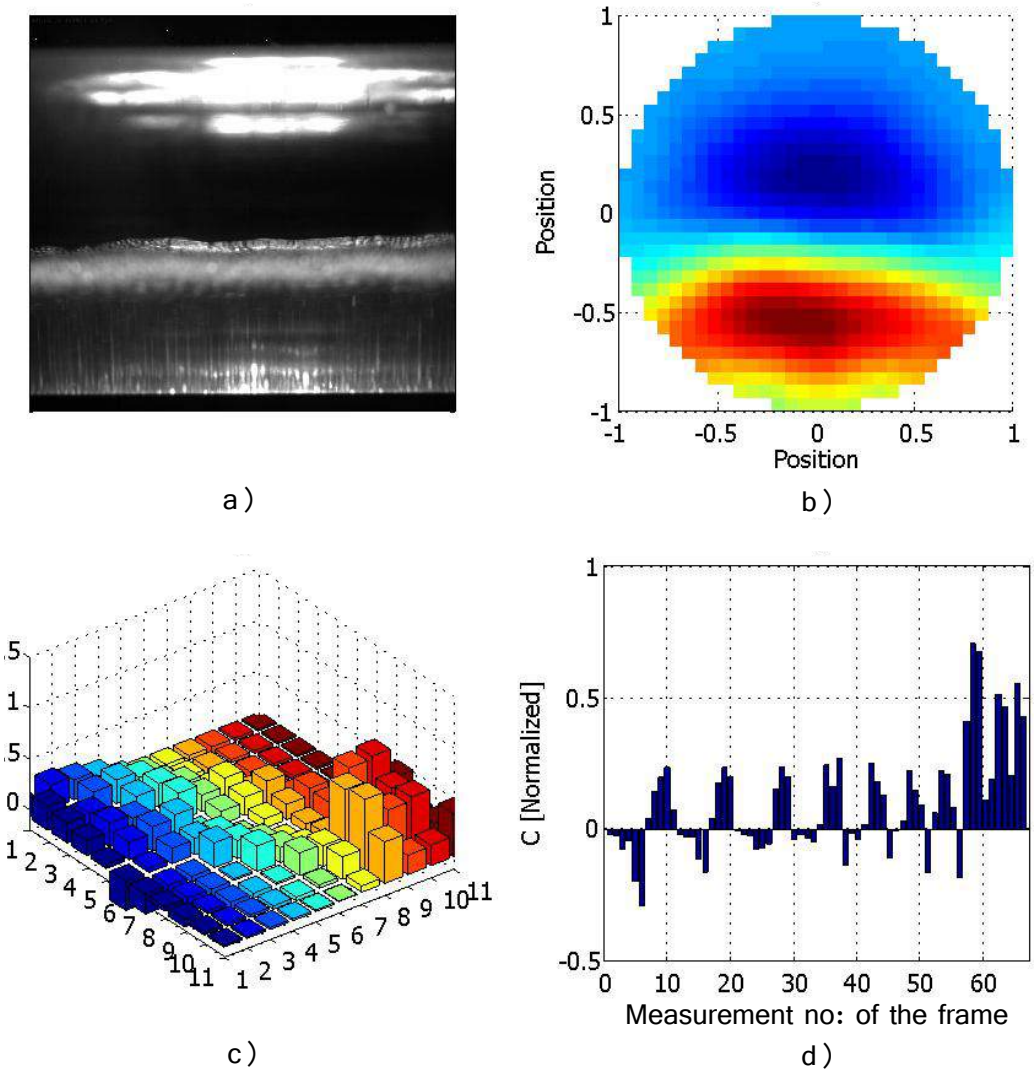

Figure 6.9: Taylor bubble of a typical inclined flow under inlet component velocities $U_{WS} = 0.20\,m/s$ and $U_{AS} = 2.39\,m/s$. a) High-speed camera image b) Constructed ECT tomogram c) Data matrix d) Measurement in the data frame.

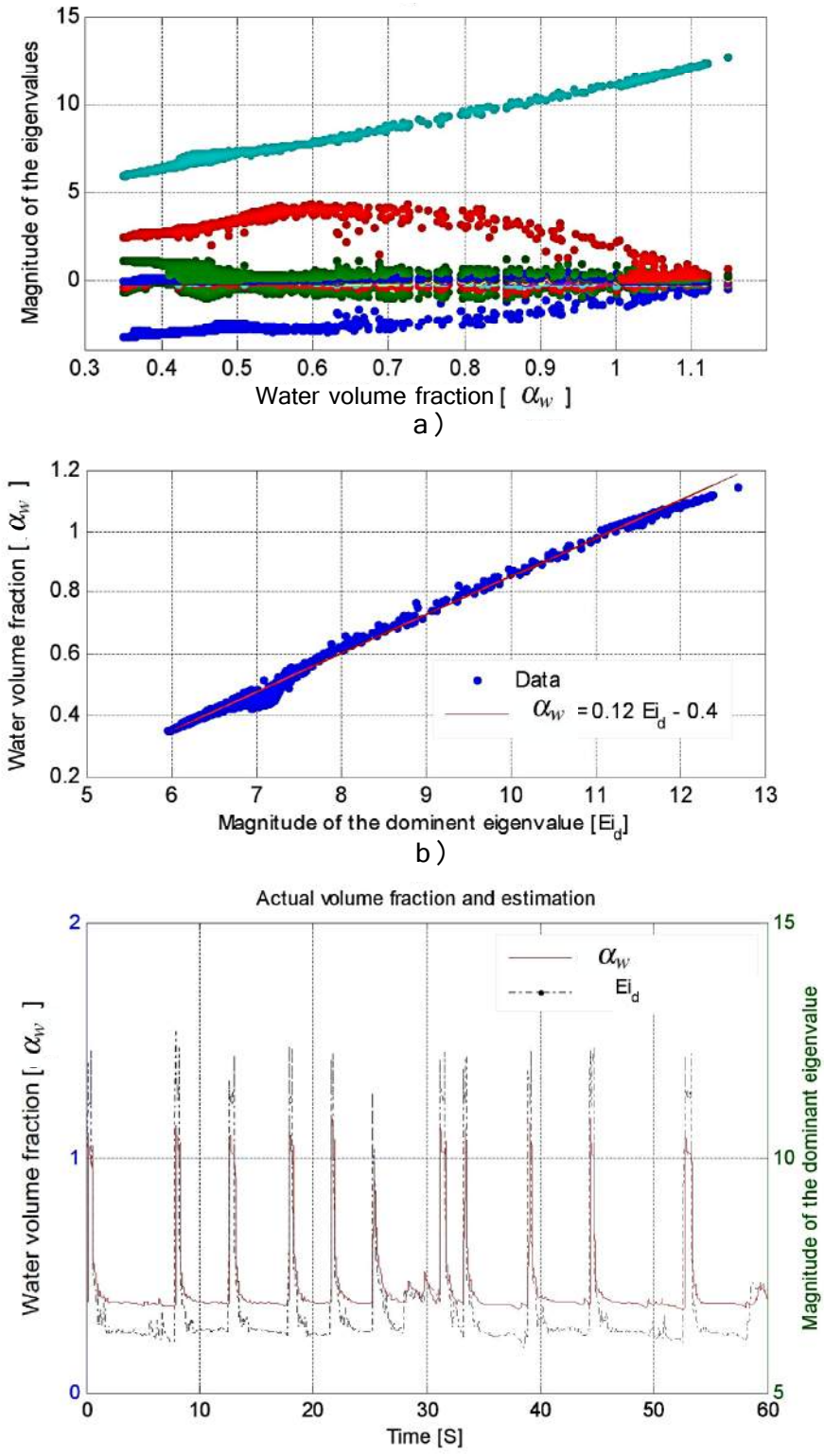

Figure 6.10: Eigenvalues of normalised capacitance matrices against water fraction for the slug flows

6.1.3 Annular flows identification

To create static annular flow distributions, plastic hollow tube arrangements with different diameters were used. Figure 6.11 shows core sizes and distances from the center line. Though, there are only three different core sizes available, constructed tomograms can be used to distinguish the sizes. These static core flow representations cannot be useful to identify how the eigenvalues vary with the varying liquid fractions due to insufficient data points, but it shows where first three eigenvalues are and hence can be used in detecting flow regime as explained by (Fang & Cumberbatch 2005). The results correspond to the cross-sections given in Figure 6.11 are shown in Figure 6.12. As shown in the figure, dominant eigenvalue has the highest magnitude and second and third largest eigenvalues approximately same in magnitude but signs are opposite. Both air-water and air-oil two phase flows show the same behaviour.

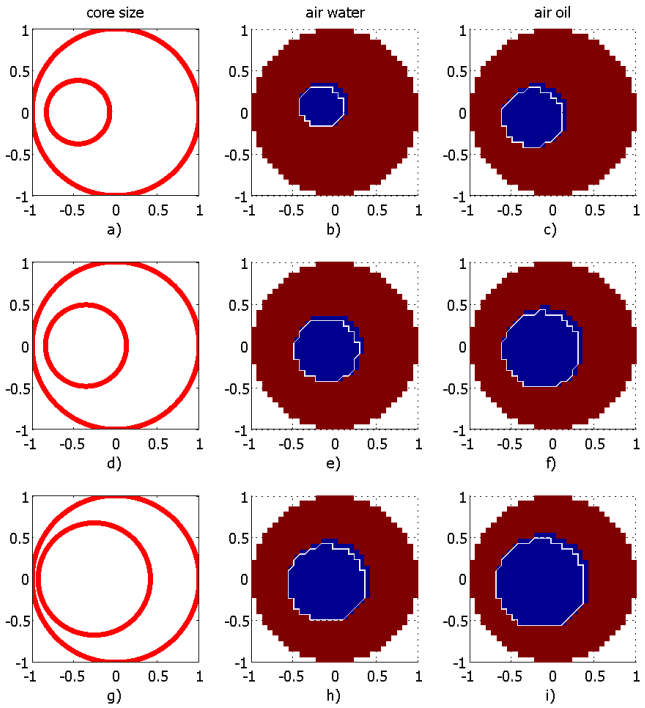

Figure 6.11: Core sizes and corresponding tomograms when two phases are air-water and air-oil. Distance between pipe center and core center for given three different cases are given with core diameters as in a) 28 mm and 31 mm d) 21 mm and 45 mm g) 15 mm and 64 mm

ECT measurements of the annular flow generated in the multiphase flow loop were also analysed and the results are given in the Figure 6.14. It can be found out in the figure that dominant eigenvalue is positive and increasing with the addition of the high dense component, oil (in this experiment).The second eigenvalue is almost similar in magnitude, but has the negative sign. Third and fourth show similarity in magnitude, but has the opposite signs.

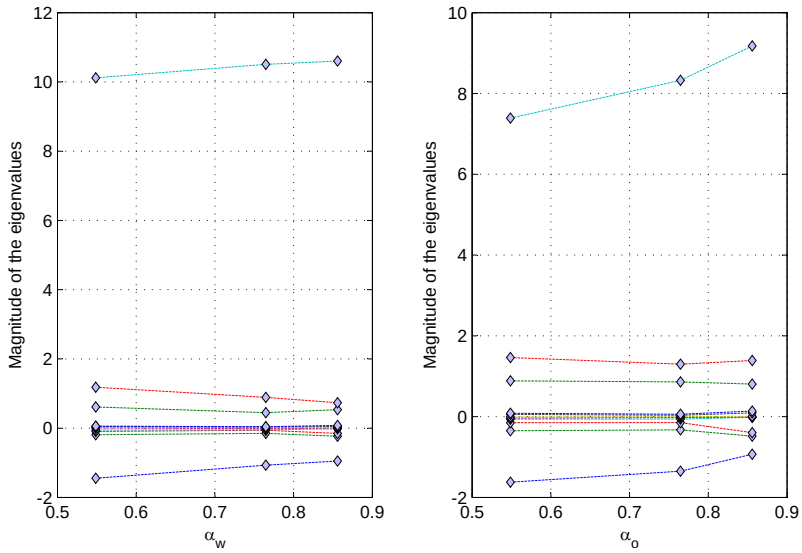

Figure 6.12: Eigenvalues corresponds to the flow representations given in Figure 6.11

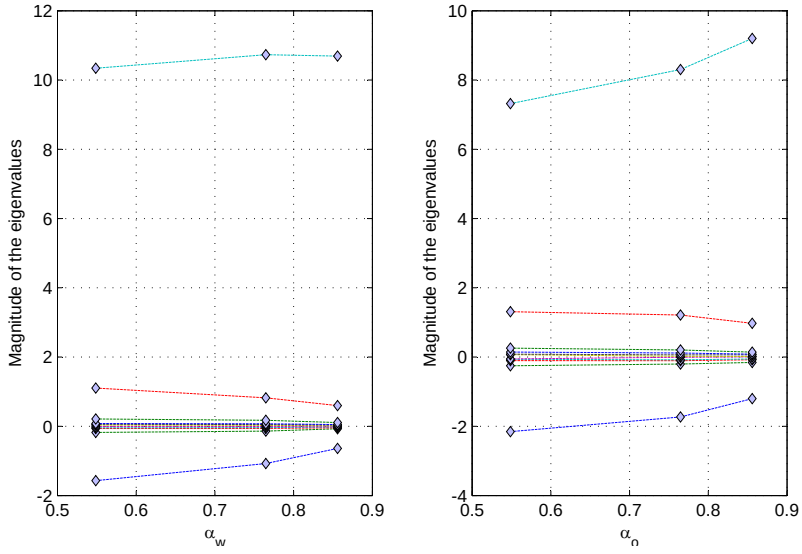

Figure 6.13: Eigenvalues corresponds to centric annular flow

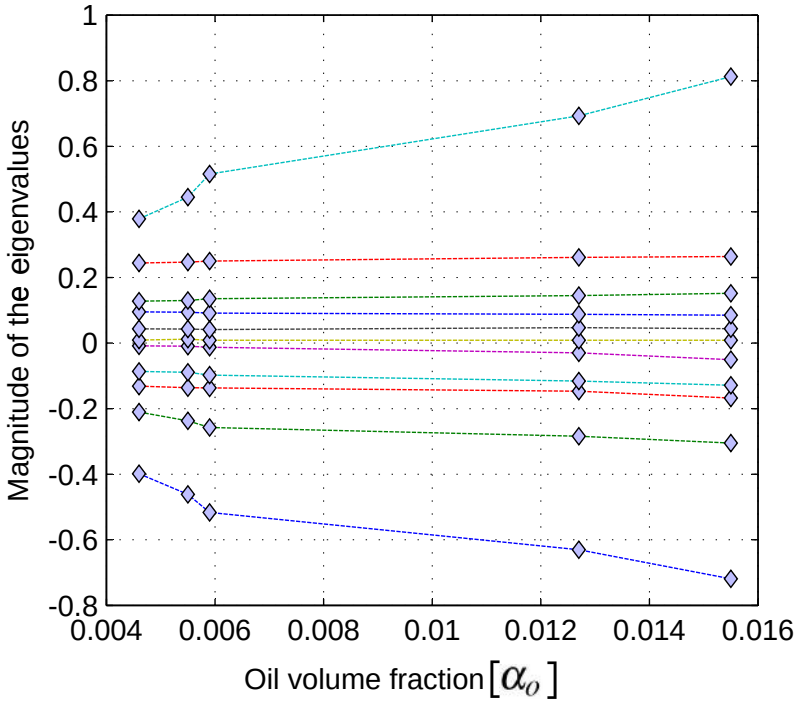

Figure 6.14: Eigenvalue of capacitance matrices corresponds to air-oil two phase flow experiments

Though (Fang & Cumberbatch 2005) says that second and third dominant eigenvalues have opposite signs, both are observed on the negative side of the figure.

Third dominant eigenvalue would not be so significant, if volume fraction goes over 0.55, as discussed by (Fang & Cumberbatch 2005).

6.1.4 Discussions on basic flow identifications using matrix properties

(Fang & Cumberbatch 2005) has explained that the leading eigenvalue is a solid indicator of the liquid volume fraction variation based on simulation results. Results from both static and dynamic layered flow experiments show that relationship explained is similar. They have further explained the possible verification with second and third eigenvalues. According to them, second and third dominant eigenvalues should have opposite signs. A very good agreement can be found from the analysis of experimental data given in Section 6.1.1. The slug phenomena in horizontal flows can be represented as a collection of layered flows with increasing interface height as explained in an above section. Corresponding results show that this explanation is acceptable.

Since just three different phantoms were used in the annular flow studies, it is hard to establish a statement based on those results. But, one thing can be distinctly observed that second and third dominant eigenvalues are approximately same in magnitude, while having opposite

signs. This does not agree with the results made by (Fang & Cumberbatch 2005). According to them, they should be positive and approximately equal. Results from dynamic flow experiments contain very low liquid fractions (less than 0.015). In accordance with further explanations given by (Fang & Cumberbatch 2005), for such small liquid fractions those characterizations may not be accurate. Hence, more experiments with higher liquid fractions are required for further investigations and validations of these techniques.

6.2 Reverse flow detection

In multiphase flow applications involved with oil and gas production and transportation safety is the key focus due to the high risk involved. Apart from the studies on the risks involved with forward flow and their relationships with different flow patterns and parameters, reverse flow detection and prevention also important in practice. It can be seen in recent developments in multiphase flow metering instruments that apart from the flow component estimations, they are trying to include the reverse flow detection as an additional option. Though ECT is a promising technique in multiphase flow metering in pipelines, possibilities of detection of flow reversing has not been investigated using this technique.

Construction of tomograms from inter-electrode capacitance measurements and image quality improvements were among the main research focusing for last couple of decades. But, the feasibility of getting flow component information from such images is minimal as explained by (Yang 2011).

After the extraction of oil with other fluids in sub-sea installations, they are transported to the offshore platforms and then to onshore platforms. The orientations of the transportation pipelines among platforms and oil wells are varied and upward inclined sections can be seen frequently. Possible reverse flow detection within such sections is studied experimentally in the lab scale facilities explained in Chapter 3. Reverse flows, which are associated with slug flow patterns are investigated here, with the view of detecting the reversing immediately to prevent possible damages to the actuators and other system components. Electrode arrays of twin plane capacitance sensor connected to the ECT systems are used here in measurements from each plane. Here, the flow reversing is studied without making any modification to the available ECT systems.

Possibilities of using cross-correlation technique for the detection of the reverse flow in similar two phase gas-liquid flows have been mentioned in the (Bertani et al. 2010). Conducting probes have been used in measurements there. Electromagnetic flow-meters, which are used to measure conducting liquid flows, can detect both forward and reverse flows.

As emphasised in the Chapter 4, fast estimation is more important in measurement and control applications than the accurate tomogram construction, which is time consuming. To cope with such requirements, tomometric approach that is discussed in this section would be more reasonable. Recent experimental studies on inclined pipe flows indicate that depending on various settings of the parameters such as pressure, flow rate, inclination angle etc influence on both flow velocity and the flow direction (Corneliussen et al. 2005). Change in flow direction can affect the hardware installations of pipelines, particularly if the flow is dominated by slugs.

This section explains how to detect the flow direction using twin plane electrical capacitance

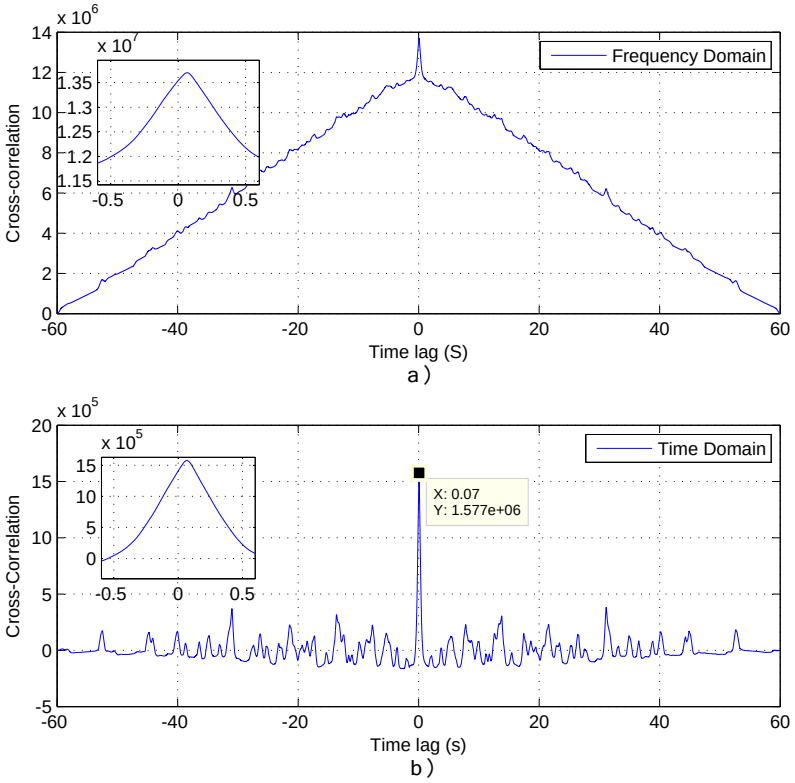

Figure 6.15: Cross-correlation of volume fraction signals from plane 1 and 2 in time and frequency domains

tomometry, and cross-correlation of the time series of raw capacitance values. This kind of information is very useful for process engineers to take actions to prevent possible damages to the system.

6.2.1 ECTm Correlation approach

Data processing in tomometric approach is same as explained in Chapter 4. Results of the experiments under air-water mixture velocity, U_{mix}, $5\,m/s$ and liquid fraction, α_w, 0.01 is discussed. According to the Equation (5.3) used in the slug flow velocity estimations in Chapter 5, the maximum measurable velocity with the use of cross-correlation technique will be at time lag 0.01s ($1/f_{cap}$). This discriminate the time lag between two signatures by $1/2f_{cap}$. This can be obviated to a certain extent by interpolating data points around the peaks of correlation profile. This approach has been discussed with more details by (Long 2006).Capturing high-speed camera images are used to verify the reversing. More information can be found in attached Paper 2. Typical cross-correlation function of two time series signals of volume fractions is shown

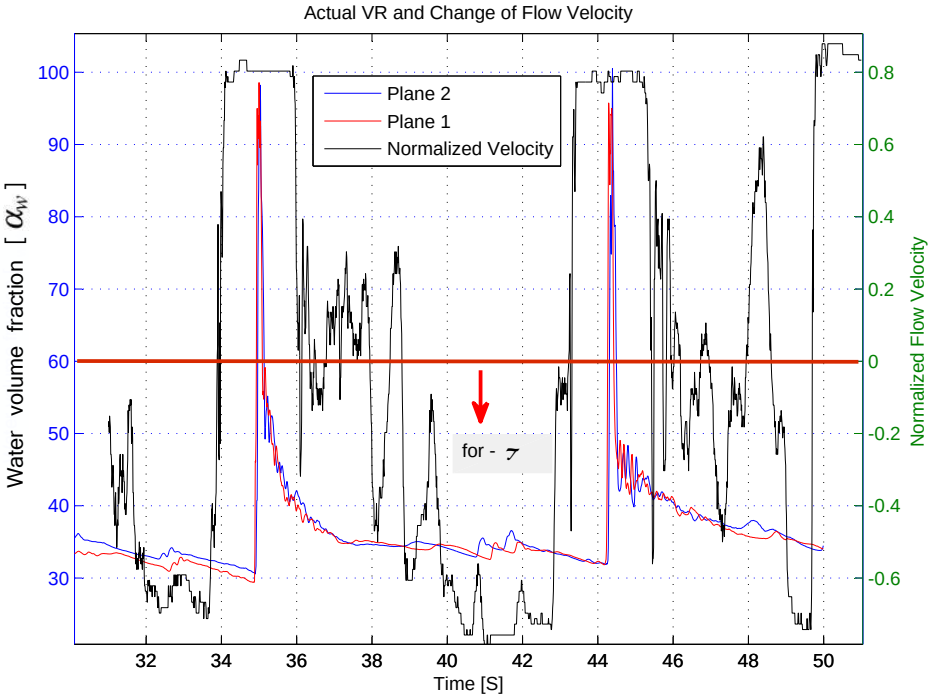

Figure 6.16: Reverse and forward flow indication with cross-correlation

in Figure 6.15. Since two signals correlated are 60s long, time lag extracted is mainly from slug front, which is the most dominant. Since the reversing appears in the Taylor bubble region, selection of the correlation window is the key thing in the reverse flow identification.

Several sets of experiments with flow reversing were performed with different inlet flow parameters. Measurements of the twin plane ECT system were sufficient to identify the reversing without any modification to the arrangement.

How this correlation based approach works, is depicted in Figure 6.16. Here a moving window of the 2s was used in each cross-correlation and only the sign of normalised velocity is sufficient to identify the flow direction.

6.2.2 Discussion on reverse flow identification using tomometric signals

When the correlation window becomes too large, this reversing information cannot be observed and dominant slug translational velocity will be indicated. Hence, the selection of correlation window is more important. But, the possibility of implementing a system to detect flow reversing without having any modification to the system would be an added advantage.

Chapter 7

Dynamic Time Warping (DTW) technique for slug length estimation

7.1 Process description

ECT measurements can easily be combined with other measurements to extract process parameters. Most of the research groups are now getting ECT systems in their facilities with the view of fusing them with other measurements and having improved estimations. Almost all measurement techniques have different strengths and weaknesses. Hence, a fusion of measurements from different types of techniques produces much improved and reliable information.

Pressure is one well known governing parameter in flow processes. Hence having pressure measurements are vital in process studies. Differential pressure measurements facilities are available at the multiphase flow rig at TUC and DP measurement points and placements of ECT sensors are as given in Chapter 3.

Pressure and liquid volume fraction signals (from ECT) are warped to identify liquid slugs in water air two phase flows here. Results are discussed in this chapter. The studies are restricted only to slug flows with focus on early slug detection and timely characterization of those slugs.

Dynamic Time Warping (DTW) is typically used to align two signals optimally. Characteristic slug pulses occur in time series signals of the pressure and ECT are warped in this study. Unlike a typical DTW application, two signals are being warped are not captured simultaneously.

7.2 Signal arrangement and DTW

Experiments were restricted to slug flow studies. Some measurements of air-water two phase flows performed under atmospheric outlet pressure and room temperature are used in the analysis. Signals from the twin plane ECT system and differential pressure signals from PDT120 were selected. Pipe inclination was kept at $+1^{\circ}$ to the horizontal plane to generate slugs conveniently. More details on flow and measurement facilities can be found in Chapter 3. Data from experiments performed under inlet flow rate of water 50 kg/min was selected. Here, only inlet air flow rates were changed for each experiment. They were between 0.05 kg/min and 0.5 kg/min

as given in Table 7.1.

Table 7.1: Inlet flow parameters of each experiment.

Test no	Air flow rate kg/min	warer low rate kg/min
1	0.10	
2	0.25	
3	0.3	50
4	0.35	
5	0.4	
6	0.45	

Volume fraction, α_w, was calculated utilizing the equation given in (5.1).

Dynamic time warping is a widely practiced technique in many speech and image processing algorithms, especially in similarity study of various signatures. Typically signals used in DTW are time series. DTW is a versatile tool in data mining applications, where there is a need for detecting "matches" in many sets of time series. The sets of time series are warped in the temporal domain somewhat non-linearly under some constraints. As such, DTW is a useful tool in sensor data fusion in process industries, where the tags can run into thousands and data can run into the Taylor Bubble (TB) regions. Basic formulation of DTW technique for two time series signals is explained briefly in Section 2.2.5

7.3 Slug characterization

Slug flow parameter estimated under above mentioned experimental conditions were also part of the studies discussed in the Chapter 5. Inter-electrode measurements from the twin plane ECT system were used for the calculation of water volume fractions (α_w) separately as given in Equation (5.1). Then, they were cross-correlated to estimate the slug velocities (U_s) for each test. These calculated slug velocities are important in the slug length calculation. Using Equation (5.5), each slug length (L_s) can be estimated. t_s is the difference between times in tail and front of the particular slug. Similarly, lengths of all slugs are estimated.

Due to the complex nature of the slug boundaries, as given in the Chapter 5, a threshold value was introduced to locate the liquid slug body region. Selected threshold was 0.7 for this analysis. Once α_w crosses this threshold from a lower value, that point is selected as the slug front. When the threshold is reached from higher α_w that point is registered as the slug tail. This is how the time difference, t_s, used in the Equation (5.5) is calculated.

Differential pressure signal, D_p, from DP121 sensor was also captured along with ECT measurements. D_p signal and α_w signal were warped to have optimum signal alignments. Unlike α_w signals, D_p signals alone do not indicate any clear information on individual slugs. However, the warped signal of D_p on to the α_w follows the variations more similar to the α_w with different peak magnitudes, which are proportional to the slug lengths. The magnitude of a typical peak of a warped D_p is marked as h_{Dp} in Figure 7.5. It can be clearly seen in the figure that warped D_p signal gives its peak within the liquid slug body region of the corresponding slug. It eases

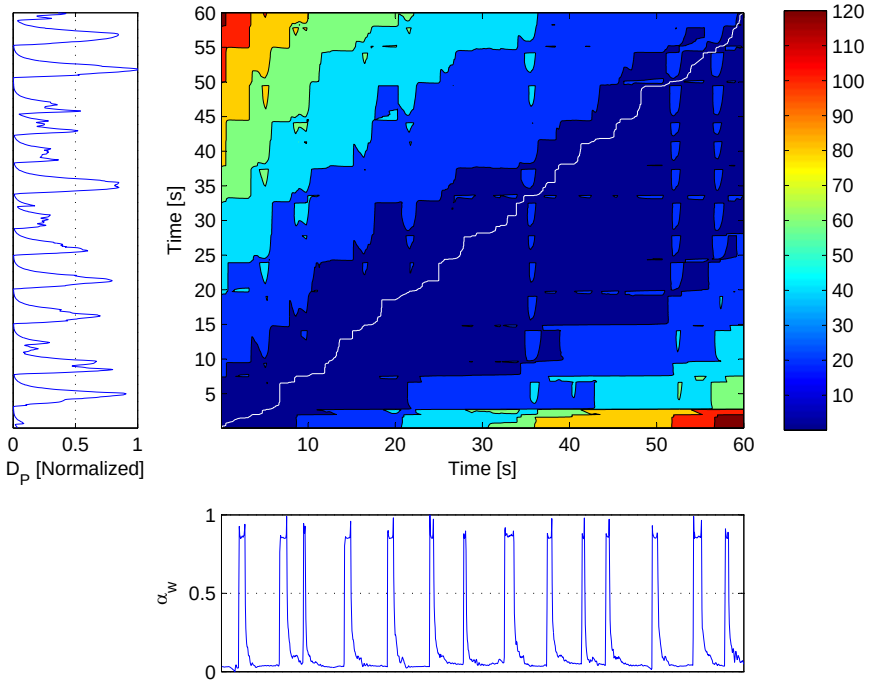

Figure 7.1: Distance matrix and warping path along with two signals, differential pressure, Dp, and water fraction, α_w,captured from test 2

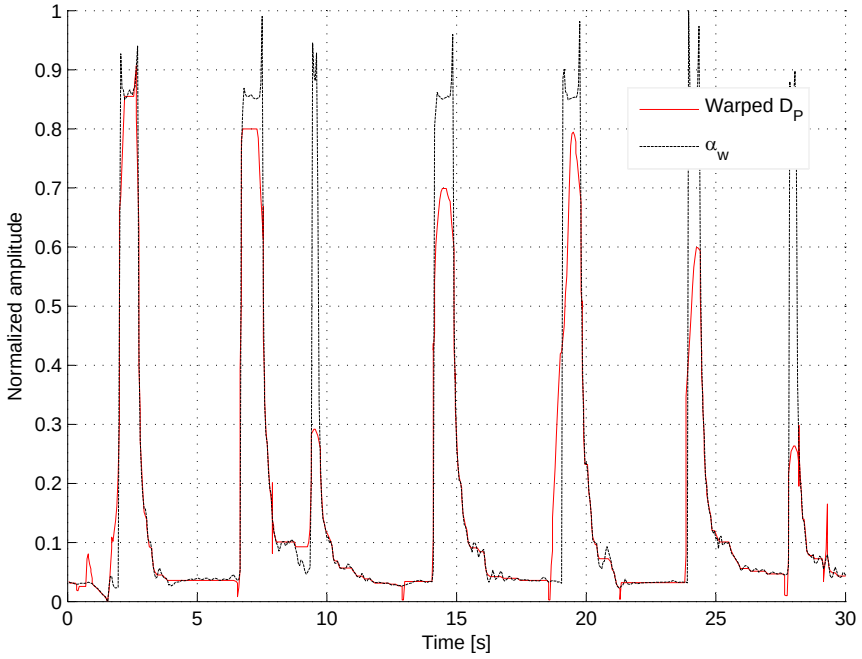

Figure 7.2: The warped signal of differential pressure, Dp, and water fraction, α_w, correspond to test 2, represented in a common time axis

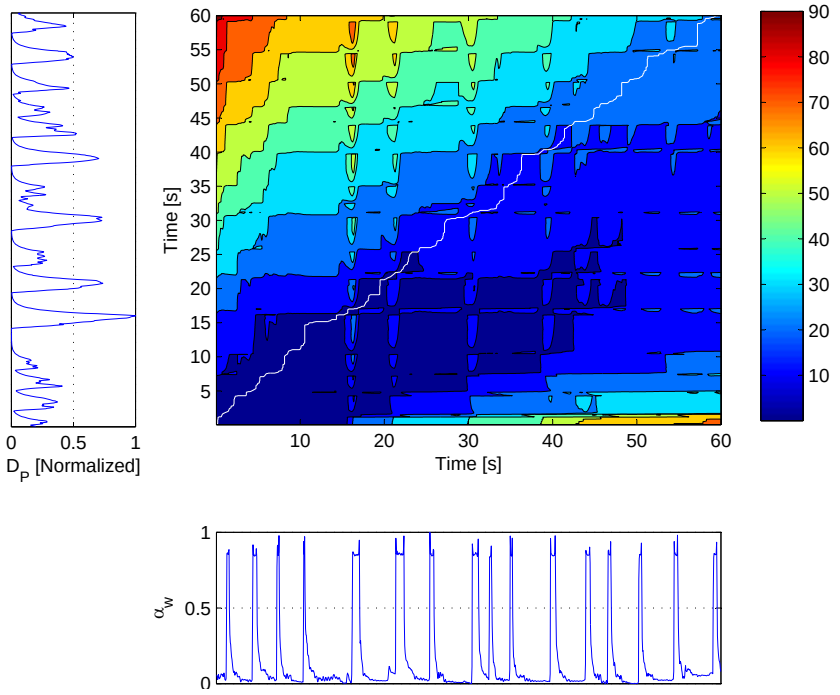

Figure 7.3: Warping of differential pressure, Dp, and water fraction, α_w, signals captured from test 1 along with distance matrix and warping path (white line).

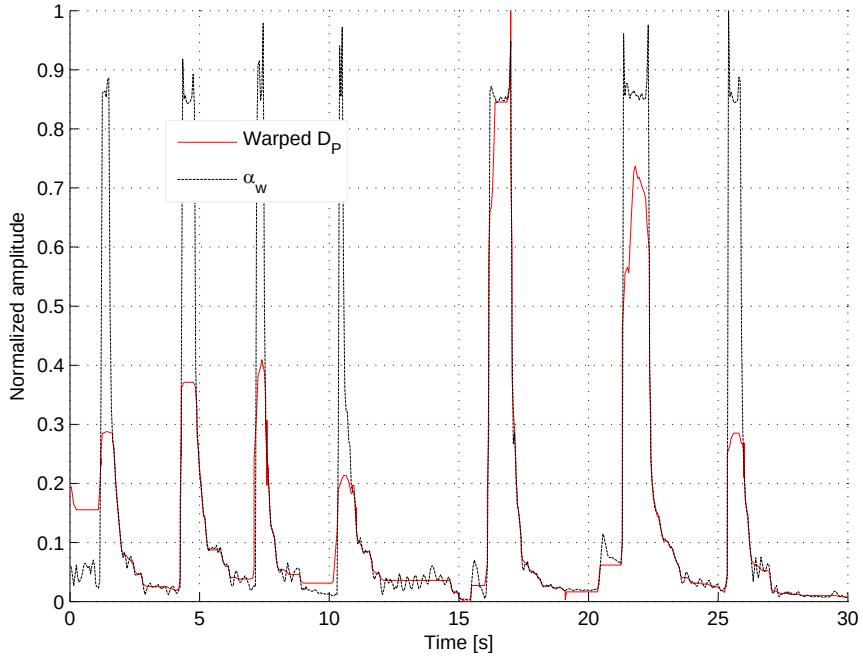

Figure 7.4: The warped signal of differential pressure, Dp, and water fraction, α_w, correspond to test 1, represented in a common time axis

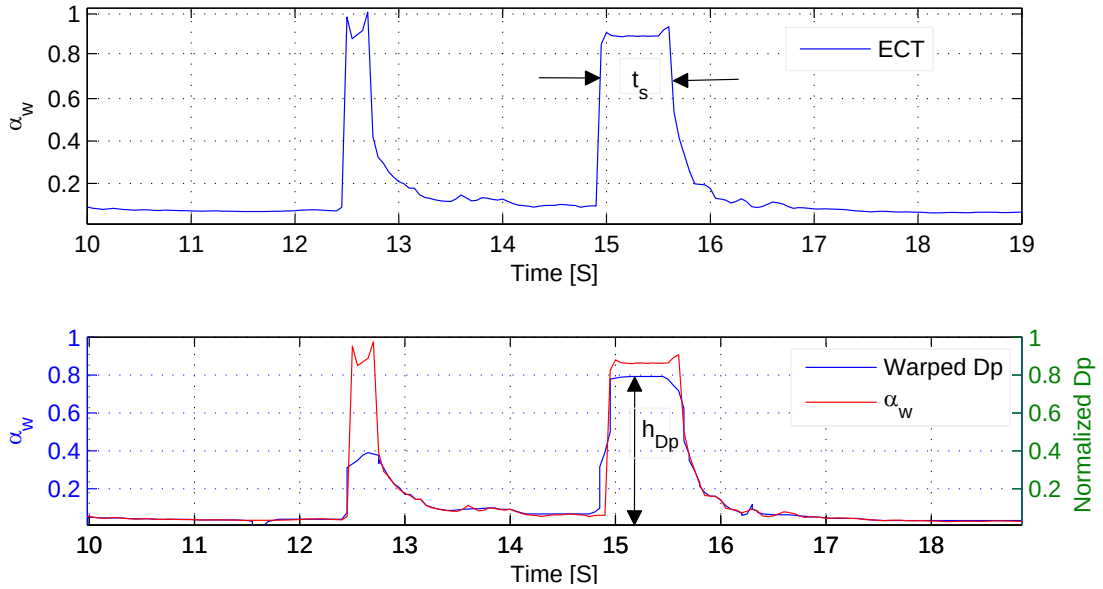

Figure 7.5: Warping differential pressure,Dp, on to water fraction signal, α_w, and selection of pressure peak, h_{Dp}, and time window of the slug

the selection of the h_{Dp}. Likewise, L_s of all slugs appeared in the experiment and corresponding h_{Dp} are collected. Flow chart given in Figure 7.6 summarises the whole procedure of estimation of slug lengths.

7.4 Co-operative data fusion to estimate slug parameters

D_p signal and α_w signal are given on left and bottom sides of the corresponding distance matrix in the Figure 7.1. Inlet flow rates maintained throughout the experiment were $0.25\,kg/min$ air and $50\,kg/min$ water (test 2). Warping path, P_w, is indicated in white on the distance matrix plot. Then, the warped D_p signal extracted from the warping path information with reference to water volume fraction signal is selected and plotted as in the Figure 7.2. Figure shows the mapping of differential pressure signal, D_p, onto the volume fraction signal α_w visualizing its hidden information.

Similar results are shown in Figure 7.3, where experiments were performed under $0.05\,kg/min$ air and $50\,kg/min$ water inlet flow rates (test 1). It can be seen from Figures 7.2 and 7.4 that positive-going ups and negative going downs of water volume fraction α_w and warped D_p are aligned properly with the plateau parts of these two time series also falling in the same time slots. It is interesting to note that for plateaus for a water volume fraction α_w with wider time slots, higher amplitudes of the differential pressure signals, D_p, can be observed.

Each individual slug length, L_s, was calculated as explained in the Section 7.3. Results

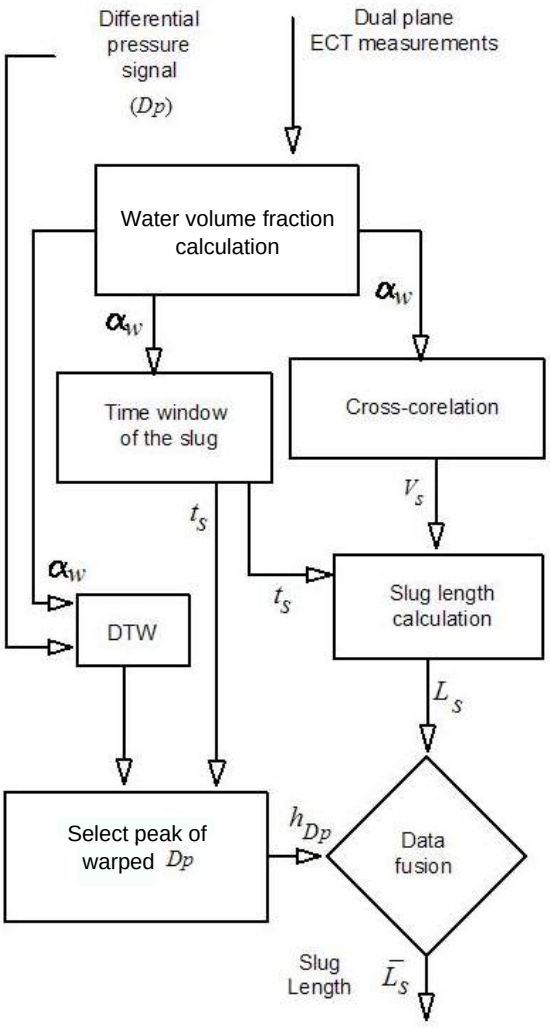

Figure 7.6: Structure of calculation of slug length with DTW of differential pressure signal,Dp and water fraction signal, α_w, with cooperative data fusion.

corresponds to the first 100s of test 2 are given in the Figure 7.7. Calculated liquid slug length (L_s) and magnitude of the D_p peak, which lies within the corresponding slug body (h_{Dp}) is also then studied with respect to both the time slots and their respective amplitudes. Then the liquid slug lengths and corresponding pressure peaks of each 23 slugs observed were plotted against each other as illustrated in Figure 7.8.

It can be seen clearly in Figure 7.7 that liquid slug length is proportional to the h_{Dp} value. This can be clearly observed in h_{Dp} vs α_w plot in Figure 7.8. Though quadratic regression line evidences the proportionality, some data points can be seen resting far away from the regression

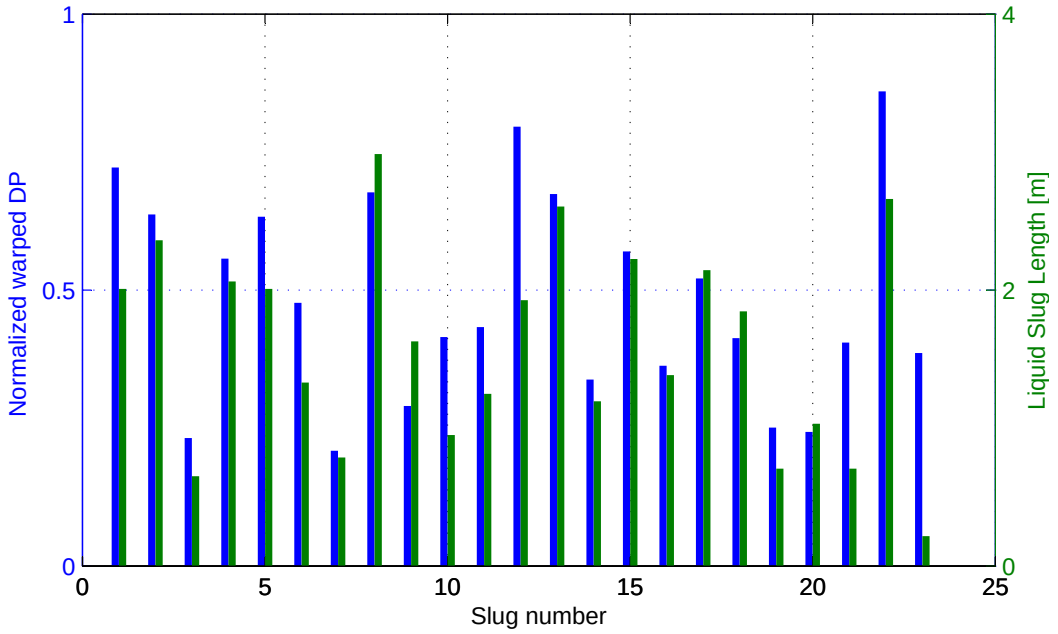

Figure 7.7: Slug lengths,L_s, as calculated using slug velocities,Us from test 2 data and corresponding warped differential pressure,Dp.

curve while others are scattered around. Linear data fitting also look reasonable, if the studied slug length range is considered, though there are some disagreements with quadratic fit for slugs shorter than 0.5m and longer than 2.5m. Each slug was individually checked with the pressure peak, but the data show no evidence to consider any of them as outliers. Slugs around 2m lengths lie much away from the regression lines as shown in the Figure 7.8. To have a clearer picture while handling uncertainty involved, slug lengths and corresponding pressure peaks were classified into 6 different groups as given in Table 7.2. The mean values of h_{Dp} and their standard deviations are given in the other columns for the given conditions of test 1 and 2.

Analysis was repeated with other data sets under the given experimental condition in Table7.1. Here the study of the slug lengths and corresponding pressure peaks were done with the help of high-speed camera images for further confirmation.

As illustrated in Figure 7.10, sequence of images are captured from high speed camera for the observation time period, T_{ob}. 600^{th} pixel column of each image is picked as shown in the figure. Since the time taken to move from one image to other is $1/f_{cap}$s, it is applied for these

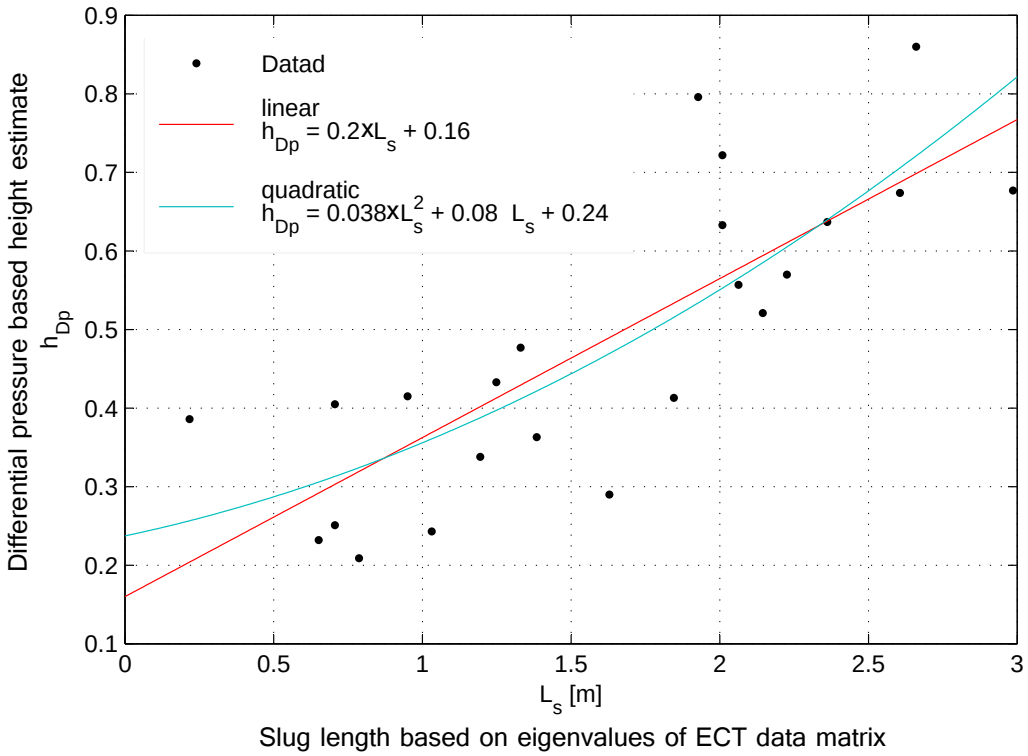

Figure 7.8: Variation of normalised pressure peak (h_{Dp}) with increasing Slug lengths under the experimental conditions of test 2

Table 7.2: Pressure Peak variation under different slug lengths.

	Normalised Pressure Peak $\left(\bar{h}_{Dp} \pm STD_{h_{Dp}}\right)$	
Slug Length m	Test 1	Test 2
0-0.5		0.38 ± 0.0
0.5-1	0.31 ± 0.11	0.30 ± 0.09
1-1.5	0.41 ± 0.0	0.37 ± 0.09
1.5-2	0.55 ± 0.14	0.49 ± 0.2
2-2.5	0.62 ± 0.15	0.61 ± 0.07
2.5-3	0.78 ± 0.21	0.73 ± 0.10

pixel columns as well. Hence, by sequentially stacking those selected pixel columns, an image, which represents the flow variations with respect to time, can be constructed.

Images were captured at $f_{cap} = 50$fps for the construction of the image in Figure 7.11 a). Hence, $5 \times f_{cap}$=250 number of images are needed for a $5s$ view of Figure 7.11 a). For the same

period of observation, the corresponding Dp signal train was identified by DTW technique. The process was repeated for every $5s$ time slot containing the slug images.

Figure 7.11 shows the comparison of time series signals of image data and α_w data of test 5. Signals from the two modalities indicated a very good agreement with slug flow measurements. The waves appeared at $13s$ and $23s$ of the Figure 7.11 a) also visible in the Figure 7.11 b) as well. The warped Dp does not exhibit any sign of dynamic at those waves. Slug encircled on both Figure 7.11 a) and b), is identified as a possible outlier as marked in black circle in corresponding L_s vs h_{Dp} plot shown in Figure 7.9.

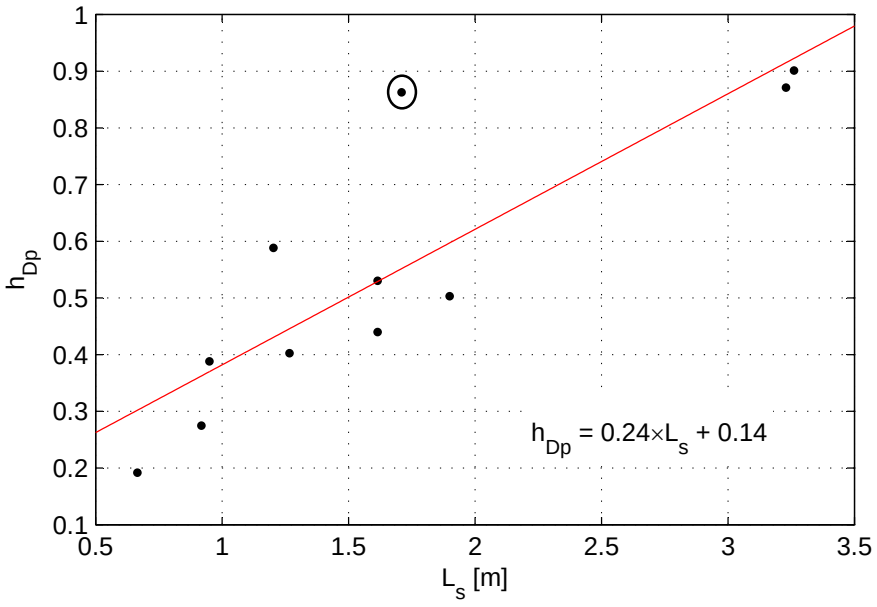

Figure 7.9: Variation of normalised pressure peak (h_{Dp}) with increasing slug lengths under the experimental conditions of test 1. Circled data point looks like an outlier

This is mainly due to a larger pressure peak compared to its relatively small slug body length (L_s). It can be observed in both Figures 7.11 a) and b) that there are two slugs close to each other. It is hard to consider these two as a one slug. This portion of the fluid formation seems to be not a single slug, but a collusion of one or more slugs. These two slugs are too close to each other for the warped signal processing to differentiate. The prominent pressure changes can be observed in the selections (in the elliptical ring) shown in Figure 7.11 b). By considering only the pressure information, this special case can be explained as a one longer slug. However, image information and ECT based α_w calculation indicates the existence of two slugs located closer to each other.

Similar events were observed in the other experimental data (test 3, 4 and 6) as well. Regression of α_w vs h_{Dp} of each experiment was calculated excluding such misleading slug information. Results correspond to each of these experiments are shown in Figures 7.12.

Slopes and intercept of the regression lines are not varying much with increased inlet air

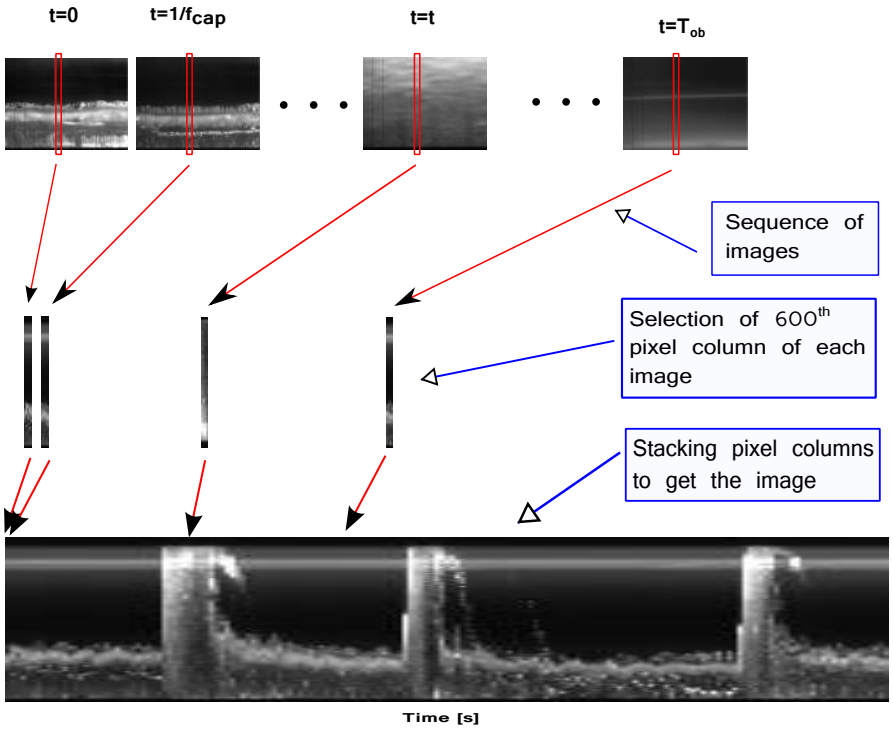

Figure 7.10: Procedure followed to get time series representation of the camera image information

flow rates. It looks like that slug units with structures different from the rest, are lying away from the regression line. This fact indicates that they are outliers. Waves, which do not develop to obstruct the air flow as liquid slug, do not get any significant pressure increase within it. However, it always produces a significant pressure build up even for a very short slug as shown in Figure 7.11.

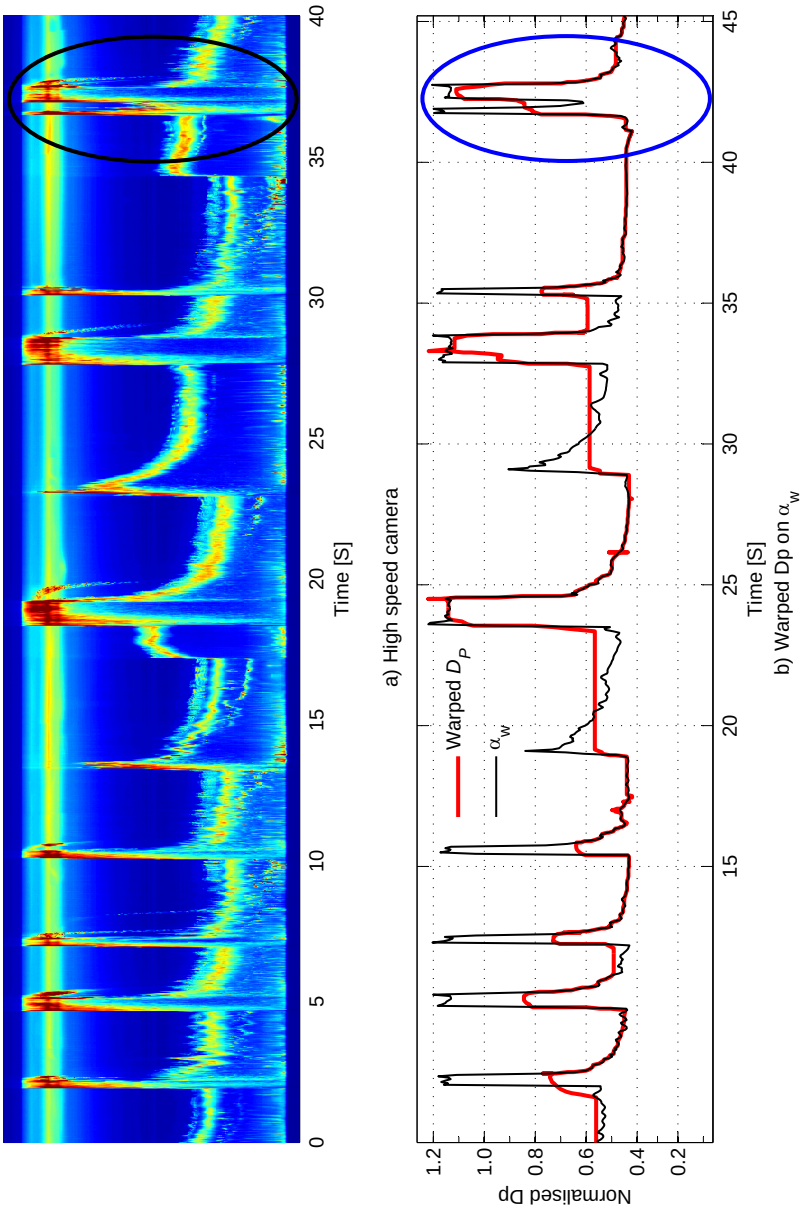

Figure 7.11: Closely overlapping signal trains from time warped signal, Dp and high-speed camera images. Although the flow discussed here is horizontal, the view is shown vertically to enable details of signal train and high speed images visible

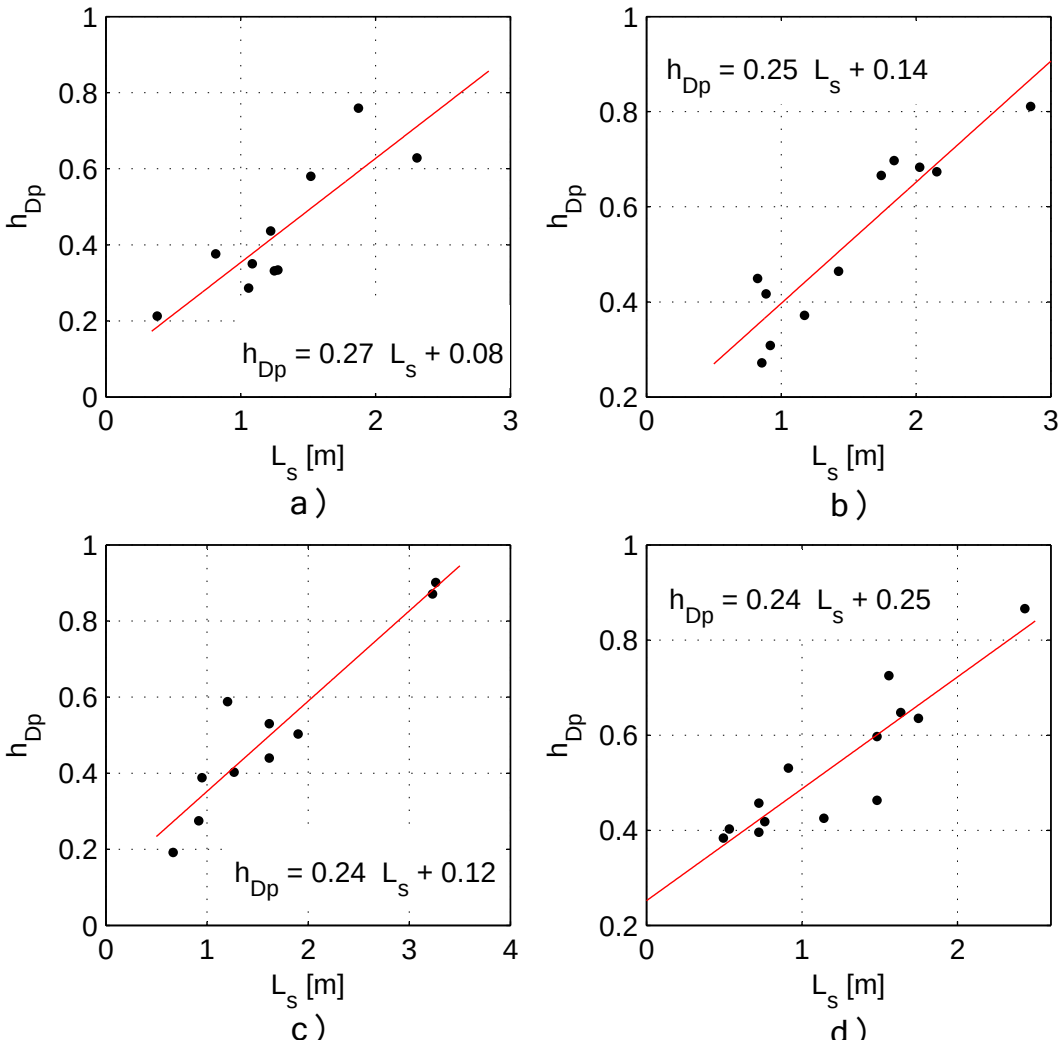

Figure 7.12: Relationship with normalised pressure peak (h_{Dp}) with slug lengths, L_s under the experimental conditions of a) test 3 b) test 4 c) test 5 d) test 6 respectively

Chapter 8

Main conclusions and future works

8.1 Main conclusions

1 Capacitance measurements form 12 electrode sensor were successfully used in interface level estimation of two phase flows, though uncertainties varies little in different phase combinations of air, water and oil. However, results with 6 electrode sensor give around 9% of error uncertainty for air-water two phase flows. With other flow combinations, they are much less than 9%. This is acceptable for most of the multiphase flow applications. 4 electrodes sensor is also working well in estimations. Uncertainty involved is sometime lower than 5 electrode asymmetric sensor selection. This is mainly due to inability of the sensing electrodes to cover much of the interface area. But, the possibility of using this arrangement with separately trained ANN gives an opportunity to get the estimations when some electrodes fails and ECT images are not usable.

Effect of higher permittivity of water has increased the estimation uncertainty, when number of electrodes of the sensor is lowered this can be seen clearly. But, even with the reduced number electrodes better estimation can be achieved by selecting a better ANN architecture. Most of the ANN Architectures used in these studies tried to preserve the hidden architecture with the view of comparison of estimation time. But, in practice with different flow components along with water, this higher permittivity effect would be significant, especially with wetted inner pipe wall and water droplets in air or oil phases.

ECT systems with reduced number of electrodes can be used for estimating interfaces of layered flows with acceptable estimation uncertainties. For air-water, 6 electrodes sensor works well and further reduction of sensor electrode would show significant loss in the accuracy. But, with air-oil two phases even 4, 5 electrode sensors can also be used with acceptable uncertainty. ANN based inferential method with 4 or 5 electrode sensors gives faster and timelier responses, which could be implemented in a pipe separator.

In practice, ANN models used in the estimations should be verified frequently to maintain reliable estimations in operation.

2 Tomogram of stratified layered dynamic flows of air-oil and GRM measurements shows somewhat higher levels than the corresponding camera image based measurements. Both

techniques are affected by the wetting of the pipe wall. It can be relatively large with ECT technique.

3 Slug flow parameters for two phase air-water flows such as slug frequency, slug length, slug velocity, liquid film thickness can be successfully estimated using ECT, ERT measurements. Average of inter electrode voltage measurements time series signal could be used to extract the flow parameters, even though ERT cannot be used when there is no conductive media covering all electrodes. Some high-speed camera images are used for verifications. Differential pressure signals correspond to some measurements proved the reliability of slug frequencies. Trends in slug parameters variations against superficial air velocities are similar with the literature. Cross-sectional information especially near the pipe wall is indicating some dynamic there. Due to the lower measurement frequencies, it is difficult to make any conclusion.

4 Same cross-correlation algorithm used in the slug flow studies could be used in the identification of flow reversing. This lab scale experimental study show that simultaneous measurements of flow velocities, volume ratios and flow direction are possible with ECTm data. Selection of the correlation window is a critical factor here.

5 Dynamic time warping technique (DTW) was used to align two signal, capacitance, and pressure with the slug. Here aligned signals of pressure and volume fraction, shows that possibility of identifying liquid slug with both signals. This cooperative data fusion technique provides better estimation of the liquid slug length. Linear relationship observed between normalised pressure peak and liquid slug length will be the easiest way of slug length estimation.

6 ECT Measurement matrix properties were used successfully in the annular flow stratified flow and slug flow identifications. Relationship between leading eigenvalue and the liquid volume fraction was successfully tested and verified. For the water fractions lower than 0.2, this relationship does not work well, but for other ranges, it worked well. Second and third eigenvalues have opposite signs for layered flows and agree with the literature. But, for the annular flows, it is very difficult to judge the signs of the second and third eigenvalues with the limited measurements.

8.2 Future works

1 Arrangements should be made to capture all measurements simultaneously, especially pressure parameters with ECT and ERT. Therefore, the fusion of the various signals from different measurements is possible and would yield better results. The synchronised set of data will provide better fusion results and will improve the quality of results based on comparative analysis of the fused and individual data. A high-speed camera with a larger memory capacity will also be helpful in the measurement verifications. A series of pressure sensors along the pipe flow directions should be placed. Then the measurements

from those sensors can be used in the comparison of slug flow parameters estimated using ECTm and ERTm.

2 Pressure fluctuations and their effects on permittivity and hence tomographic image constructions should be studied separately. This would be help to gather more and better pixel information.

3 How wetting of pipe inner wall affects the ECT and GRM measurements should be studied along with CFD model. Fusion of model data and measurement data would be helpful to correct the interface estimation errors.

4 Properties of matrices containing raw data from ECT/ERT of different flow patterns should be studied further. Main focus should be on the annular flows and relationship between second and third leading eigenvalues.

5 Data capturing rates of ECT and ERT should also be improved, so that studies can be extended to extract more information and hence improved tomometrical results with cross-correlations.

6 Investigating the system in real time with increased number of sensor modalities will give more information on different system parameters as well as flow phenomena.

7 For process technical solutions for measurement and control of multiphase flow a solution based on multimodal sensor data fusion as well as fusion of conventional control algorithms with AI-techniques (such as ANN, Fuzzy, Support Vector Machines) would be advantageous, as solutions based on mechanical models alone may be inadequate to describe all the features encountered in different flow regimes.

Bibliography

Al-Lababidi, S. (2006), Multiphase Flow Measurement in the Slug Regime Using Ultrasonic Measurements Techniques and Slug Closure Model, PhD thesis, Cranfield University, United Kingdom.

Alme, K. J. (2007), Material distribution and interface detection using EIT, PhD thesis, Telemark University College and NTNU, Norway.

Alme, K.-J. & Mylvaganam, S. (2006), 'Electrical capacitance tomography amp:sensor models, design, simulations, and experimental verification', *Sensors Journal, IEEE* **6**(5), 1256–1266.

Azzopardi, B. J. (2006), 'Multiphase flow', *Chemical engineering and chemical proces technology* **1**.

Beck, M. S. & Williams, R. A. (1996), 'Process tomography: a european innovation and its applications', *Measurement Science and Technology* **7**, 215–224.

Bennett, M., Luke, S. P., Jia, X., West, R. & Williams, R. (1999), Analysis and flow regime identification of bubble column dynamics, *in* 'at 1st World Congress on Industrial Process Tomography', Buxton, Greater Manchter, UK.

Bertani, C., Salve, M. D., Malandrone, M., Monni, G. & Panella, B. (2010), State of art and selection of techniques in multiphase flow measurement, PhD thesis, Italian National agency for new technologies, Energy and sustainable economic development, Turin.

Bratland, O. (2010), *Pipeflow 2, Multi-phase flow assurance*.

Bukhari, S. F. A. & Yang, W. (2006), 'Multi-interface level sensors and new development in monitoring and control of oil separators', *Sensors* **6**(4), 380–389.

Byars, M. (2001), Developments in electrical capacitance tomography, *in* 'at 2nd World Congress on Industrial Process Tomography', Hannover, Germany.

Cai, Y., Wang, H. W., Hong, T. & Jepson, W. P. (1999), Slug frequency and length inclined large diameter multiphase pipeline, *in* 'Proceedings of flow and heat transfer flow and heat transfer'.

Cheney, M., Isaacson, D. & Newell, J. (1999), 'Electrical impedance tomography', *SIAM Review* **41**(1), 85–101.
URL: *http://epubs.siam.org/doi/abs/10.1137/S0036144598333613*

Cook, M. & Behnia, M. (2000), 'Slug length prediction in near horizontal gas-liquid intermittent flow', *Chemical Engineering Science* **55**(4188), 2009–2018.

Corneliussen, S., Couput, J. P., Dahl, E., Dykesteen, E., Frøysa, K. E., Malde, E., Moestue, H., Moksnes, P., Scheers, L. & Tunheim, H. (2005), *Handbook of Multiphase Flow Metering*, Norwegian Society for Oil and Gas Measurement (NFOGM).

Daily, W., Ramirez, A., Newmark, R., George, V. & Randall, J. (2000), Imaging uxo using electrical impedance tomography, *in* 'Proceedings of SAGEEP', Washington D.C., p. pp793.

Datta, U. (2007), Multimodal Measurements in Dilute Phase Pneumatic Conveying Systems, PhD thesis, Telemark University College and NTNU, Norway.

Dukler, A. E. & Hubbard, M. G. (1975), 'A model for gas-liquid slug flow in horizontal and near horizontal tubes', *Ind. Eng. chem.* **14**(4).

Dyakowski, T. & Jaworski, A. J. (2003), 'Non-invasive process imaging-principles and applications of industrial process tomography', *Chemical Engineering Technology* **26**(6), 697–706.

Dyakowski, T., Jeanmeure, L. F. & Jaworski, A. J. (2000), 'Applications of electrical tomography for gas–solids and liquid–solids flows — a review', *Powder Technology* **112**(3), 174 – 192.

Fang, W. & Cumberbatch, E. (2005), 'Matrix properties of data from electrical capacitance tomography', *Journal of engineerin mathematics* **51**(.), 127–146.

Havre, K., Stornes, K. O. & Stray, H. (2000), *Taming slug flow in pipelines*, 3rd edn, ABB review.

Haykin, S. (2008), *Neural Networks and Learning Machines*, 3rd edn, New Jersey: Prentice Hall.

Hjertaker, B. T., Johansen, G. A. & Jackson, P. (2001*a*), 'Level measurement and control strategies for subsea separators', *Journal of Electrcal Imaging* **10**(3), 679–689.

Hjertaker, B. T., Johansen, G. A. & Jackson, P. (2001*b*), 'Recent developments in hydrocarbon separator interface imaging', *Proc. of SPIE* (4188), 81–92.

Isaksen, ., Dico, A. S. & Hammer, E. A. (1994), 'A capacitance-based tomography system for interface measurement in separation vessels', *Meas. Sci. Technol* **5**(1), 1262–1271.

Ismail, I., Gamio, J., Bukhari, S. & Yang, W. (2005), 'Tomography for multi-phase flow measurement in the oil industry', *Flow Measurement and Instrumentation* **16**(2–3), 145 – 155.

Ismail, I., Gamio, J., Bukhari, S. & Yang, W. (2011), 'Experimental investigation of air-oil slug flow using capacitance probes, hot-film anemometer and image processing', *International Journal of Multiphase Flow* **37**, 876–887.

ITS (2005), *ITS Toolsuite, User's manuel*, Industrial Tomography Systems Ltd, Manchester, UK.

Johansen, G. A., MERIC, I., Maad, R., Bruvik, E. M., Hjertaker, B. T. & Sætre, C. (2014), Non-destructive monitoring of multiphase hydrocarbon flow by highspeed gamma-ray tomography, *in* '11th European Conference on Non-Destructive Testing (ECNDT 2014)', Prague, Czech Republic, pp. 1022–1029.

Kang, C., Jepson, W. P. & Gopal, M. (1999), 'Effect of drag-reducting agent on slug characteristics in multiphase flow in inclined pipes', *Journal of Energy Resources Technology* **121**.

Keogh, E. J. & Pazzani, M. J. (2000), 'Scaling up dynamic time warping for datamining applications', *ACM* .

Kumara, W. A. S. (2010), An Experiimentall Study of Oiill-Water Fllow iin Piipes, PhD thesis, Telemark University College and NTNU, Norway.

Long, T. M. (2006), An on-line velocity flow profiling system using Electrical resistance tomography, PhD thesis, University of Cape Town, South Africa.

Ma, Y., Zheng, Z., an Xu, L., Liu, X. & Wu, Y. (2001), 'Application of electrical resistance tomography system to monitor gas/liquid two-phase flow in a horizontal pipe', *Flow Measurement and Instrumentation* **12**, 259–265.

Marsshdeh, Q. (2006), *Advances in electrical capacitance tomography*, Ohiyo State University, PhD thesis.

Matlab (2002), *Neural network toolbox*, The Mathworks Inc., Natick, MA.

Moore, M. (2012), The use of wavelets for determining wing flexure in airborne gps multi-antenna attitude determination systems, *in* 'Proceedings of the 15th International Technical Meeting of the Satellite Division of The Institute of Navigation (ION GPS 2002)', Portland, OR, pp. 1022–1029.

Müller, M. (2007), *Information Retrieval for Music and Motion*, 3rd edn, Springer-Verlag New York, ISBN: 978-3-540-74047-6.

Niedostatkiewicz, M., J.Tejchman, Z.Chaniecki & K.Grudzien (2009), 'Determination of bulk solid concentration changes during granular flow in a model silo with ect sensors', *Chemical Engineering Science* **64**(20-30).

Norwegion radiation protection authority, N. (2005), 'Act and regulations on radiation protection and use of radiation', *østeras:NRPA* .
URL: *www.nrpa.no/dav/6cb7606703.pdf*

Perez, H. V. (2007), Gas-liquid two-phase flow in inclined pipes, PhD thesis, University of Nottingham, United Kingdom.

Pradeep, C., Ru, Y. & Mylvaganam, S. (2012), 'Reverse flow alarm activation using electrical capacitance tomometric (ectm) correlation', *IEEE Sensor Application Symposium* pp. 228–232.

Pradeep, C., Yan, R., Vestøl, S., Melaaen, M. C. & Mylvaganam, S. (2014), 'Electrical capacitance tomography (ect) and gamma radiation meter for comparison with and validation and tuning of computational fluid dynamics (cfd) modeling of multiphase flow', *Measurement Science and Technology* **25**, 1–8.

Primrose, K. M., Qiu, C. & Bolton, G. T. (2010), Visualsation and measurement of 3 phase (air water oil) flow and 2 phase flow (sand water) with electrical tomography, *in* 'at 6th World Congress on Industrial Process Tomography', Beijing, China.

PTL (2009), *Fundametals of ECT*, Process Tomography Limited.

PTL, P. T. L. (2008), 'Developments in electrical capacitance tomography', *Electrical capacitance tomography system operation manual* **1**(6).

Randall, E. W., Long, T. & Sutherland, A. P. N. (2008), *The UCT electrical resistance tomography Instrument and its applications*, The Southern African Institute of Mining and Metallurgy.

Randall, E. W., Wilkinson, A. J., Long, T. M. & Southerland, A. (2004), A high speed current pulse electrical resistance tomography system for dynamic process monitoring, *in* 'Proceedings of the 7th Biennial ASME Engineering Systems Design and Analysis', Manchester, UK.

Rautenbach, C., Melaaen, M. & Halvorsen, B. (2011), 'Investigating the influence of fines in fludized bed reactors using 3d ect images', *Engineering science* **70**, 141–151.

Rautenbach, C., Mudde, R. F., Yang, X., Melaaen, M. C. & Halvorsen, B. M. (2012), 'A comparative study between electrical capacitance tomography and time-resolved x-ray tomography', *Flow measurement and instrumentation* **–**, 0–0.

Reinecke, N., Petritsch, G., Boddem, M. & Mewes, D. (1988), 'Tomographic imaging of the phase distribution in two-phase slug flow', *International Journal of Multiphase Flow* **24**(4), 617–634.

Rogero, E. C. (2009), Experimental investigation of developing plug and slug flows, PhD thesis, Munchen Technical University, Germany.

Ru, Y., Pradeep, C. & Mylvaganam, S. (2010), Artificial neural networks for ect based interface detection in separators, *in* 'at 6th World Congress on Industrial Process Tomography', Beijing, China.

Ru, Y., Pradeep, C. & Mylvaganam, S. (2011), 'Neural networks in electrical capacitance tomography (ect)-based interface detection', *Measurement Science and Technology* **22**(10), 104006.
URL: *http://stacks.iop.org/0957-0233/22/i=10/a=104006*

Ruder, Z., Hanratty, P. J. & Hanratty, T. J. (1989), 'Necessary condition for the existance of stable slugs', *Int Journal of Multtphase dlow* **15**, 209–226.

Sakoe, H. & Chiba, S. (1978), 'Dynamic programming algorithm optimization for spoken word recognition', *IEEE Transactions on Acoustic, Speech and Signal Processing* **26**(1), 43–49.

Sankowski, D., Zain, R. M. & Mosorov, V. (2006), Image fusion for dual tomography, *in* 'Perspective Technologies and Methods in MEMS Design, 2006. MEMSTECH 2006. Proceedings of the 2nd International Conference on', pp. 75–78.

Strang, G. (2009), *Introduction to Linear Algebra*, 4th edn, Wellesley: Cambridge press.

Vestøl, S. (2013), Detailed measurementsof gas/liquid flow with lowliquid fractions in horizontaland near horizontal pipes, PhD thesis, Norwegian University of Science and Technology, Department of Energy and Process Engineering.

Vestøl, S. & Melaaen, M. C. (2006), Gamma and piv measurements in laboratory model of unprocessed gas flow, *in* 'at 5th International symposium on measurement techniques for multiphase flows', Macau, China.

Vuurpiji, L. (1998), Platforms for artificial neural networks Neurosimulators and Performance prediction of MIMD-Parallel Systems, PhD thesis, University of Nijmegen, Netherlands.

Wang, F., Marashdeh, Q., Fan, L. S. & williams, R. A. (2009), *Advances in chemical engineering* **37**, 179–222.

Wang, H. X. & Zhang, L. F. (2009), 'Identification of two phase flow regimes based on support vector machine and electrical capacitance tomography', *Measurement Science and Technology* **20**.

Wu, Z., McCann, H., Davis, L. E., Hu, J., Fontes, A. & Xie, C. G. (2009), 'Microwave-tomographic system for oil- and gas-multiphase-flow imaging', *Measurement Science and Technology* **20**(10), 104026.
URL: *http://stacks.iop.org/0957-0233/20/i=10/a=104026*

Yang, W. (2010), 'Design of electrical capacitance tomography sensors', *Measurement Science and Technology* **21**.

Yang, W., Chondronasios, A., Nattrass, S., Nguyen, V., Betting, M., Ismail, I. & McCann, H. (2004), 'Adaptive calibration of a capacitance tomography system for imaging water droplet distribution', *Flow Measurement and Instrumentation* **15**(5–6), 249 – 258.
URL: *http://www.sciencedirect.com/science/article/pii/S0955598604000433*

Yang, W. Q. & Peng, L. H. (2003), 'Image reconstruction algorithms for electrical capacitance tomography', *Meas. Sci. Technol* **14**(1), R1–R13.

Zorgani, E., Al-Awadi, H. & Yan, W. (2010), Ect application in heavy oil multi-phase flow system: Part 1 static mesurements, *in* 'at 6th World Congress on Industrial Process Tomography', Beijing, China.

PART II

Published Articles

Paper 4

Multimodal Tomometry for Slug Detection in two Phase Flow

This paper was also presented as an oral presentation at the 6th International Symposium on Process Tomography (ISPT) in Cape Town, South Africa in March 2012. The paper was also published in the conference proceedings of International Symposium on Process Tomography 2012 (ISBN: 978-0-620-53039-2, March 2012, pp:OR11)

Multimodal Tomometry for Slug Detection in two Phase Flow

Chaminda Pradeep[1], Yan Ru[1] and Saba Mylvaganam[1, 2]

[1]Telemark University College (TUC)
Faculty of Technology, Department of Electrical Engineering, Information Technology and Cybernetics, Porsgrunn,Norway,

[2]Telemark Technological R&D Institute, Kjølnes Ring 30, N-3918 Porsgrunn, Norway
Email: saba.mylvaganam@hit.no

ABSTRACT

Electrical Capacitance and Resistance Tomometric (ECTm/ ERTm) approaches are attractive for measurement and control applications in the process industries. By using the time series of raw resistance and capacitance values R(i,j,t) and C(i,j,t) (i=1, …, N_R, j = 1, 2, …, N_R and i ≠ j for ERT modules with N_R electrodes; i=1, …, N_C, j = 1, 2, …, N_C and i ≠ j for ECT modules with N_C electrodes), it is shown in this paper (with N_R=16,N_C=12) how the intermittent occurrence of slugs in a liquid/gas two phase flow can be detected using the time series data consisting of the measured resistances and capacitances R(i,j,t) and C(i,j,t). In a pipe transporting oil and gas, the slugs can be characterized by their sizes, occurring instants and frequencies. The signal processing employed to estimate these parameters associated with the slugs is based on the analysis of the pulse generated from the ECT/ERT module, both in time and frequency domains. Some measurements are also performed using high speed camera, thus making this effort multimodal. Due to the very much reduced estimation times involved in this process as compared to tomographic image processing, this tomometric method has many advantages in real time measurement and control applications. Signal processing of the volume ratio data of tomography systems and image analysis of high speed camera images can be done to extract various slug parameters. Slug length, velocity and frequency in a slightly inclined upward two phase water/air flow are estimated using fusion of data from the multimodal system. The results obtained are compared to verify the various parameters estimated using different modalities.

Keywords: ERTm, Slug parameters, oil and gas flow, cross-correlation, power spectral density, ECT, ERT

1 MOTIVATION

Electrical Capacitance/ Resistance Tomography (ECT/ERT) is gaining ground in industrial multiphase flow metering (Ismail et al 2005). Some key industrial actors in the oil and gas industries have ECT/ERT systems in their test facilities. In conjunction with multiphase flow metering, the identification of the regions of different phases and hence the flow regimes, is an important application of ECT/ERT. This paper focuses on the detection of slugs very often found in multiphase flow using ECT/ERT. When the slug passes the sensor head containing the resistance/capacitance sensors, a characteristic pulse is formed showing the spatial variations of resistivity or permittivity, given by the raw capacitance/resistance values *C*(*i,j,t*) and *R(i,j,,t)*. Many parameters characterizing the slug can be obtained by studying the characteristic pulse associated with the slug in frequency and time domains.

Slugs in multi-phase flow can lead to hazardous situations involving pressure build-up and blow out as was the case on Deepwater Horizon platform in the Mexican Gulf. Timely detection of slug formation can help the operators in preventing such disasters. Tomometric methods may well be suited for such applications. From raw resistance/capacitance data, sensor level fusion can be performed using inferential methods involving such as fuzzy-logic or neural network based algorithms. Fusion at a higher level leading to features easily assignable to slugs can also be advantageous, but this might need longer time to process. This paper deals with sensor level fusion and addresses some aspects of feature level fusion using inferential methods.

2 MULTIPHASE FLOW FACILITY

A schematic diagram of the multiphase flow facility used for the generation of slug flow is shown in Figure 1. The test section consists of 15m long pipe of 56mm internal diameter with flow meters to monitor water and air flow at the inlet and some pressure and temperature sensors. The ECT/ERT systems are placed about 13

m from the inlet. Pipe inclination is maintained at +1 degree with the horizontal. The outlet pressure is atmospheric due to the storing of the fluids at the outlet in an open tank.

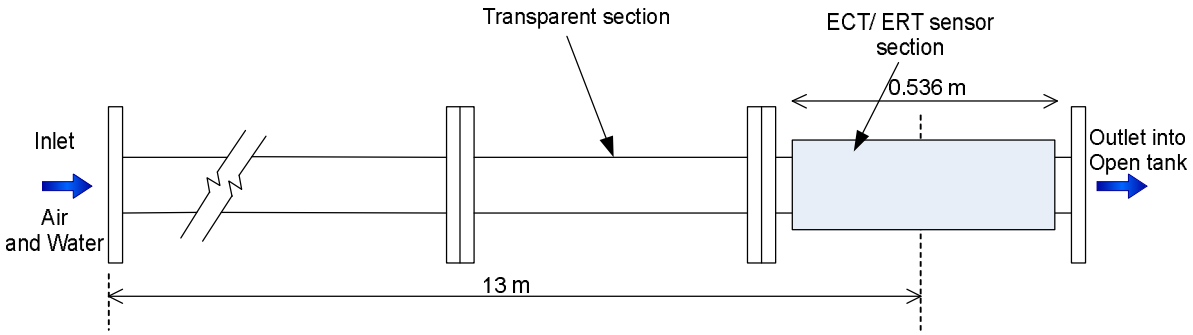

Figure 1. Schematic diagram of the test section with ECT/ERT system

Inter-electrode capacitance and resistance measurements were recorded separately using ECT and ERT systems with the flow loop running under a selected set of inlet conditions. The ECT system used for these experiments is PTL300E. It is capable of measuring up to 100 data frames per second. The current pulse ERT system (Randall et al 2004) developed by the UCT (University of Cape Town) was used and resistance data were acquired at 37 frames per second in the experiments.

A MotionPRO X Digital camera is used to obtain detailed data regarding slug characteristics such as slug frequency, slug lengths and the height of the liquid film. The capture rate used was 40 frames per second.

3 EXPERIMENTAL PROCEDURE AND DATA ANALYSIS

In a typical ERT application, the first set of results are the raw resistance, as well known comprising of $(N_R(N_R\text{-}3)/2)$ measurements for an ERT system with N_R-electrodes using the pulsed current mode of excitation (Daily et al 2000). A schematic of the ERT module is shown in Figure 2. These values are usually processed using rather time consuming algorithms to generate images, called tomograms in the context of process tomography. By focusing on the ERT signal train (shown in Figure 3) obtained during the transit of the slug past the ERT system, and employing signal processing of the pulse generated at the ERT electrodes, we can estimate various parameters associated with this particular slug.

Experiments were performed maintaining volumetric flow rate of water at the inlet of the testing unit at 30kg/min (hence superficial velocity 0.2m/s) while the air flow rate was increased from 0.05 kg/min to 0.5 kg/min in 0.05 kg/min steps (superficial velocity from 0.28m/s to 2.78 m/s). Inclination of 56 mm diameter test pipe was +1◦ to the horizontal plane. Separate ERT, ECT sensors and a high speed camera were also used as indicated in Figure 2.

3.1 Slug velocity

Time series of volume ratio data obtained from twin plane capacitance and resistance sensors were cross-correlated to calculate slug velocity. Figure 2 illustrates how both sensor planes capture the slug flow, assumed to have not undergone any change considerably due to the short distances between the twin planes for ERT and ECT sensors. The time delays between the two signals from the two sets of ERT and ECT sensors are calculated using cross-correlation of signals (Ahmed 2011) as given in equation (1). If $S_{pl_1}(t)$ and $S_{pl_2}(t+\tau)$ are the signals at the sensor planes 1 and 2 at time instant t and $t+\tau$ respectively, then the typical cross-correlation function $\rho_{S_{pl_1}(t),S_{pl_2}(t+\tau)}(\tau)$ is defined by the following equation (Datta 2007):

$$\rho_{S_{pl_1}S_{pl_2}} = \lim_{T\to\infty}\frac{1}{T}\int_0^T S_{pl_1}(t)S_{pl_2}(t-\tau)dt \qquad (1)$$

The time delay τ_{max} corresponding to the maximum value of cross-correlation function gives the transit time of the flow between the two sensors. From the estimate of cross-correlation as given in equation (1), the time delay τ_{max} can be found by finding the correlation peak. Using the time delay τ_{max} and distance L between the two sensor planes, the axial slug velocity, V_s can be evaluated as:

$$V_s = \frac{L}{\tau_{max}} \tag{2}$$

Both ECT and ERT measurements were used in the estimation of the slug velocity. Measured row capacitance and resistance measurements were correlated separately. Flowan software developed by Process Tomography Limited was used to estimate the slug velocities for verifying the results. Flowan software uses pixel correlation for velocity estimation.

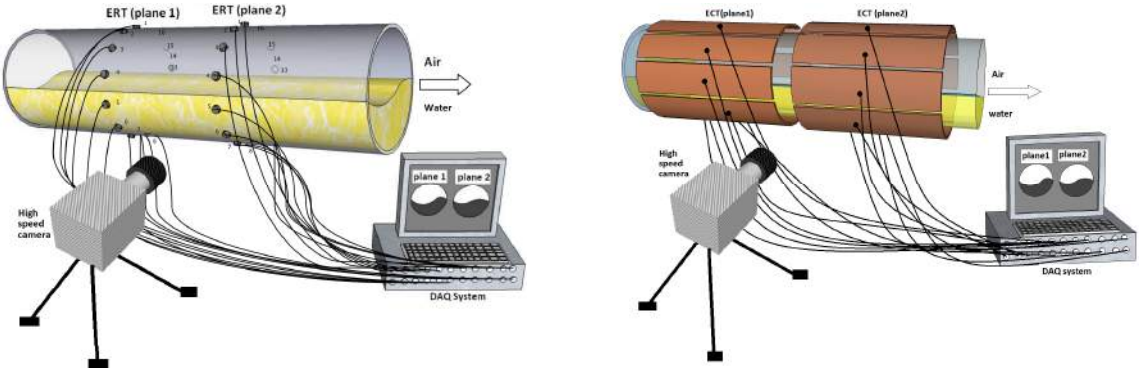

Figure 2. Resistance and Capacitance sensors on the periphery of a pipe distributed in two different planes with water and air delivering capacitance values *C(i,j,t)* with *i= 1, 2, ..12, j=1, 2, …12* and resistance values *R(i,j,t)* with *i= 1, 2, ..16, j=1, 2, …16* in this case

3.2 Slug frequency

Counting the number of slugs moving past these two sets of sensors placed in the two different planes pl_1 and pl_2 within the observation period can be used to calculate the slug frequency as given in equation (3). A threshold value has to be defined to decide the existence of slug (Al-Lababidi 2006).

$$f_s = \frac{n_s}{T} \tag{3}$$

Where f_s is the slug frequency, n_s is the number of slugs passed during the observation period T .
Average of the ECT/ERT measurement signals was used. The averaging process helps to identify the boundaries of the slug bodies. Images captured from the high speed camera were also run frame by frame to count the number of slugs to verify the results.

3.3 Mean Slug body length

As indicated in Figure 3, time window t_s associated with the slug body is calculated. Then with the estimated slug flow velocity, each slug length L_s can be calculated.

$$L_s = t_s V_s \tag{4}$$

The threshold selected in the algorithm used in the slug frequency calculation is used here to find the time window of the slug body. Typical slug front and tail images produced by the High speed camera, are shown in Figure 4. ECT and ERT signals used in the analysis of slug frequency are shown here to see some clear boundaries of slug fronts and tails.

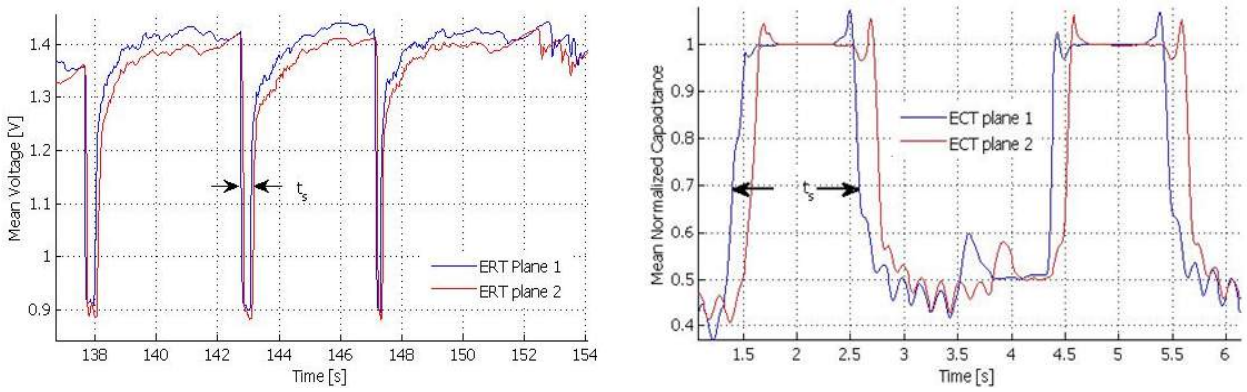

Figure 3. Typical Slug pulse as obtained from ERT and ECT time sequences

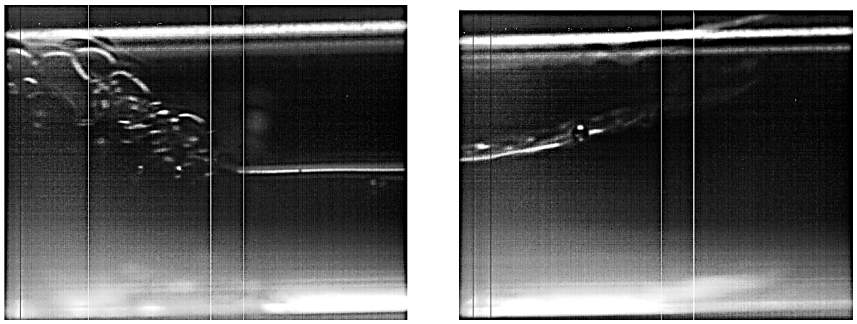

(a) (b)

Figure 4. Images of slug front (a) and tail (b). Bottom part of the slug is water and top part air.

4 RESULTS

Estimates of slug velocity, slug frequency and slug length are given in Figures 5, 6 and 7. It can be seen in Figure 5, that all three curves show an increase in slug velocities with increasing superficial gas velocities. Compared to the ECT and Flowan based calculations, ERT measurements show an increase of slug velocity about 0.1m/s at 0.8 m/s superficial gas velocity and decrease of about 0.13 m/s at superficial gas velocity 1.1 m/s. At superficial air velocity 2.2 m/s the highest velocity difference of 0.35 m/s is observed.
To see whether these estimation differences are due to different data capturing rates of ECT and ERT systems, uncertainty of the slug velocities due to the data capturing rate of each ECT and ERT systems were tested. There is $\pm$ 0.005 s uncertainty to the time delay, τ_{max} in the ECT, since its data capturing rate is 100 frames per seconds. The corresponding uncertainty associated with ERT is $\pm$ 0.013 s.

When τ_{max} increases, slug flow velocity decreases and hence uncertainties of the calculated slug velocities also decrease. When the time delay τ_{max} decreases, slug velocity and uncertainty increase. Figure 8 shows the uncertainty increase in the velocity range considered of this work. This may be one of the reasons for higher velocity estimates resulting from ERT data.

Slug frequency decreases when the superficial gas velocity increases as explained by Kang et al (1999). Results show slight decrease in slug frequency. It can be easily seen that results based on the image data are showing higher slug frequencies compared to the ECT and ERT based calculations even though they follow similar trends. An offset of about +0.05 Hz is observed compared to the other ECT/ERT based calculations. Limitations in the memory storages in the camera restrict the possibilities of capturing data to 40s. The increase of one slug increases the slug frequency by 0.025 Hz due to the limited observation time period. The ECT and ERT measurements were made for 4 min. Maximum difference in frequency calculations between ECT and ERT is about 0.01 Hz at superficial air velocity of 1.1 m/s.

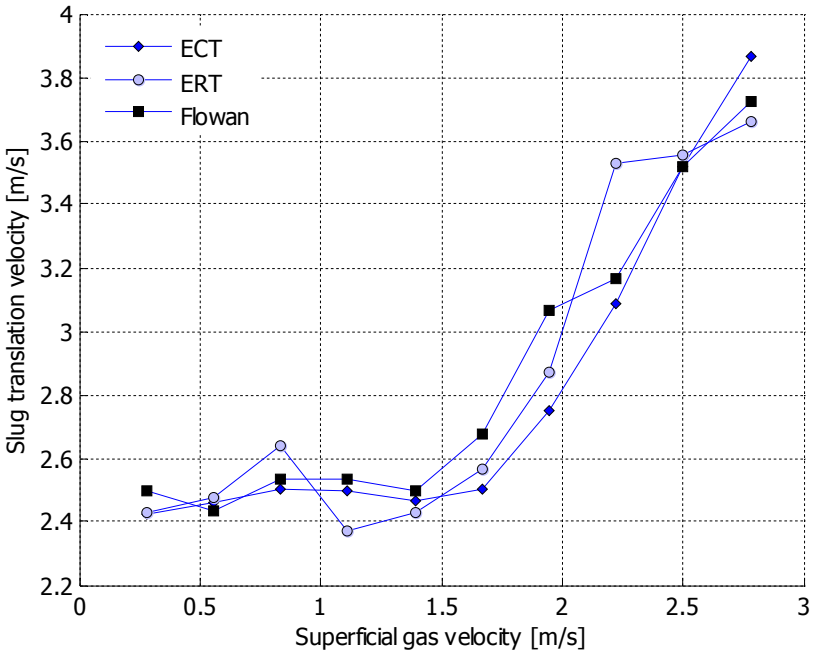

Figure 5. Slug velocity with water superficial velocity at 0.2 m/s

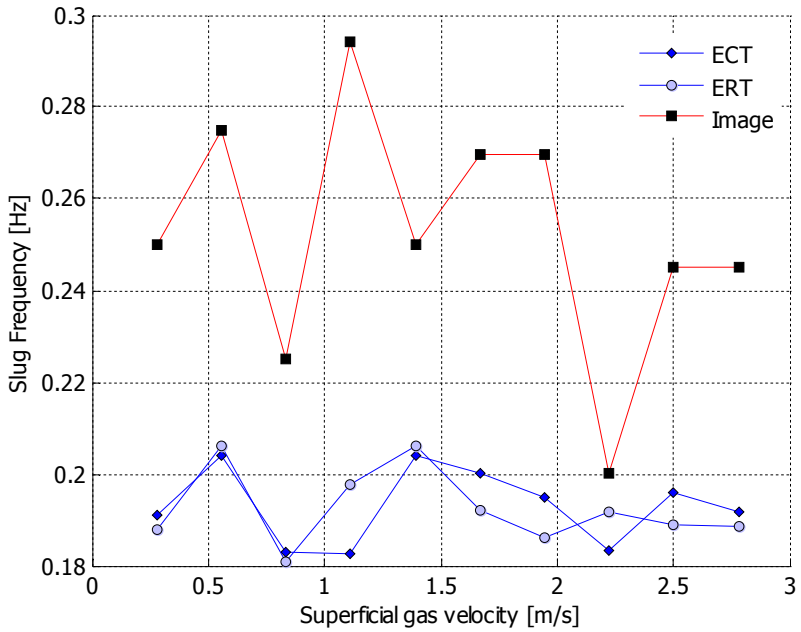

Figure 6. Slug Frequency with water superficial velocity at 0.2 m/s

Slug length calculations were made using equation (4) and calculated velocities given in Figure 5. Lower gas velocities should result in a shorter slug but higher gas velocities should show increases in slug length as explained by Cai et al (1999). All 3 curves in Figure 7, show decrease in slug lengths with increase in superficial water velocities. At superficial gas velocity 2.2 m/s, image data based calculation gives 1.7m for the mean slug length. Difficulties involved in estimating exact time window of the slug is one of the reasons for the variations in image based approach. The slug velocity V_s used in the calculation was from the ERT system and it might also be the reason for getting some higher and lower slug length values. To see whether the trend observed exists with different flow conditions, another two sets of experiments were performed varying superficial water velocities to 0.27m/s and 0.33 m/s. Results after the ECT measurement based calculations are given in Figure 9. It can be seen clearly in Figure 9 that the mean slug length decreases with increase in superficial gas velocity.

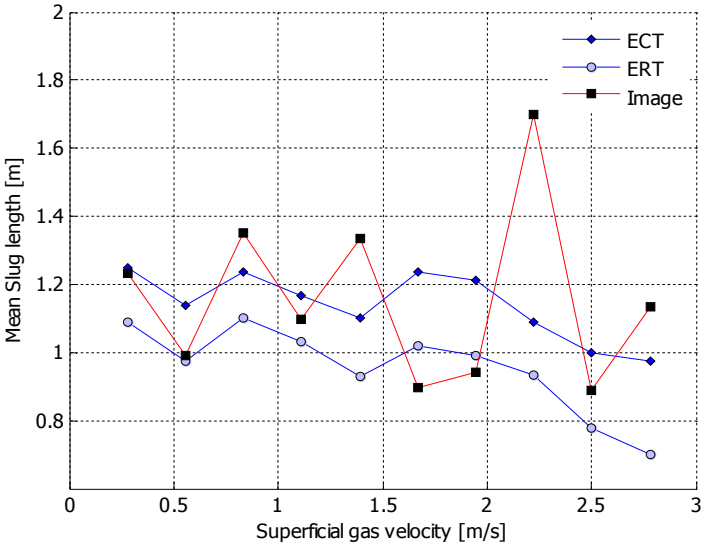

Figure 7. Slug Length with water superficial velocity at 0.2 m/s

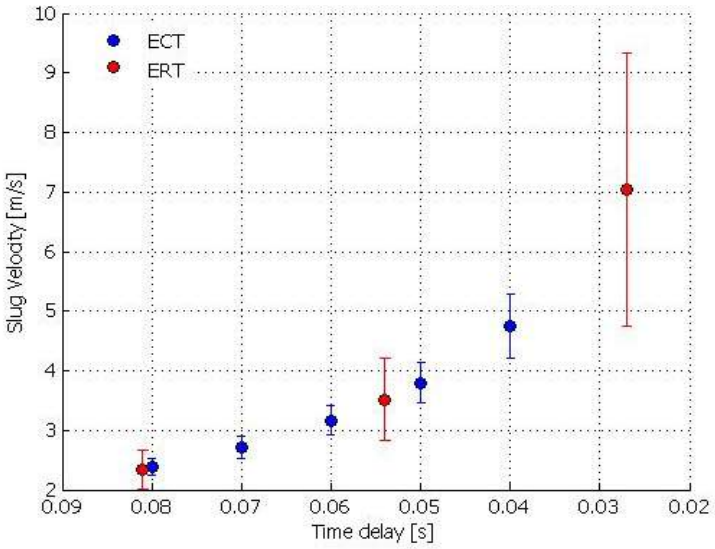

Figure 8. Estimated uncertainties for different slug velocities

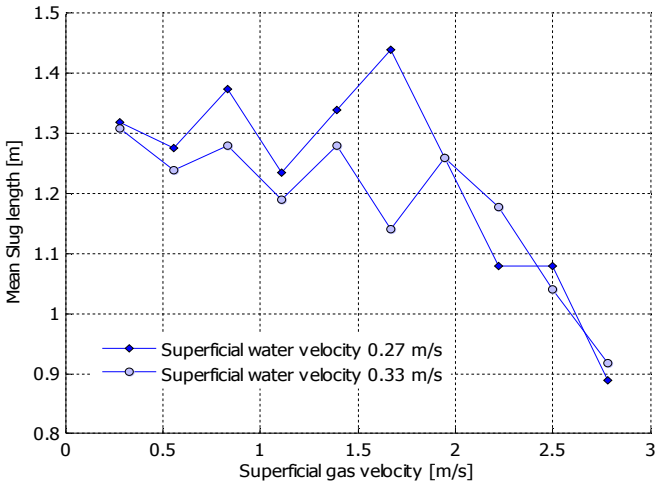

Figure 9. Slug Length for varying superficial gas velocities at superficial water velocity 0.27 m/s and 0.33 m/s

4.1 Variations in Velocities in cross-sectional area

Correlations between corresponding inter-electrode measurements of ERT signals were performed to see the possibilities of observing the velocity variations in the pipe cross-section. Figure 10 shows some selected combinations of electrodes to see the effects of flow regime on capacitance values. As given in Figure 11 correlations based on the electrode combinations $E_1E_2-E_3E_4$, $E_1E_2-E_{10}E_{11}$, $E_1E_2-E_1E_{16}$, $E_2E_3-E_5E_6$, $E_2E_3-E_1E_{16}$, $E_4E_5-E_{14}E_{15}$ and $E_5E_6-E_{14}E_{15}$ give the slug velocity as 7 m/s. Since some of the combinations of electrodes given above, cover a larger sensing area of the pipe section, these particular combinations may lead to better estimates of the velocity and its variations. Not all combinations are sensitive to velocity variations, although they all give the average velocity as 3.5m/s.

The combinations $E_2E_3-E_6E_7$, $E_3E_4-E_7E_8$ and $E_4E_5-E_7E_8$ covering the pipe bottom give an estimate of 2.3 m/s velocity.

Figure 11 shows only 3 different velocities from all different combinations. These 3 velocities are the same velocities discussed Figure 8.

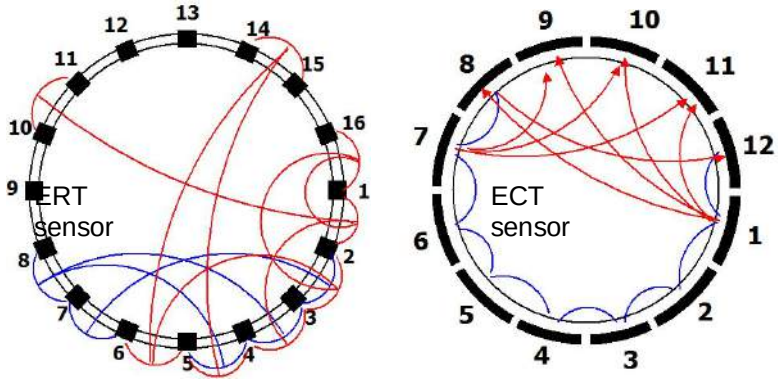

Figure 10. Electrode arrangements of ERT and ECT sensors

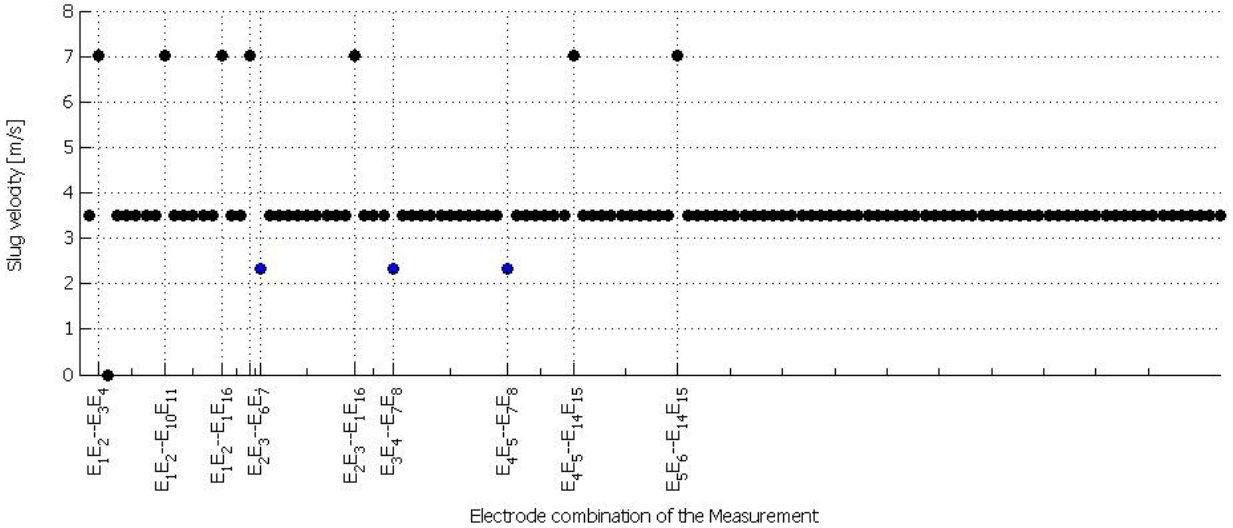

Figure 11. Slug velocities with cross-correlation of individual ERT measurements at superficial gas and water velocities 2.78 m/s and 0.2 m/s

Figure 12 shows the slug velocities obtained with ECT measurements. Correlation measurement of signals of the capacitance values $C_{1,8}$, $C_{1,9}$, $C_{1,10}$, $C_{1,11}$, $C_{7,9}$, $C_{7,10}$, $C_{7,11}$ and $C_{8,12}$ *at both planes,* give the estimated velocity as 4.7m/s. These combinations are from the top half of the sensor and cover a larger area of the medium air, i.e. the top part as shown in Figure 4. Signals of adjacent electrode combinations $C_{1,2}$, $C_{1,12}$, $C_{2,3}$, $C_{3,4}$, $C_{4,5}$, $C_{5,6}$, $C_{6,7}$ and $C_{7,8}$ show lower slug velocities (most of them are around 3.1 m/s). Most of these combinations are from the bottom half of the pipe. The ECT results give better estimates of the slug velocities compared to those estimated using the ERT data.

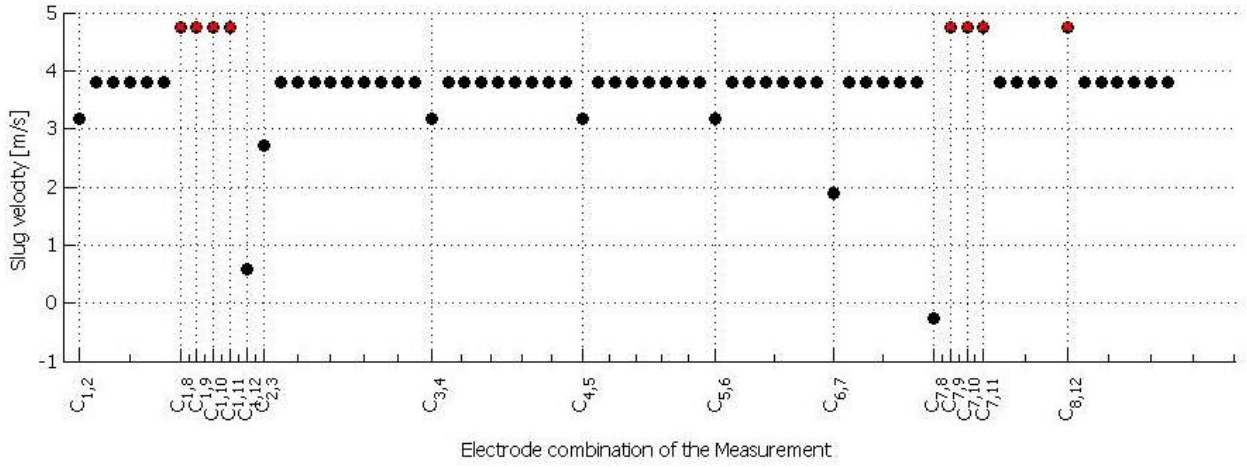

Figure 12. Slug velocities with cross-correlation of ECT measurements at superficial gas and water velocities 2.78 m/s and 0.2 m/s. The capacitance values indicated on the axis refer to the respective electrode combinations on plane 1 and plane 2.

5 CONCLUSION

The study presented here compares the estimates of the following parameters for a two phase air/water flow: slug frequency, slug length, slug velocity and some information on velocity distribution across the pipe section. For the estimation a data fusion methodology based on cross-correlation of inter-electrode resistance/capacitance values from ERT and ECT systems is used. From the estimates thus obtained, uncertainty of the slug velocity is also calculated. Some parameters are verified using high speed camera. These results show that the trend is the same for the slug parameters calculated as functions of superficial air velocities. Increasing frame rates of both ECT/ERT systems and simultaneous capturing of the raw resistance and capacitance values may improve the quality of all the estimates.

6 NOMENCLATURE

N_R	Number of electrodes in ERT sensor	t_s	Time window of the slug (s)
N_C	Number of electrodes in ECT sensor	T	Observation time period (s)
M	Number of measurements per frame	τ_{max}	Time delay at correlation peak
S	Signal	L	Distance between two sensors (m)
pl_i	Plane i	$\rho_{S_{pl_1}S_{pl_2}}$	Cross-correlation function of signals from 1st and 2nd planes
τ	Time delay (s)	$C_{i,j}$	Capacitance between i th and j th electrode
V_s	Slug velocity (m/s)	$E_iE_j - E_kE_l$	Voltage measurement between k and l Electrodes when i and j electrodes are used for injecting the current (ERT)
n_s	Number of slugs		
f_s	Slug frequency (Hz)	ERT	Electrical Resistance Tomography
L_s	Slug length (m)	ECT	Electrical Capacitance tomography

7 ACKNOWLEDGEMENT

The work is based on an on-going project supported by the Research Council of Norway. The advice and help provided by Mr. Talleiv Skredtvedt of the Mechanical Engineering Laboratory of Telemark University College, in conjugation with sensor assembly, rig related activities are very much appreciated. Dr. W. A. S.

Kumara has assisted us with the operation of multiphase rig. We appreciate very much the advice given by Mr. Malcolm Byars of Process Tomography Ltd. Chaminda Pradeep and Yan Ru are PhD students funded by the Norwegian Ministry of Education.

8 REFERENCES

ISMAIL I., GAMIO J. C., BUKHARI S. F. A., YANG W. Q. (2005) Tomography for multi-phase flow measurement in the oil industry, *Flow Measurement and Instrumentation*., 16(2011), 145-155.

AHMED W.H., (2011), Experimental investigation of Air-oil slug flow using capacitance probes, hot-film anemometer and image processing, *International Journal of Multiphase Flow*., 37(2011), 876-887

KANG C., JEPSON W.P., GOPAL M., (1999) 'Effect of Drag-Reducting Agent on slug characteristics in Multiphase flow in inclined pipes', Journal of Energy Resources Technology. Vol. 121.

Al-LABABIDI S., (2006), *Multiphase Flow Measurement in the Slug Regime Using Ultrasonic Measurements Techniques and Slug Closure Model*, Thesis submitted to the Cranfield University for the degree of philosophiae doctor, UK.

RANDALL E. W., WILKINSON A. J., LONG T. M., SUTHERLAND A. (2004), A high speed current pulse electrical resistance tomography system for dynamic process monitoring., Proceedings of 7th Biennial ASME Engineering Systems Design and Analysis., Manchester, UK.

DAILY, W., RAMIREZ A., NEWMARK R., GEORGE V., RANDALL J., (2000) 'Imaging UXO Using Electrical Impedance Tomography', in Proceedings for SAGEEP, Washington D.C., pp793, 2000

DATTA U., (2007) *Multimodal Measurements in Dilute Phase Pneumatic Conveying Systems*, Telemark University College, Thesis submitted to the NTNU for the Degree of philosophiae doctor, Norway.

CAI J.Y., WANG H.W., HONG T., JEPSON W.P., (1999) Slug frequency and length inclined large diameter multiphase pipeline. Multiphase flow and heat transfer proceeding of Fourth International Symposium. China.

Paper 5

Co-operative sensor fusion using time warping in multimodal tomometry for process control

This paper was presented as an oral presentation at the IEEE conference on Systems and Industrial Informatics (ICCSII)in Bandung, Indonesia in September 2012.The paper was also published in the IEEE conference proceedings of Systems and Industrial Informatics 2012 (ISBN: 978-1-4673-1022-2, September 2012, pp: 219-224)

Co-operative sensor fusion using time warping in multimodal tomometry for process control

Chaminda Pradeep , Yan Ru and Saba Mylvaganam,
Faculty of technology
Department of Electrical Engineering, Information Technology and Cybernetics
Telemark University College
Porsgrunn, Norway
Email: saba.mylvaganam@hit.no

***Abstract*- Recent studies in process tomography have mostly focused on image processing and enhancement of images obtained from Electrical Capacitance, Electrical Resistance, Electrical Impedance, Gamma- and X-ray- tomographic modalities. In the process industries, there is a growing need for fast acting measurement and control procedures, architectures and their implementation within existing sensor and control suites. With this industrial relevance, a multimodal tomometric sensor fusion is studied involving pressure and capacitance measurements in a two phase flow rig. Pressure is measured using standard pressure sensors, whereas the capacitance are measured using arrays of capacitance electrodes placed on the periphery of a section of the pipe in the multiphase flow rig. These capacitance measurements are performed by using ECT-modules. In this paper, the focus is on early slug detection and timely characterization of these slugs formed in the two phase flow. To associate simultaneous occurrence of slug based phenomena in the time series of the pressure and ECT-signals, dynamic time warping (DTW) algorithms are used. The usage of DTW and the multimodal tomometric sensor suite with pressure and ECT-modules leads to a co-operative sensor data fusion, which can help to identify characteristic features of slugs in two phase flows, which can be significant inputs to the process control unit in the assessment/implementation of necessary actions, such as activating choke valves, reducing pump outputs of one or more of the phases flowing in the rig. Time series of pressure and ECT-signal are studied using DTW and results are compared and fused with some discussions on how these could be used in process control.**

Keywords*- *Multimodal tomometry, ECT (Electrical capacitance Tomography), sensor fusion, soft sensor, two phase flow, Dynamic Time Warping (DTW)

NOMENCLATURE

ECT	Electrical Capacitance Tomography
DTW	Dynamic Time Warping
TB	Taylor Bubble

LIST OF SYMBOLS

N	Number of capacitance Electrodes
α_w	Water volume ratio
C_{ij}	Capacitance measurement between electrodes *i* and *j*.
P_w	Warping path
X ,Y	Time series signals
δ	Squared distance between two time series elements
Co_δ	Cost matrix
Dp	Differential pressure (mbar)
t_s	Time window of the slug (s)
V_s	Slug Velocity (m/s)
d	Distance between two ECT sensor planes
τ	Time lag (s)
L_s	Liquid slug length (m)
h_{Dp}	Pressure peak (normalized)
$\bar{h}_{Dp}$	Mean of the Pressure peak
$\sigma_{h_{Dp}}$	Standard deviation of the Pressure peak

I. INTRODUCTION

Electrical capacitance tomography (ECT) is gaining increased acceptance in multiphase flow measurements. Most of the research facilities of leading industries have included ECT in their measurement systems. Pressure signals coming from well-established sensors in the study of flow in pipes, have vast amount of information on multiphase flows. The information from pressure signals has been used to characterize some flow parameters. In this paper, ECT measurements and differential pressure (Dp) measurements are fused and the results from the fusion are used to identify and characterize the liquid slug.

Dynamic time warping (DTW) technique has been used mainly in speech recognition applications [1]. DTW techniques are used here to fuse the Dp and ECT signals.

II. TEST FACILITY WITH THE MEASUREMENT SYSTEM

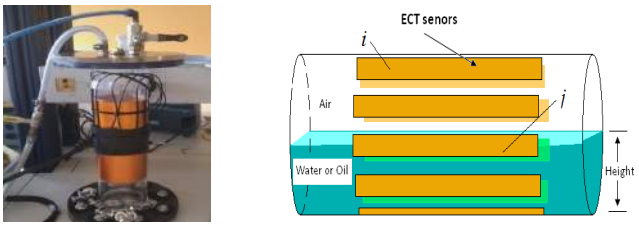

(a) (b)

Figure 1. (a) The actual sensor head used in experiments (b) Schematic diagram. Cij is the capacitance measured between the elctrodes i and j covering all the combinations excluding i=j. i, j= 1, 2, …,12.

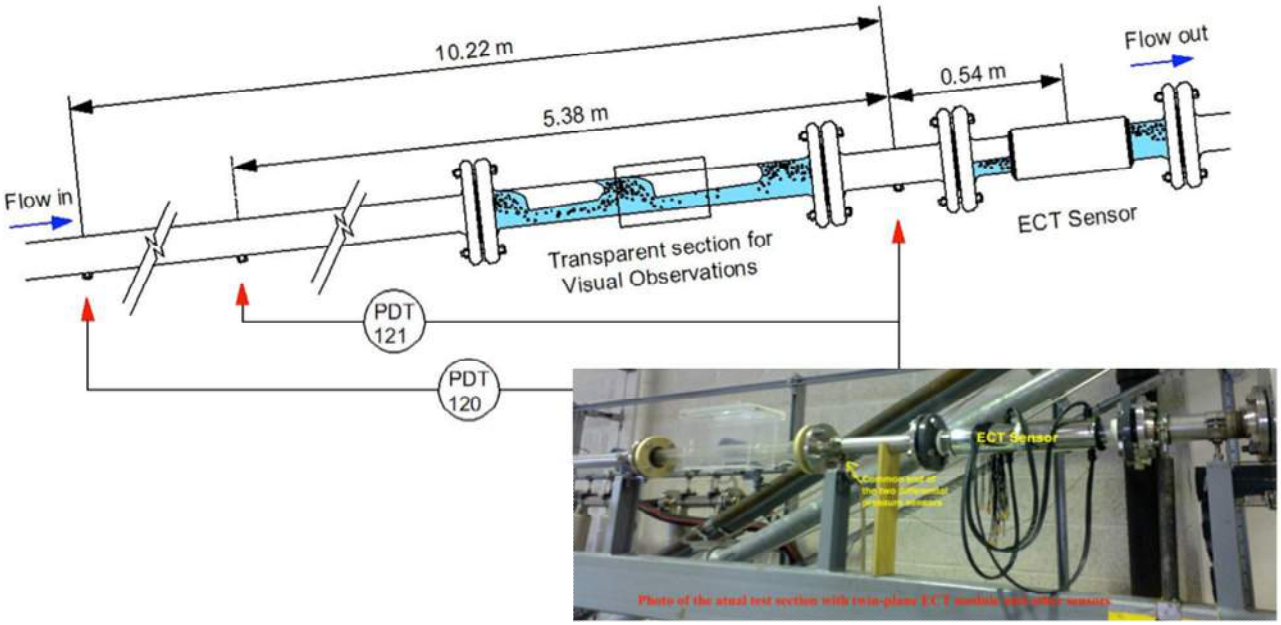

Figure 2. Test section in the multiphase flow rig containing pressure and ECT-modules with details of relevant dimensions. Inset: Photo of the actual test section with twin-plane ECTm module and other sensors

A. Electrical Capacitance Tomography

Electrical capacitance tomography (ECT) is a non-invasive method of imaging the cross sectional permittivity distribution of a mixture of materials with different permittivities inside vessels, based on inter-electrode capacitance measurements, [2]. In generating images needed for estimating the distribution of materials, the capacitances between all possible combinations of the electrode pairs are measured, using an array of electrodes placed externally around the periphery of the vessel, [3]. A schematic showing the assembly of all the electrodes on the sensor head is shown in Fig. 1 (b).

As shown in Fig. 1, the electrodes are arranged very often symmetrically taking necessary precautionary measures to improve the signal to noise ratio. These measures are mainly based on avoiding spurious capacitance values, e.g. inclusion of guard electrodes, shielding etc. In the context of this paper, the arrangement shown in Fig. 1 is called the ECT sensor module. In our application, the ECT sensor consists of one circumferential set of N capacitance electrodes placed around the pipe separator (in the experiments described below, N=12). During the experiments performed in conjunction with this study, the pipe is kept horizontal, as shown in Fig. 1 (b).

B. Multi-phase flow loop

Simple flow Diagram of the testing section of experimental flow-rig used in this study is shown in Fig. 2. Experiments were performed using water and air at room temperatures and atmospheric outlet pressure. Differential pressures between the points marked in red arrows were captured from sensors PDT120 and PDT121.water is circulated using volumetric pumps. The mass flow, density and temperature were measured for each phase, before the components enter the test section using Coriolis flowmeters. The test section is a 15m long steel pipe with inner diameter 56mm. with the test section of the pipe having adjustable inclination in the range of -10º to +10º to the horizontal. Liquid and air flow 12.5 m from the inlet of the test section to pass the first tomography sensor plane. Distances between points where the differential pressure is measured are also given in the same figure. Coriolis flowmeters provide high accuracy with uncertainty ± 0.01kg/min. PID controllers implemented in LabVIEW controls the liquid flow rates. In this experimental study, the inlet air and water flow rates were maintained at 0.25kg/min and 50kg/min while the pipe inclination was fixed at +1º to the horizontal.

Volume ratio, α_w can be calculated using (1) based on inter-electrode capacitance measurements as explained in [3] and [5].

$$\alpha_w = \frac{1}{N(N-1)} \sum_{i=1}^{N} \left(\sum_{j=1}^{N} C_{ij} \right) \qquad \forall\, i < j \qquad (1)$$

Where N=12 and C_{ij} is the capacitance between electrodes i and j.

III. DYNAMIC TIME WARPING (DTW)

Dynamic Time Warping is implemented in many algorithms in the field of speech and image processing for establishing similarities in two or more sequences of observations (Usually measurements) in the form of time series. DTW is a versatile tool in data mining applications, where there is a need for detecting “matches” in many sets of

time series. The sets of time series are warped in the temporal domain somewhat non-linearly under some constraints. As such, DTW is a useful tool in sensor data fusion in process industries, where the tags can run into thousands and data can run into TB regions.

The use of DTW is to compare two time series signals. Here the warping path and two time series signals are defined as $P_w = (p_1, p_2, \ldots p_L)$, $X = (x_1, x_2, \ldots x_r)$ and $Y = (y_1, y_2, \ldots y_s)$ respectively. *r* and *s* are number of elements in the X and Y time series and L is length of the warping path. Warping path aligns the points in time series *X* and *Y* in such a way that the distance between them are minimized. Squared distance between two elements can be defined as:

$$\delta(x_i, y_j) = (x_i - y_j)^2 \tag{2}$$

Then total cost Co_δ of a warping path P_w between *X* and *Y* signals with respect to δ can be defined as:

$$Co_\delta(X,Y) = \sum_{k=1}^{L} \delta(x_i - y_j)_k \tag{3}$$

Here, *i* and *j* corresponds to the location in the $Co_\delta(X,Y)$ matrix and *k* is the corresponding point of the warping path P_w. Then the best alignment between *X* and *Y*, is found following the path through the minimum points of the $Co_\delta(X,Y)$ matrix [4].

$$DTW(X,Y) = \min_{P} \sum_{k=1}^{L} \delta(p_k) \tag{4}$$

The DTW given in (4) is found using dynamic programming [5].

IV. CHARACTERIZATION OF FLOW REGIME AND SLUGS

Under the experimental conditions given above slug flows can be observed. Water volume ratio signal (α_w) calculated from ECT measurements using (1) can then be used to estimate liquid slug parameters. As shown in Fig 3, a threshold value is selected to locate t_s. In this analysis, a threshold of 0.7 was selected. When the volume fraction α_w reaches the threshold value of 0.7 from lower values of α_w, the corresponding time stamp is picked. When the volume fraction α_w reaches the threshold value of 0.7 again in the descending mode, on its way back to the stratified region, the second time stamp is picked. Then the difference between these two time stamps is calculated giving the value of t_s. Then this time difference t_s is used in the slug length L_s calculation as given in (5). Here V_s is the velocity of the slug.

$$L_s = V_s t_s \tag{5}$$

Similarly, L_s of each slug observed using the time series of pressure *Dp* and volume fraction α_w is calculated. Since a twin plane ECT sensor is used in these measurements, two time series of α_w can be calculated. Cross-correlation of those two α_w signals gives the time lag, τ , between two signals corresponding to the correlation peak. Since the distance between two sensor planes is known (d =190mm). The slug velocity V_s can easily be calculated using (6) as explained in [7].

$$V_s = \frac{d}{\tau} \tag{6}$$

Differential pressure signal (Dp) from DP121 sensor was also recorded along with the capacitance measurements from ECT-module. Then the sets of time series consisting of differential pressure Dp and water volume fraction α_w signals are warped to get the optimum alignment. The warping of Dp signal on to the α_w is selected here for the estimation of the magnitude of Dp (h_{Dp}) at the liquid slug region as shown in Fig 4. As illustrates in Fig 4 the warped Dp signal indicates its peak within the corresponding liquid slug body. Hence, maximum Dp value (h_{Dp}) can easily be selected. Similarly h_{Dp} values correspond to all slugs can be selected.

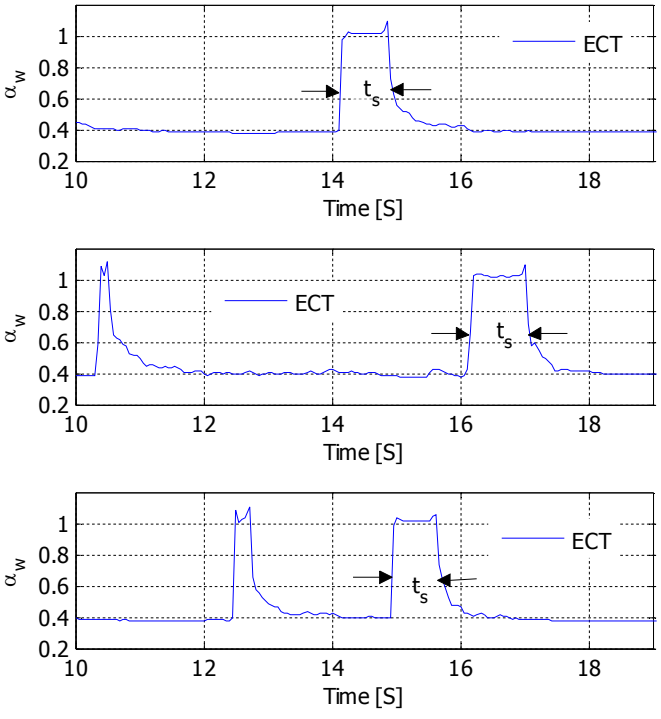

Figure 3. Typical slug pulse as obtained from ECT-module based water volume fraction, shown here as part of a time series with characteristic features depicting slug formation

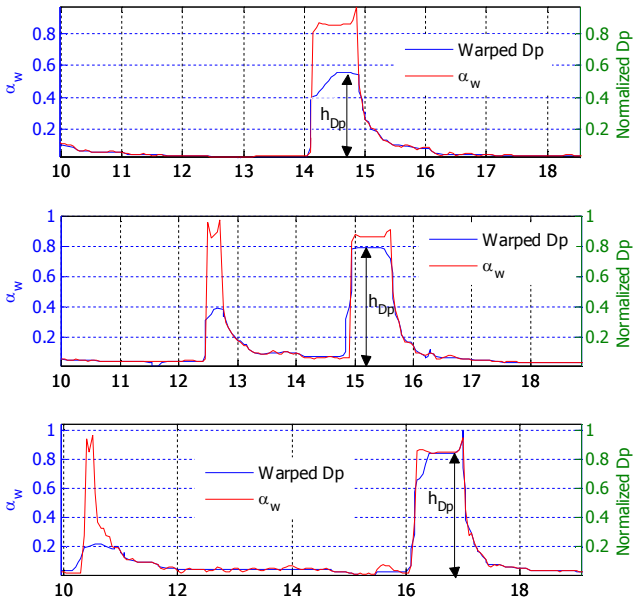

Figure 4. Warping Dp on to α_w signal and selection of h_{Dp}

V. EXPERIMENTAL RESULTS

Signals used in the analysis are given in the Fig 5. Warping path p_w is indicated in white of Co_δ matrix plot shown in Fig 6. Then the warped Dp signal with reference to water volume ratio signal is extracted from the warping path information. Fig 7 illustrates the mapping of differential pressure signal Dp onto the volume fraction signal α_w

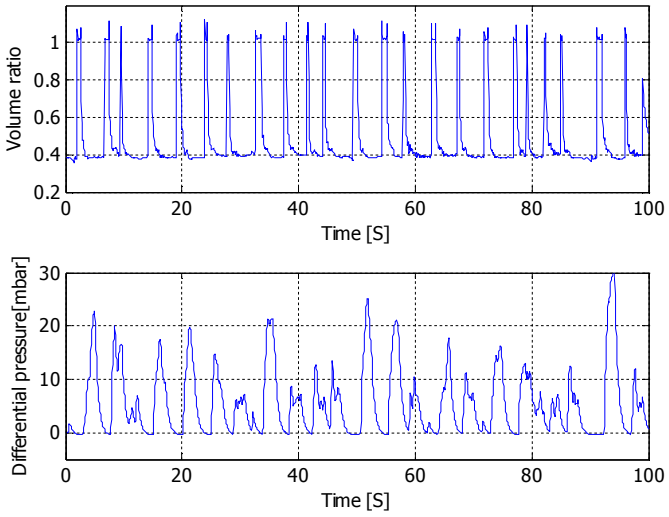

Figure 5. Typical sets of time series (water volume fraction α_w and differential pressure Dp signals) used in the data mining algortihms

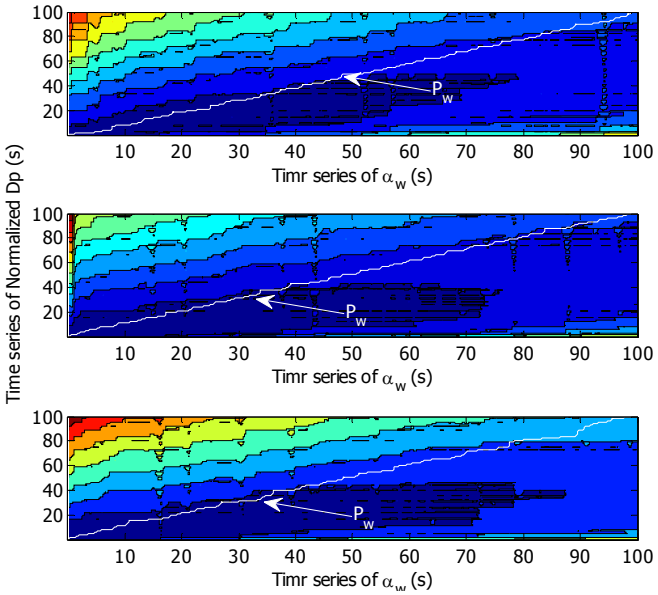

Figure 6. The cost matrix and warping path (white line) using the time series of differential pressure Dp and water volume fraction α_w

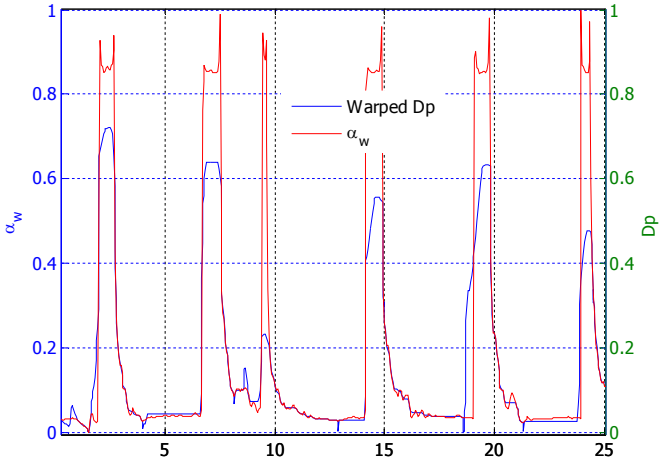

Figure 7. The warped versions of Dp and α_w signals represented using a common time axis.

It can be seen from Fig 7 that positive-going and negative going flanks of water volume fraction α_w and warped Dp are aligned properly with the plateau parts of these two time series also falling in the same time slots. It is interesting to note that for plateaus for water volume fraction α_w with wider time slots, higher amplitudes of differential pressure signals Dp can be observed.

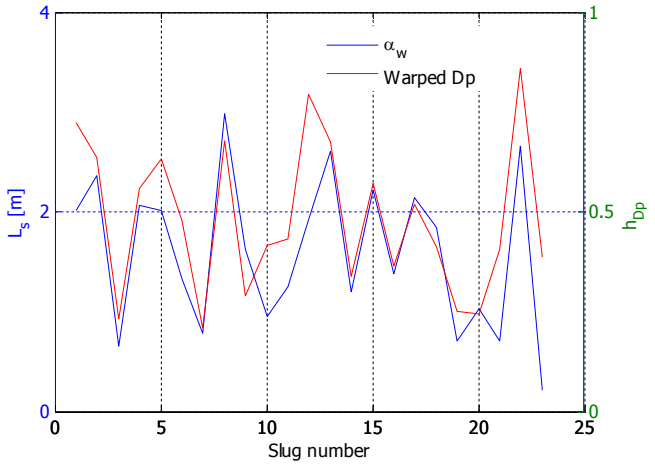

Figure 8. Slug lengths as calcualted using slug velocities for slugs found using Figure 7

The lengths of different slugs (L_s) calculated using (4) with the help of the slug velocities are given in Fig. 8. The liquid slug length (L_s) and magnitude of the *D*p peak which lies within the corresponding slug body (h_{Dp}) is then studied both with respect to the time slots and their respective amplitudes. The results for 23 slugs observed are presented in Fig 8. From Fig. 8, it can be seen that for longer liquid slugs higher h_{Dp} values are generated, whereas for shorter slugs the values of h_{Dp} are lower.

The variations of slug lengths for different inflow conditions of air and water as estimated using the DTW based algorithm is given in Table 1.

TABLE I. PRESSURE PEAK VARIATION UNDER DIFFERENT SLUG LENGTHS

Slug Length (m)	Pressure peak ($\bar{h}_{Dp} \pm \sigma_{h_{Dp}}$)	
	Inlet Flow rates Air -- 0.25kg/min Water-- 50kg/min	Inlet Flow rates Air -- 0.10kg/min Water -- 50kg/min
0-0.5	0.38	--
0.5-1	0.30 ± 0.09	0.31 ± 0.11
1-1.5	0.37 ±0.09	0.406
1.5-2	0.49 ± 0.2	0.55 ± 0.14
2-2.5	0.61± 0.07	0.62 ± 0.15
2.5-3	0.73± 0.10	0.78 ± 0.21

The pressure peaks observed using the DTW algorithm follow the trend shown in Fig 9. The lengths of slugs and corresponding pressure peaks were then classified into 6 different groups as given in Table l. The mean of h_{Dp} and their deviations are given in the other columns for the experimental conditions given.

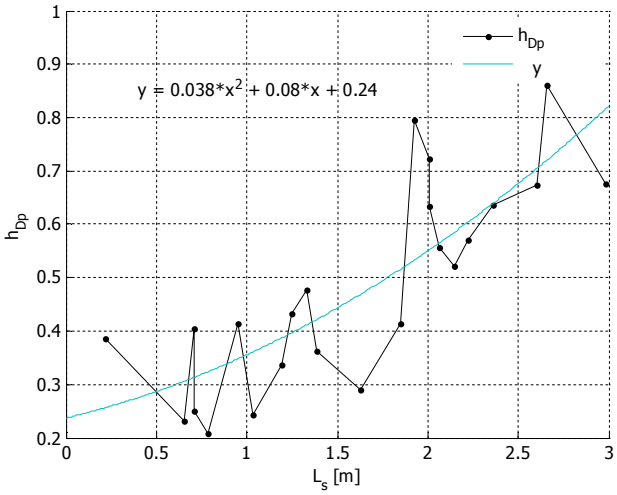

Figure 9. Variation of Normalized pressure peak (h_{Dp}) with increasing Slug lengths

VI. SOFT SENSOR APPROACH USING PROCESS TOMOMETRY

The results from the multimodal tomometric approach involving capacitance values from ECT-module and differential pressure sensors indicate that useful information on flow regime and slug can be extracted from a fusion of these two sets of time series. This is an example of a soft sensor approach giving the process engineer parameters such as V_s, L_s and the time slots of the occurrences of slugs. The system integration of the differential pressure Dp and ECT-sensor with the soft sensor outputs related to the flow regime/slug are shown in Fig 10 with a schematic of the control architecture for mitigating the detrimental effects of heavy slug formation and its transportation to sensitive hardware like valves and pumps is a multiphase loop.

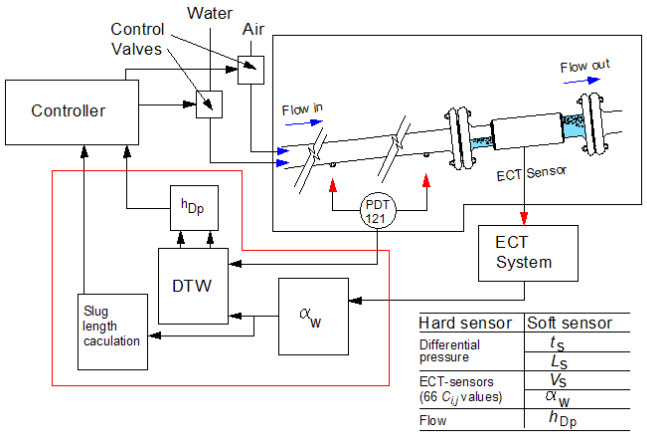

Figure 10. Block diagram for the system with soft sensor outputs in a control scenario to ascertain slug length and mitigate slug induced flow problems.

VII. CONCLUSIONS

The simultaneous observations of differential pressure and capacitance values form an ECT-module in a pipe section in

multiphase flow gives the process engineer a set of time series, which can then be subjected to data mining using various procedures. In the present study, differential pressure signals and water volume fraction signals as estimated with capacitance values from ECT-sensor modules form a good set of cooperative sensor data for data fusion. The data mining and data fusion are done using dynamic time warping (DTW). With the dynamic time warping, some physical phenomena are clearly captured and their characterizations are facilitated, especially with respect to slug and pressure peaks. The aligned signals of pressure and volume fractions clearly indicate the possibility of identifying the time of occurrence and the extent of slugs. With a set of two time series, based on two physical measurands, viz. pressure and capacitance, the soft sensor approach described in this paper gives rise to water volume fraction, flow regime identification, slug velocity, frequency and length and the time of occurrence and duration of these flow regimes. The interdisciplinary group in the Telemark University College looking into CFD codes for multiphase flow is looking into the ways and means of unambiguously identifying input parameters giving rise to certain type of slugs. These could be compared with the results given in this paper, especially those given in Table 1 and Fig 10.

This is a valuable tool for the process engineer in making decisions as to what kind of control actions are to be taken.

ACKNOWLEDGMENT

Part of the work was done in conjunction with the strategic Institute Programme (SIP) supported by the Research Council of Norway, MULTIPROCONd. Our colleagues in the mechanical and electronic workshops Talleiv Skredtveit and Eivind Fjelldalen helped us with all the mechanical engineering work associated with the project. Support of Mr. Malcolm Byars of PTL Ltd. is very much appreciated. Yan Ru and Chaminda Pradeep are PhD candidates at Telemark University College funded by the Royal Norwegian Ministry of Education and Cultural affairs.

REFERENCES

[1] H. Sakoe, and S. Chiba., Dynamic programming algorithm optimization for spoken word recognition, IEEE Transactions on Acoustics, Speech and Signal Processing, 26(1) pp. 43– 49, 1978, ISSN: 0096-3518

[2] M. Byars, “Developments in Electrical Capacitance Tomography”, Process Tomography Limited, Cheshire, United Kingdom

[3] Process tomography Ltd., “Electrical capacitance tomography system operation manual,” issue 6, vol.1, September 2008

[4] M. MÜller, “Information Retrieval for Music and Motion”, 2007, http://www.springer.com/978-3-540-74047-6,

[5] E. J. Keogh and M.J. Pazzani, Scaling up Dynamic Time Warping for Datamining Applications, ACM, 2000

[6] C. Pradeep, Y. Ru, S. Mylvaganam, “Reverse flow alarm activation using electrical capacitance tomometric (ECTm) correlation”, proceedings of IEEE internl. Sensors Application Symposium (SAS 2012), Brescia.

[7] C. Pradeep, Y. Ru, S. Mylvaganam, “Multimodal tomometry for slug detection in two phase flow”, proceedings of 6th International symposium on process tomography(ISIPT 2012), Caper Town.

ISBN 978-82-7206-400-5
ISSN 1893-3068

www.hit.no
2015